Towards multiscale modelling of CO_2 corrosion

Carles Rafols i Belles

A thesis presented for the degree of

Doctor of Philosophy

June 2022

Chemistry Department

Imperial College London

Abstract

CO_2 corrosion is a serious environmental and financial concern for the oil and gas industry requiring the continuous development of cost-effective corrosion prevention and mitigation strategies. Over the last decades, the $FeCO_3$ scale that forms during the CO_2 corrosion process has gained much interest as it can prevent further corrosion once fully formed. However, fundamental research on CO_2 corrosion and the formation of these corrosion scales is still lacking due to the complexity of these electrochemical systems. Density Functional Theory calculations can be instrumental in supporting and interpreting experimental results. In this work, the results of DFT PDOS calculations of oxygen adsorbed on an Fe(110) surface revealed a hybridised orbital around the Fermi level that explains the origin of the asymmetric oxygen peak in the XPS spectrum. Other more traditional electrochemical models have been developed over the years to improve our understanding and forecasting capabilities of CO_2 corrosion, however these models are unable to capture the stochastic nature of the corrosion process which is key to describe stochastic phenomena such as localised corrosion and the formation of the corrosion scale. This work presents the Semi-local Corrosion Approximation, a novel modelling technique that combines a general corrosion electrochemical model with elements of cellular automaton stochastic models to simulate the corrosion process using a 3-dimensional description of the corrosion system. The model predicts the evolution of the physical properties of the corrosion scale which are found to play an important role in the protection of the steel surface. The 3-dimensional analysis of the corrosion scale shows that scales formed under a high precipitation rate may develop localised corrosion as the $FeCO_3$ supersaturation is consumed before the scale fully covers the steel surface.

Statement of Originality

I declare that this thesis and the work presented in it are my own and has been generated by me as the result of my own original research, except where explicitly referenced.

Carles Rafols i Belles

London, June 2022

Copyright Declaration

The copyright of this thesis rests with the author. Unless otherwise indicated, its contents are licensed under a Creative Commons Attribution-ShareAlike 4.0 International (CC BY-SA).

Under this licence, you may copy and redistribute the material in any medium or format for both commercial and non-commercial purposes. You may also create and distribute modified versions of the work. This on the condition that: you credit the author and share any derivative works under the same licence.

When reusing or sharing this work, ensure you make the licence terms clear to others by naming the licence and linking to the licence text. Where a work has been adapted, you should indicate that the work has been changed and describe those changes.

Please seek permission from the copyright holder for uses of this work that are not included in this licence or permitted under UK Copyright Law.

Acknowledgments

I would like to thank my supervisor Prof. Nicholas Harrison for giving me the opportunity to pursue this PhD and for his continuous support and encouragement. Would like to thank BP for sponsoring the project and for providing guidance and industry expertise when needed. I am thankful and grateful to the TSM CDT for sponsoring me and for all their support throughout my PhD. I would also like to thank all the researchers that contributed to the ICAM56 project for their support, the insightful discussions and collaborations.

I dedicate this thesis to my family. Their unconditional support, love and patience helped me immensely in this long journey.

Publications

Acres, M.J., Hussain, H., Walczak, M.S., Nikiel, M., Sewell, C., Rafols i Belles, C., Ahmad, E.A., Walton, A.S., Muryn, C.A., Harrison, N.M. and Lindsay, R., 2020. Core level photoemission line shape selection: Atomic adsorbates on iron. Surface and Interface Analysis, 52(8), pp.507-512.

Contents

1 Introduction **17**

1.1 CO2 corrosion 19

1.2 Corrosion product layer 20

1.3 CO2 corrosion models: a review 22

2 Semi-local Corrosion Approximation **27**

2.1 Introduction 27

2.2 Semi-local Corrosion Approximation 29

2.2.1 Water chemistry 30

2.2.2 Electrochemical model 32

2.2.3 Corrosion product precipitation 38

2.2.4 Mass transport 43

2.2.5 Stochastic 3-dimensional model 52

2.3 Algorithm 56

2.3.1 Initialisation 56

2.3.2 Solution chemistry 57

2.3.3 Corrosion and precipitation rates calculation 57
2.3.4 Iteration cycle 58
2.4 Model variance 59
2.5 Conclusions 64

3 CO_2 corrosion time-series analysis **67**

3.1 Introduction 67
3.2 Validation of the model 68
3.3 Predictions of scale growth 71
3.3.1 pH dependence 72
3.3.2 A/V dependence 77
3.3.3 Temperature dependence 79
3.3.4 Pressure dependence 81
3.4 Conclusions 84

4 CO_2 corrosion multiparameter analysis **87**

4.1 Introduction 87
4.2 Multiparameter analysis 88
4.3 Conclusions 96

5 Additional use cases **98**

5.1 Introduction . . . 98

5.2 Changes in the environment . . . 99

5.3 Corrosion inhibitor protection . . . 106

5.4 Conclusions . . . 111

6 Atomistic scale corrosion modelling **113**

6.1 Introduction . . . 113

6.2 Density Functional Theory . . . 114

6.2.1 Schrödinger equation . . . 114

6.2.2 Born-Oppenheimer approximation . . . 115

6.2.3 Molecular orbitals . . . 117

6.2.4 Variational principle . . . 118

6.2.5 Hartree-Fock approximation . . . 119

6.2.6 Hohenburg-Kohn Theorems . . . 120

6.2.7 Kohn-Sham equations . . . 122

6.2.8 Exchange-correlation functional . . . 123

6.3 Computational methods . . . 125

6.4 Iron bulk and surface properties: a comparative study . . . 126

6.5 Oxygen adsorption on Fe(110) . . . 134

6.6 O/Fe(110) XPS analysis . . . 140

6.7 H_2CO_3/Fe(110) adsorption geometry . . . 144

6.8 Conclusions . . . 145

7 Conclusions **147**

A Atomistic scale corrosion modelling **152**

A.1 basis sets . . . 152

A.1.1 Iron 8-64111d41G . . . 152

A.1.2 Oxygen 8-411d11G . . . 154

A.1.3 Carbon 6-311d11G . . . 155

A.1.4 Hydrogen TZVP . . . 156

A.2 Vibrational frequencies . . . 156

B Semi-local Corrosion Approximation **158**

B.1 Water chemistry . . . 158

B.2 Pitzer model . . . 161

B.3 Electrochemistry . . . 165

B.4 Mass transport model . . . 167

C Publishing permissions **168**

Bibliography **198**

List of Figures

1.1 CO_2 corrosion diagram. 21

2.1 Diagram of the general algorithm used by the Semi-local Corrosion Approximation model. 30

2.2 1-dimensional diagram of the mass transport, diffusion and reaction layer for a steel surface with (top) and without (bottom) corrosion scale. 36

2.3 Cross section of the 3-dimensional simulation cell. Square represents on of the three phases: steel (gray), scale (dark red) and water (cyan). Steel squares marked with a C are candidates to be dissolved in the next iteration cycle. Water squares marked with a P are sites where precipitation may take place in the next iteration cycle. 54

2.4 Standard Deviation of the corrosion rate, precipitation rate, surface coverage and equivalent porosity at pH 5 and pH 6. Simulation conditions: 80 °C, 1 bar, 1% NaCl, 1 m^{-1} A/V and 1000 rpm RCE. 60

2.5 Mean corrosion rate, precipitation rate, surface coverage and equivalent porosity at pH 5 and pH 6. Simulation conditions: 80 °C, 1 bar, 1% NaCl, 1 m^{-1} A/V and 1000 rpm RCE. 61

2.6 Mean corrosion rate, precipitation rate, surface coverage and equivalent porosity for a square cell width of 20, 40 and 60 voxels. Simulation conditions: 80 °C, pH 6, 1 bar, 1% NaCl, 1 m^{-1} A/V and 1000 rpm RCE. 62

2.7 Standard Deviation of the corrosion rate, precipitation rate, surface coverage and equivalent porosity for a square cell width of 20, 40 and 60 voxels. Simulation conditions: 80 °C, pH 6, 1 bar, 1% NaCl, 1 m^{-1} A/V and 1000 rpm RCE. 63

2.8 Standard Deviation and mean of the corrosion rate as a function of the number of voxels in the xy plane. Simulation conditions: 80 °C, pH 6, 1 bar, 1% NaCl, 1 m^{-1} A/V and 1000 rpm, 2 cm RCE. 63

3.1 Comparison between the corrosion rates from the experimental results from Tanupabrungsun [1] (dashed line) and the model predictions (solid line) under the same conditions. 71

3.2 Predicted precipitation rates for 100, 500 and 1000. Simulation conditions: 120 °C, pH 4, 5.2 bar, 1% NaCl and 0.63 m^{-1} A/V and a 2 cm diameter RCE. 72

3.3 Cross-sections and porosity profiles of the 3-dimensional simulation cells after 20 hours of simulation for 100, 500 and 1000 $m\,s^{-1}$. Simulation conditions: 120 °C, pH 4, 5.2 bar, 1% NaCl and 0.63 m^{-1} A/V 73

3.4 Model predictions of corrosion rate (solid line), precipitation rate (dashed line), bulk $[Fe^{2+}]$ and bulk pH for pH 5.4, 6 and 6.6. Simulation conditions: 80 °C, 1 bar, 1% NaCl and 1 m^{-1} A/V. 74

3.5 Model predictions of surface coverage (solid line), equivalent porosity (dashed line), scale weight and scale thickness for pH 5.4, 6 and 6.6. Simulation conditions: 80 °C, 1 bar, 1% NaCl and 1 m^{-1} A/V. 75

3.6 Cross-sections and porosity profiles of the 3-dimensional simulation cells after 120 hours of simulation for pH 5.4, 6 and 6.6. Simulation conditions: 80 °C, 1 bar, 1% NaCl, 1 m^{-1} A/V. 76

3.7 Model predictions of corrosion rate (solid line), precipitation rate (dashed line), bulk $[Fe^{2+}]$, bulk pH and bulk supersaturation for A/V ratios of 0.1, 1 and 10 m^{-1}. Simulation conditions: 80 °C, 1 bar, pH 5.8, 1% NaCl. 78

3.8 Cross-sections and porosity profiles of the 3-dimensional simulation cells for A/V ratios of 0.1, 1 and 10 m^{-1} after 120 hours. Simulation conditions: 80 °C, 1 bar, pH 5.8, 1% NaCl. 79

3.9 Model predictions of corrosion rate (solid line), precipitation rate (dashed line), bulk $[Fe^{2+}]$ and bulk pH at 60, 70 and 80 °C. Simulation conditions: 1 bar, pH 6, 1% NaCl and 1 m^{-1} A/V. 81

3.10 Cross-sections and porosity profiles of the 3-dimensional simulation cells at 60, 70 and 80 °C after 120 hours of simulation. Simulation conditions: 1 bar, pH 6, 1% NaCl and 1 m^{-1} A/V. 82

3.11 Model predictions of corrosion rate (solid line), precipitation rate (dashed line), bulk [Fe^{2+}] at 1, 2 and 3 bar. Simulation conditions: 80 °C, pH 6, 1% NaCl and 0.1 m^{-1} A/V. 83

3.12 Cross-sections and porosity profiles of the 3-dimensional simulation cells after 120 hours of simulation at 1, 2 and 3 bar. Simulation conditions: 80 °C, pH 6, 1% NaCl and 0.1 m^{-1} A/V. 84

4.1 Matrix of heatmaps displaying the corrosion rate after 120 hours of simulation as a function of two of the following three parameters: temperature, pressure and pH. The third unused parameter is represented across each row of the matrix. Simulation conditions: 1% NaCl, 1 m^{-1} A/V, and a 2 cm diameter rotating disc electrode (RCE) at 1000 rpm. 89

4.2 Matrix of heatmaps displaying the corrosion scale surface coverage after 120 hours of simulation as a function of two of the following three parameters: temperature, pressure and pH. The third unused parameter is represented across each row of the matrix. Simulation conditions: 1% NaCl, 1 m^{-1} A/V and a 2 cm diameter RCE at 1000 rpm. 92

4.3 Matrix of heatmaps displaying the porosity after 120 hours of simulation as a function of two of the following three parameters: temperature, pressure and pH. The third unused parameter is represented across each row of the matrix. Simulation conditions: 1% NaCl, 1 m^{-1} A/V and a 2 cm diameter RCE at 1000 rpm. 93

4.4 Matrix of heatmaps displaying the volume of steel lost after 120 hours of simulation as a function of two of the following three parameters: temperature, pressure and pH. The third unused parameter is represented across each row of the matrix. Simulation conditions: 1% NaCl, 1 m^{-1} A/V and a 2 cm diameter RCE at 1000 rpm. 95

5.1 Model predictions of the corrosion rate, corrosion scale surface coverage and equivalent porosity. Simulation conditions: 80 °C, pH 6.5, 1 bar, 1% NaCl, 1 m^{-1} A/V and 1 m/s in a 0.2 m diameter pipe. 100

5.2 Model predictions of the corrosion rate, precipitation rate, surface coverage, bulk pH, equivalent porosity and $FeCO_3$ supersaturation (SS_{FeCO_3}) for a 3-day simulation at 80 °C, pH 6.5, 1 bar, 1% NaCl, 1 m^{-1} A/V and 1 m/s in a 0.2 m diameter pipe followed by a water chemistry reset, a change in temperature to 70 °C, 80 °C and 90 °C and another 3-day simulation. 102

5.3 Model predictions of the corrosion rate, precipitation rate, surface coverage, bulk pH, equivalent porosity and SS_{FeCO_3} for a 3-day simulation at 80 °C, pH 6.5, 1 bar, 1% NaCl, 1 m^{-1} A/V and 1 m/s in a 0.2 m diameter pipe followed by a water chemistry reset, a change in pH to pH 5.5, pH 6 and pH 6.5 and another 3-day simulation. 103

5.4 Model predictions of the corrosion rate, precipitation rate, surface coverage, pH, bulk $[Fe^{2+}]$ and SS_{FeCO_3} for a 3-day simulation at 80 °C, pH 6.5, 1 bar, 1% NaCl, 1 m^{-1} A/V and 1 m/s in a 0.2 m diameter pipe followed by a water chemistry reset, a change in temperature to 70 °C, 80 °C and 90 °C and another 3-day simulation. 105

5.5 Model predictions of corrosion rate, surface coverage and equivalent porosity for 1 bar, 2 bar and 3 bar. Simulation conditions: 80 °C, 1% NaCl, 1 m^{-1} A/V and 1000 rpm. 109

5.6 Cross-sections and porosity profiles of the 3-dimensional simulation cells after 120 hours of simulation for 60, 70 and 80 °C. Simulation conditions: 80 °C, 1 bar, pH 6, 1% NaCl, 1 m^{-1} A/V and 1000 rpm. 110

6.1 α-Fe body-centered cubic crystal structure 127

6.2 Top view of the Fe(100), Fe(110) and Fe(111) facets. 129

6.3 α-Fe surface energy of (100), (110) and (111) facets as a function of the atomic layers of the slab 130

6.4 Top view of the Fe(111) highlighting the high symmetry sites: on-top (OT), long-bridge (LB), short-bridge (SB) and, 3-fold hollow (TH). 132

6.5 Geometry optimised atomistic models of the adlayer structures identified by Erley [2] using the PBE functional. 133

6.6 Distances between the four outermost atomic layers of a Fe(110) p(1x1) slab for the four high symmetry sites: on-top (T), long-bridge (LB), short-bridge (SB) and, 3-fold hollow (TH). The distances are expressed relative to the distances at the bulk. 138

6.7 Distances between the four outermost atomic layers of a Fe(110) p(1x1) slab. The distances are expressed relative to the distances at the bulk. 140

6.8 (A) Fe 2p and (B) O 1s X-ray photoelectron spectroscopy (XPS) spectra ($h\nu$ = 1486.6 eV, θ E = 0) acquired from four ordered phases formed on Fe(110) following exposure to either O2, CO2, or H2O. Details of exposure (in mbar/s), substrate temperature (in K), and the resulting surface unit cells (matrix notation) are indicated. Each spectrum has been normalised to have a maximum (minimum) intensity of 1 (0). Insets (top left of each panel) show superimposition of spectra displayed in panel. Also shown is the best fit (blue markers) to the bottommost O 1s spectrum, using an LF line shape function (broken red lines) and a Shirley-type background. Source: Acres et al.[3]. Figure reproduced with permission of the rights holder, John Wiley & Sons. 143

6.9 To the left, schematic plan and side views of Fe(110) (2 x 2)-O structure used to generate DFT-PDOS.The O atoms are located in their most energetically favourable adsorption sites, as determined from DFT modelling. Atom labels are employed to identify the source of plotted DFT-PDOS. To the right O, Fe1, Fe2 and Fe3 DFT-PDOS ($-2eV \geq E_F \geq 2eV$) from an optimised five-layer Fe(110) (2 x 2)-O slab. DFT, density functional; PDOS, projected electronic density of states. Source: Acres et al.[3]. Figure reproduced with permission of the rights holder, John Wiley & Sons. 144

6.10 Top view of the Fe(100), Fe(110) and Fe(111) facets. 145

List of Tables

6.1 Iron bulk properties 129

6.2 Surface density and energy of iron facets 131

6.3 CO/Fe(110) high frequency peak 133

6.4 Computation time difference between exchange-correlation functionals 134

6.5 Adsorption energy in $\mathrm{J\,m^{-2}}$ of oxygen adsorbed onto Fe(110) p(1x1) symmetric slabs for different thicknesses (atomic layers) and different adsorption sites . 137

A.1 Vibrational frequencies in $\mathrm{cm^{-1}}$ of C-O adsorbed on Fe(110) at 0.25 ML . . . 156

A.2 Vibrational frequencies in $\mathrm{cm^{-1}}$ of C-O adsorbed on Fe(110) at 0.5 ML . . . 157

B.1 References of temperature dependent physicochemical properties 158

B.2 Thermodynamic equilibrium constants of the homogeneous reactions involved in CO_2 corrosion. 159

B.3 Thermodynamic equilibrium constants of the homogeneous rections involved in CO_2 corrosion. 160

B.4 References for $\beta^{(0)}$, $\beta^{(1)}$ and $\beta^{(2)}$ 164

B.5 References for $\beta^{(0)}$, $\beta^{(1)}$ and $\beta^{(2)}$ 164

B.6 References for the ternary intercation term ψ 164

Chapter 1

Introduction

Corrosion is a natural process that causes metals to degrade and deteriorate posing major safety and financial issues across many industries.[4] The yearly global cost of corrosion was estimated at $2.5 trillion; 3.4% of the world's GDP in 2013.[5,6] In the oil and gas industry a corrosion related accident not only results in financial loss but it can also cause a serious environmental hazard. According to the U.S. Department of Transport, in the past decade corrosion was the primary cause of accidents impacting people and the environment in the U.S. 70% of the accidents that could be prevented during an integrity inspection were related to corrosion with roughly an even split between internal (pipeline inner surface) and external (pipeline outer surface) corrosion accidents.[7] Therefore, plenty of research is devoted to study the corrosion process and develop new tools and strategies to detect and prevent corrosion damage.[8–11]

Pipelines have been used for over a century as a reliable way of transporting crude oil, natural gas and petroleum-derived products.[12] The vast majority of pipes are still made of

carbon steel. This is because it is a relatively cheap material with good mechanical and welding properties, it is compatible with a wide variety of corrosion resistance strategies and it has been studied thoroughly for decades providing the trust and confidence required by the oil and gas industry.[13] However, carbon steel pipelines are susceptible to corrosion and corrosion detection and mitigation strategies are expensive to implement and maintain. This is particularly problematic for internal corrosion where corrosion typically develops faster and inspections of the pipe for corrosion damage are challenging.

The conditions inside the pipeline can be categorised into sulfide and sulfide-free environments most commonly known as sour and sweet (or CO_2) environments respectively. Sour environments contain high levels of sulfides—mainly H_2S—and exhibit more aggressive corrosion. In contrast, sweet environments have a low concentration of sulfides and the corrosion is milder compared to sour corrosion. However, currently the majority of the oilfield failures are caused by sweet corrosion due to the lack of reliable models to predict this type of corrosion.[14,15] Indeed, while numerous models have been proposed over the years some of the fundamental processes involved in sweet corrosion are not yet fully understood resulting in models with poor forecasting capabilities. Therefore, this project aims to expand our understanding of sweet corrosion by both using existing modelling tools and developing novel modelling techniques.

1.1 CO2 corrosion

CO_2 (or sweet) corrosion refers to the oxidation process of iron in the presence of CO_2 gas. The two main electrochemical reactions are the oxidation of Fe to Fe^{2+} at the anode

$$Fe_{(s)} \rightleftharpoons Fe^{2+}_{(aq)} + 2\,e^- \quad \{1\}$$

and the hydrogen evolution reaction (HER) at the cathode.

$$H^+_{(aq)} + 1\,e^- \rightleftharpoons \frac{1}{2}\,H_{2(g)} \quad \{2\}$$

The CO_2 gas dissolves in the water phase and hydrates to give carbonic acid:

$$CO_2\,(g) \rightleftharpoons CO_2\,(aq) \quad \{3\}$$

$$CO_2\,(aq) + H_2O \rightleftharpoons H_2CO_3 \quad \{4\}$$

The carbonic acid can then dissociate into HCO_3^- and CO_3^{2-} losing one proton at each step:

$$H_2CO_3 \rightleftharpoons H^+ + HCO_3^- \quad \{5\}$$

$$HCO_3^- \rightleftharpoons H^+ + CO_3^{2-} \quad \{6\}$$

The equilibria established between Reactions {3} to {6} is known as the carbonate equilibria and it plays a key role in CO_2 corrosion as explained below.

Despite the rate of corrosion being demonstrably higher in the presence of CO_2 there has been much debate over the past decade on the specific mechanism responsible for this increase. The two main mechanisms under discussion are (I) the direct reduction reaction of H_2CO_3

and (II) the ability of H_2CO_3 to act as a reservoir of H^+ due to its weak acid properties, also known as the *buffering* effect.[16] As of the writing of the present work the consensus is that the contribution of the H_2CO_3 direct reduction to the total cathodic current is negligible and the *buffering* effect is the major contributor to the increase in corrosion rate in sweet environments.[17–21]

While the additional protons are provided by the deprotonation of H_2CO_3 (Reaction {5}) and, to a lesser extent, the deprotonation of HCO_3^- (Reaction {6}) both of these reactions are limited by the slow CO_2 hydration reaction (Reaction {4}).[22,23] Therefore, the three major factors limiting the HER are (I) the mass transport of H^+ (II) the mass transport of H_2CO_3 and (III) the kinetics of the CO_2 hydration reaction.[23]

1.2 Corrosion product layer

During the corrosion process a film may sometimes form over the corroding metal surface as a by-product of the corrosion reaction, the *corrosion scale*. Such a film may protect the metal surface from further corrosion (surface passivation) so they are utilised as an additional cost-effective mitigation strategy in many industries. The level of protection is often linked to the structural properties of the film which are determined by the type of metal substrate and the conditions under which the film formed.[24,25]

In CO_2 corrosion the oxidation reaction releases Fe^{2+} ions into solution where they combine with CO_3^{2-} ions and precipitate on top of the steel surface as $FeCO_3$ in the siderite crystalline phase.[14] Figure 1.1 shows a diagram of the different chemical and electrochemical reactions involved in CO_2 corrosion.

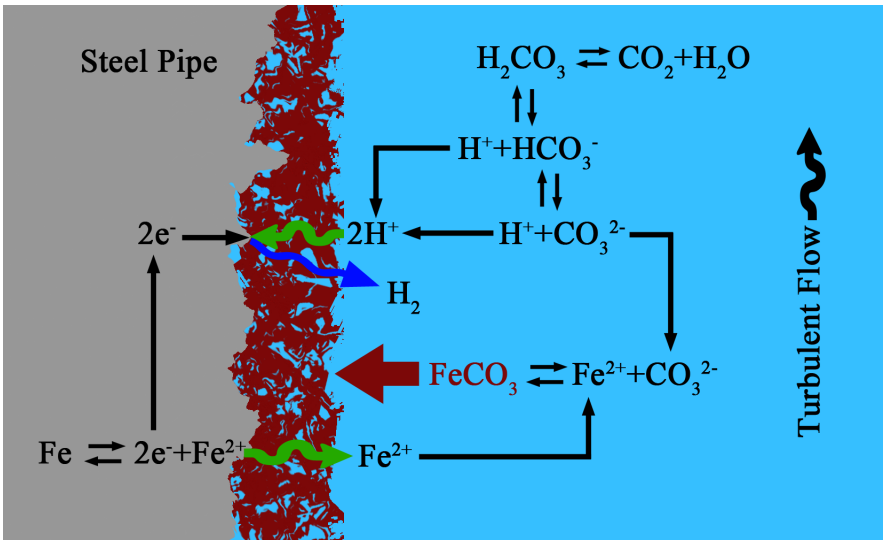


Figure 1.1: CO_2 corrosion diagram.

This film protects the steel surface via two different mechanisms: (I) the film creates a diffusion barrier for the electroactive species moving away and towards the steel surface and (II) the film covers the steel surface thereby blocking active corrosion sites.[26] The degree of protection offered by these two mechanisms is determined by the physical properties of the corrosion scale such as the density, morphology and surface coverage which are observed to be determined by the corrosion and precipitation rates during formation the formation of the scale.[16,16,27–30] When the precipitation rate is higher than the corrosion rate a dense uniform film forms on the metal surface. When the corrosion rate is higher than the precipitation rate the corrosion "undermines" the corrosion scale resulting in a thick porous film with poor protective properties. This is typically characterised by the *scaling tendency* (ST), a ratio between the precipitation rate and corrosion rate.[25] Additionally, the stability of the film is key to maintain the corrosion protection as changes in the environment can result in the degradation of the corrosion scale or its detachment from the steel surface.

While compact and dense scales are generally deemed as "protective" based on short-term experiments (less than a week) long-term corrosion experiments are still lacking even though

they are key to validate the current consensus on protective scales. Furthermore, the formation process of the scale is still not fully understood and thus it is not trivial to predict which environments promote the formation of a protective scale.

The goal of the present work is to improve our understanding of the corrosion process and corrosion scale formation by using existing modelling methods as well as developing new modelling techniques that can overcome the limitations of the current models.

1.3 CO2 corrosion models: a review

New tools and strategies for the prevention and mitigation of corrosion are continuously developed to reduce its costly and sometimes catastrophic consequences.[9,10] Predictive corrosion models play a key role in these developments as they are used to evaluate the risk of corrosion and assess the lifespan and maintenance of equipment and components susceptible to it.

CO_2 corrosion models are generally based on the assumption that there is no charge buildup at the metal surface and thus the sum of cathodic currents must equal the sum of anodic currents:

$$\sum_i i_{a,i} = \sum_j i_{c,j} \tag{1.1}$$

i_a and i_a are typically expressed as a function of the applied potential (E). The potential at which Eq. (1.1) holds true is known as the corrosion potential (E_{corr}) which is typically obtained using numerical methods such as the Newton-Raphson method when an analytical solution doesn't exist. Then, the corrosion current (i_{corr}) can be obtained by adding up all anodic (or cathodic) currents.

Many CO_2 corrosion models have been developed over the past decades. The first CO_2 corrosion model was introduced by De Waard and Milliams[31] in 1975. They proposed the following mechanism for the cathodic reaction:

$$H_2CO_{3(aq)} + e^- \longrightarrow HCO^-_{3(aq)} + H_{2(gas)} \quad \{7\}$$

$$H^+ + HCO_3^- \rightleftharpoons {}_2CO_3 \quad \{8\}$$

This mechanism assumes that the direct reduction of the carbonic acid is the main cathodic reaction when CO_2 is present in the environment. Their model is based on a linear approximation of the pH dependence of the log of the corrosion current (i_{corr}):[31]

$$\log i_{\text{corr}} = -A \text{ pH} + B \tag{1.2}$$

The parameters A and B are related with the Tafel slopes of the cathodic and anodic reactions and the reaction rates respectively and can obtained by fitting experimental data to the equation experimentally. De Waard and Milliams[31] correlated the pH with the partial pressure of CO_2 (p_{CO_2}) to obtain a relation for the corrosion current as a function of the partial pressure of CO_2:

$$\log i_{\text{corr}} = -\frac{1}{2}A \ \log p_{CO_2} + B \tag{1.3}$$

While this initial model has a mechanistic (albeit simplistic) foundation later iterations of this model included empirical corrections to account for additional effects such as the flow rate or the corrosion scale.[32–35] Therefore, later versions of the model are considered *semiempirical*.[36]

The next generation of CO_2 corrosion models include a mechanistic description of additional physicochemical processes that influence the corrosion rate such as other important electrochemical reactions (particularly at the cathode) and the mass transport of species

between the bulk of the solution and the reactive surface. Moreover, the water chemistry of the solution and the concentration of species at the reactive surface are key components of these new models as the concentration of carbonic acid in solution was considered to play a key role in the CO_2 corrosion process. The models developed by Gray et al.[37] and Dayalan et al.[38] are amongst the first examples of such models with the most complete model being developed by Nesic et al.[39] in 1996 which included the H^+, H_2CO_3, H_2O reduction reactions and identified the hydration reaction as the limiting process of the carbonic acid reduction.

While these models are based on sound mechanistic foundations they predict a constant corrosion rate for a specific set of conditions. However, CO_2 corrosion is a dynamic process and the evolving solution chemistry and the possible formation of a corrosion scale can influence the corrosion rate as a function of time. Therefore, some more advanced models have been developed to make time-dependent predictions of the corrosion rate starting from a set of initial conditions. These models describe the mass transfer, electromigration, flow and electrochemical and homogeneous reactions via the Nerst-Planck relation:

$$\frac{\partial C_i}{\partial t} = -\nabla N_i + R_i \tag{1.4}$$

where C_i is the concentration of species i, N_i is the flux of species i and R_i is the source or sink that accounts for all the chemical and electrochemical reactions that the species i is involved in. While the first CO_2 corrosion models that used this approach were somewhat limited (Turgoose et al.[40], Pots[41]) the more comprehensive model developed by Nordsveen et al.[42] in 2003 is considered a milestone in CO_2 corrosion modelling due to the improved description of the electrochemical and homogeneous chemical reactions. The model also included a simplified description of the corrosion scale that was added in later publications.[26,43]

Later studies focused on incremental improvements to the electrochemical, homogeneous

and heterogeneous chemical reactions to widen the range of conditions where the model is valid.[16,23,44]

While CO_2 corrosion modelling have seen major improvements over the last decades current CO_2 corrosion models still present some shortcomings. Firstly, current CO_2 corrosion models are 1-dimensional which is enough to model *general* (or uniform) corrosion but struggle to describe 3-dimensional processes such as localised corrosion and corrosion scale growth. Secondly, since current CO_2 corrosion models models are deterministic they cannot account for the stochastic nature of the corrosion process.

Chapter 2 of the present work describes a new corrosion modelling technique that aims to overcome the aforementioned issues related to CO_2 corrosion modelling. It features a 3-dimensional simulation cell that represents the corroding surface and is coupled with a stochastic model that introduces a random component into the corrosion and scale formation process.

Chapter 3 analyses the time-series predictions obtained from the model and compares the results with the current understanding of CO_2 corrosion.

Chapter 4 explores the outcomes of the corrosion process after 2 days for a wide range of different conditions aiming to understand the complex patterns and interactions between the different initial conditions of the corrosion environment.

Chapter 5 showcases the possibilities that this new modelling technique offers by studying two additional use cases of the model. The first use case aims to replicate a change in the environment during the course of the simulation while the second use case describes an inhibitor model that replicates the effect of inhibitors molecules blocking active corrosion

sites on the metal surface.

Finally, Chapter 6 shifts the scope to the atomistic scale. To improve the description of corrosion models it is important to have a clear understanding of the fundamental processes that govern the corrosion reaction. This last chapter studies the initial stages of the corrosion process while laying down the foundations for future research in this area.

Chapter 2

Semi-local Corrosion Approximation

2.1 Introduction

During the corrosion process a film may sometimes form over the corroding metal surface as a by-product of the corrosion reaction. This film can play a key role in the protection of the surface against corrosion but it is generally omitted or oversimplified in 1-dimensional corrosion models. More advanced techniques can be used to incorporate a local description of the processes but the additional cost currently prevents these methods from being used for predictions that address practical length and time scales.[45–48] It is the purpose of the current work to introduce a new efficient and accurate model of corrosion scale growth that predicts heterogeneous scale growth at realistic length and time scales.

Predictive CO_2 corrosion models typically estimate the general (or uniform) corrosion rate by solving complex partial differential equations in a continuous 1-dimensional system

disregarding any stochastic or local surface phenomena.[36,39,42,49,50] Some of these models have attempted to incorporate the formation of a corrosion scale but modelling such complex structures explicitly is challenging and therefore significant assumptions are adopted when describing the internal structure of the scale.[26,51–53] These 1-dimensional models typically consider the formation and growth of the scale as a homogeneous process across the surface which renders them unable to capture the heterogeneous and stochastic nature of both scale growth and the resultant scale structure. Nevertheless, many studies have emphasised the major impact that the presence of the scale has on the overall corrosion rate thus an appropriate representation of the scale is crucial to model CO_2 corrosion under scaling conditions.[25,54]

Corrosion scales are made of a combination of amorphous and crystalline material creating a hierarchical multi-length scale structure that exhibits complex growth patterns and generates complex fluid dynamics. The importance of a microscopic description of the scale has been recently demonstrated by theoretical models in similar systems where the mass transport across the grain boundaries has been shown to play a significant role in the oxidation process.[55] There is therefore a need to extend current models of scale growth to improve the description of the heterogeneous structure and its formation through stochastic and environmentally influenced process.

Cellular Automaton (CA) models have been successful at describing many heterogeneous and stochastic phenomena at relatively large scales including localised corrosion and metal passivation.[47] This modelling technique discretises space, time and state and defines a set of local rules that attempt to mimic physical and chemical processes. It is also trivial to model stochastic processes by assigning a probability to a rule. However, CA models are not always suitable as a predictive tool because the parameters used in their local rules are not typically modelled by a physically motivated equation, hence, they must be calibrated using

experimental data.[56,57] This constrains the predictive power of CA models to a limited range of conditions as the parameters are not usually transferable from one system to another.

To overcome the limitations of the general corrosion models and CA models we introduce here a new modelling technique has been developed to improve the predictive power of current corrosion models and provide new insights into corrosion under scaling conditions, the *Semilocal Corrosion Approximation* (SLCA) . This is achieved by assuming a pseudo-local equilibrium in a discretised 3-dimensional space and time where the system is evolved locally by applying a validated *general* corrosion electrochemical model that is explicitly dependent on local conditions and coupled with a stochastic model of the corroding surface.

2.2 Semi-local Corrosion Approximation

The Semi-local Corrosion Approximation model can be divided into five parts: a water chemistry model that calculates the concentration of species, an electrochemistry model that computes the corrosion rate, a precipitation model that predicts the precipitation of corrosion product, a mass transport model used to obtain the mass transport coefficients for a given flow system and a stochastic model that controls the corrosion and precipitation processes at the micro scale. The model is packaged in a `C++` binary and can run under all OS platforms. Figure 2.1 shows a diagram of the general algorithm used by the software. After reading the input parameters into the model and computing the initial conditions the 3-dimensional cell, the species concentrations, the mass transport coefficients, the corrosion rate and precipitation rate are updated in this order. Finally, the simulation time is updated and the cycle is repeated until the time reaches the set time limit. The following sections will describe the different models in detail and how these are linked together. The models adopted here are

described for the specific example of CO_2 corrosion.

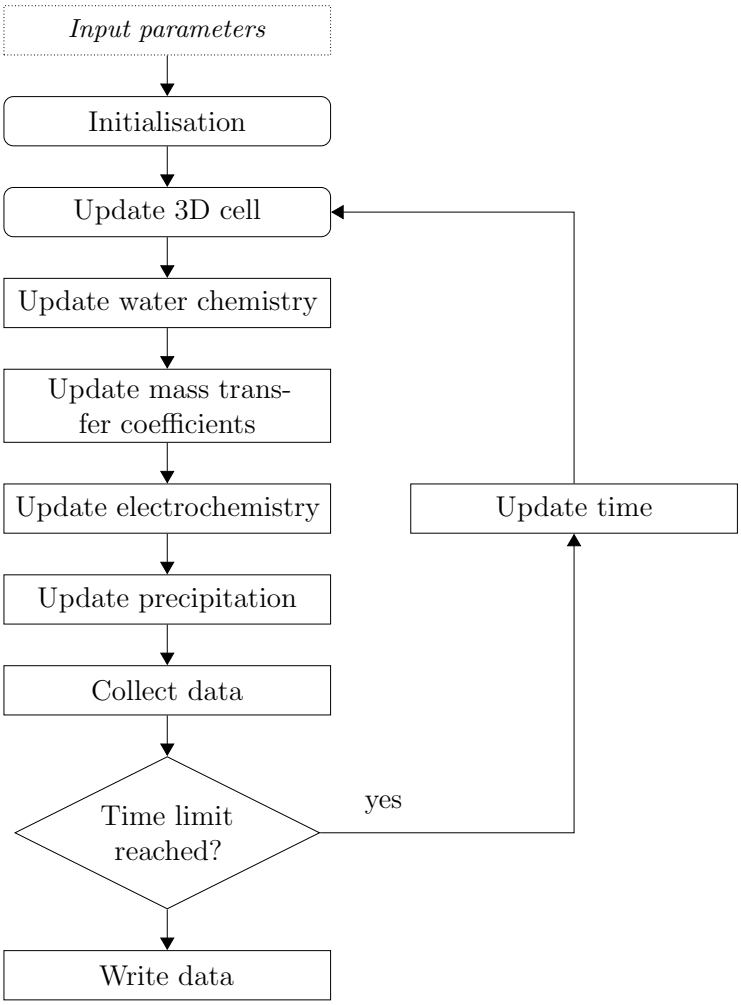


Figure 2.1: Diagram of the general algorithm used by the Semi-local Corrosion Approximation model.

2.2.1 Water chemistry

In order to estimate the concentration of aqueous species in CO_2 corrosion one can adopt models of thermodynamic equilibrium and the underlying reaction kinetics. The accuracy of this model depends strongly on the thermodynamic and kinetic constants of the reactions involved. Often obtaining these constants experimentally is challenging and the methods used

have been refined and improved over many years.[36,42,44] The current model is modular and flexible incorporating the latest reported values of thermodynamic and kinetic constants.

The thermodynamic constants of the homogeneous chemical Reactions {3} to {6} used by the model are defined in Appendix B.1.

At high ionic strength the solution no longer behaves as an ideal mixture and the activity coefficients of the ionic species present in solution may differ significantly from unity and, hence, have to be explicitly calculated. This includes the intrinsic species Fe^{2+}, H^{+}, OH^{-}, HCO_3^{-}, CO_3^{2-} and any other ionic species present in the solution. In the present work, the activity coefficients of the ions and the solvent are obtained using the Pitzer model; a set of thermodynamic equations that express the interaction between ions in complex mixtures as a combination of the ionic interactions in simpler mixtures for which the experimental data is readily available.[58] The model has been used recently in other CO_2 corrosion models.[44,50] The Pitzer equations and the parameters used are described in (Appendix B.2). In the current work the solution is assumed to be electroneutral. The validity of this assumption depends on the magnitude of the corrosion rate. At higher corrosion rates the system will take longer to reach a state of pseudo-equilibrium compared to a slow and steady corrosion rate where the transient stage is shorter. For a CO_2−H_2O system with no additional ions the charge balance results in the constraint:

$$[H^{+}] + 2[Fe^{2+}] = [OH^{-}] + [HCO_3^{-}] + 2[CO_3^{2-}] \tag{2.1}$$

where [X] is the concentration of species X. Under the assumption of thermodynamic equilibrium the concentration of $[H^{+}]$, $[OH^{-}]$, $[HCO_3^{-}]$ and $[CO_3^{2-}]$ are determined by the thermodynamic equilibrium constants listed in Table B.2. As a consequence, for a known $[Fe^{2+}]$ the $[H^{+}]$ can be obtained by solving Eq. (2.1) with all carbonate species concentrations expressed

as a function of $[H^+]$. Since thermodynamic equilibrium is assumed the water chemistry model does not take into account reaction kinetics.

The model can fix the initial pH of the solution by simulating the addition of a strong acid or base to the solution and including the conjugated acid or base to the charge balance equation (Eq. (2.1).

2.2.2 Electrochemical model

CO_2 corrosion consists of two main electrochemical reactions: the oxidation of Fe to Fe^{2+} at the anode (Reaction {9}) and the HER at the cathode (Reaction {10}).

$$\mathrm{Fe_{(s)}} \rightleftharpoons \mathrm{Fe^{2+}_{(aq)}} + 2\,\mathrm{e^-} \qquad \{9\}$$

$$\mathrm{H^+_{(aq)}} + 1\,\mathrm{e^-} \rightleftharpoons \frac{1}{2}\,\mathrm{H_{2(g)}} \qquad \{10\}$$

The HER (cathodic) current density (i_{HER}) can be calculated from the cathodic charge-transfer current density (i_{ct}) equation as:[59,60]

$$i_{\mathrm{HER}} = i_{\mathrm{ct}} = i_0 \exp\left(-\frac{\alpha F}{RT}\Delta E\right) \qquad (2.2)$$

where i_0 is the *exchange* current density, α is the charge transfer coefficient, F is the Faraday constant, R is the ideal gas constant, T is the temperature and $\Delta E = E - E_0$ where E is the electrostatic potential and E_0 is the potential at the equilibrium. The *exchange* current density is the current exchanged between a redox couple at equilibrium potential (E_0). For

the HER the first-order reaction exchange current density equation is used here:[59]

$$i_{0,\mathrm{HER}} = F k_{\mathrm{HER}} c_{m,\mathrm{H^+}} \exp\left(- \frac{\alpha_{\mathrm{HER}} F E_{0,\mathrm{HER}}}{RT} \right) \tag{2.3}$$

where $c_{m,\mathrm{H^+}}$ is the $\mathrm{H^+}$ concentration at the reactive surface and k_{HER} is the reaction rate constant of the HER. The temperature dependence of k_{HER} can be modelled using an Arrhenius-like relation:

$$k = k_{\mathrm{ref}} \exp\left(\frac{-\Delta H}{R} \left(\frac{1}{T} - \frac{1}{T_{\mathrm{ref}}} \right) \right) \tag{2.4}$$

where k_{ref} is the value of k at temperature T_{ref} and ΔH is the enthalpy of the reaction.

The protons involved in the HER originate from two independent sources: the protons already in the solution and the protons stored in the form of carbonic acid ($\mathrm{H_2CO_3}$). The protons already in solution reach the surface via mass-transfer while the protons stored as $\mathrm{H_2CO_3}$ are transported to the surface as $\mathrm{H_2CO_3}$ which subsequently deprotonates releasing $\mathrm{H^+}$. Furthermore, the carbonic acid supply is limited by the slow $\mathrm{CO_2}$ hydration reaction (Reaction {4}). Therefore, the i_{HER} can be divided into two components in terms of proton sources:

$$i_{\mathrm{HER}} = i_{\mathrm{mt}} + i_r \tag{2.5}$$

where i_{mt} is the $\mathrm{H^+}$ mass-transfer current and the i_r combines the $\mathrm{H_2CO_3}$ mass-transfer and the $\mathrm{CO_2}$ hydration reaction that limits the supply of $\mathrm{H_2CO_3}$. Both components are described below.

The model adopts the diffusion layer approximation proposed by Nernst[61] and Brunner[62] in 1904 whereby the diffusion of electroactive species only takes place within a *diffusion layer* (δ_m) of stationary liquid irrespective of the flow conditions.[63] For the mass transport of $\mathrm{H^+}$

the diffusion layer approximation is defined as:

$$J_{\mathrm{H^+}} = -D_{\mathrm{H^+}} \frac{c_{b,\mathrm{H^+}} - c_{m,\mathrm{H^+}}}{\delta_{m,\mathrm{H^+}}} \tag{2.6}$$

where $J_{\mathrm{H^+}}$ is the flux of $\mathrm{H^+}$ $D_{\mathrm{H^+}}$ is the $\mathrm{H^+}$ diffusion coefficient $c_{b,\mathrm{H^+}}$ and $c_{m,\mathrm{H^+}}$ are the bulk and steel surface concentrations of $\mathrm{H^+}$ respectively and $\delta_{m,\mathrm{H^+}}$ is the $\mathrm{H^+}$ diffusion layer.

The diffusion layer separates the surface concentration and the bulk concentration of the electroactive species and assumes a constant flux throughout the layer under steady state conditions. Despite its simplicity, numerous experimental studies have verified the validity of the model.[63] The electromigration of ions can be neglected for solutions with an excess of supporting electrolyte.[63,64] Since the solutions encountered in the oil and gas industry generally have high concentrations of multiple salts the current model neglects electromigration, hence the model is restricted to solutions with enough salt in them to consider the electromigration contribution negligible. While this implies that experiments with no additional salt cannot be adequately described by the model, from an experimental point of view it is trivial to use a non-interacting electrolyte in corrosion experiments.

Generally, δ_m is not known so it is often combined with the diffusion coefficient to define a new constant, the *mass-transfer* coefficient ($k_{\mathrm{mt}} = D/\delta_m$); a measure of the speed at which species diffuse from the bulk of the solution to the surface of the electrode.[64] The mass-transfer coefficients used by the current model are described in Section 2.2.4.

The current density can be obtained from the flux using the following relation:

$$i_j = n_j F J_j \tag{2.7}$$

where n_j is the charge of species j, F is the Faraday constant and J_j is the flux of species j. Therefore, the mass transport current density (i_{mt}) associated with the mass-transfer of H^+ from the bulk of the solution to the surface of the electrode can then be described as

$$i_{\text{mt}} = F n_{H^+} k_{\text{mt},H^+} (c_{b,H^+} - c_{m,H^+}) \tag{2.8}$$

Increasing the current density decreases the H surface concentration. When surface concentration is zero the current density has reached its upper limit also known as *limiting* mass transport current density ($i_{\text{lim,mt}}$):

$$i_{\text{lim,mt}} = F n_{H^+} k_{\text{mt},H^+} c_{b,H^+} \tag{2.9}$$

Equation (2.8) can be rewritten using the $i_{\text{lim,mt}}$ definition:

$$i_{\text{mt}} = \left(1 - \frac{c_{m,H^+}}{c_{b,H^+}}\right) i_{\text{mt,lim}} \tag{2.10}$$

In 1967, Vetter derived the following equation to describe the current density of electrochemical reactions limited by the rate of a homogeneous reaction. For the H_2CO_3 hydration reaction the equation is as follows:[63]

$$i_r = i_{r,\text{lim}} \sqrt{1 + \exp\left(\frac{2F}{RT}\Delta E\right) - 2\exp\left(\frac{F}{RT}\Delta E\right)} \tag{2.11}$$

$$i_{r,\text{lim}} = F c_{b,H_2CO_3} \sqrt{D_{H_2CO_3} k_b} \tag{2.12}$$

where F is the Faraday constant, $D_{H_2CO_3}$ is the diffusion coefficient of the H_2CO_3 and k_b is the kinetic constant of the backward limiting reaction. Eq. (2.11) assumes that the diffusion layer extends to the bulk of the solution; thus, it is valid for stagnant solutions. However, in fast flow systems where the solution is well mixed the diffusion layer and the reaction layer can

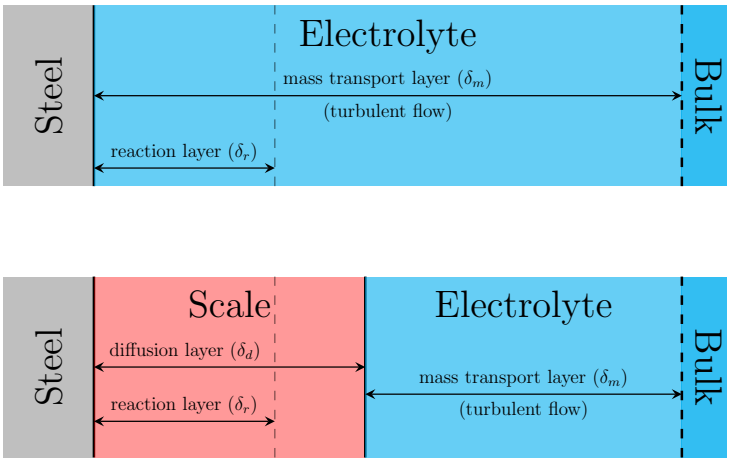


Figure 2.2: 1-dimensional diagram of the mass transport, diffusion and reaction layer for a steel surface with (top) and without (bottom) corrosion scale.

be of comparable lengths which invalidates Vetter's assumption. Nesic et al.[65] proposed an alternative derivation that includes a finite diffusion layer and results in an equation similar to Eq. (2.11) but with an extra *flow factor* (f):

$$i_{r,\text{lim}} = F c_{b,\text{H}_2\text{CO}_3} \sqrt{D_{\text{H}_2\text{CO}_3} k_b} f \tag{2.13}$$

where f is defined as

$$f = \coth\left(\frac{\delta_m}{\delta_r}\right) \tag{2.14}$$

δ_m is the thickness of the mass-transfer layer and δ_r is the thickness of the chemical reaction layer (see Appendix B.4 for how these quantities are calculated). This flow factor balances the diffusion vs reaction current densities. Figure 2.2 displays a diagram of the diffusion (δ_d), reaction (δ_r) and mass transport (δ_m) layers for a steel surface with and without a corrosion scale. The relative position of δ_d and δ_r will depend on the thickness of the scale but generally the reaction layer is only a few micrometers thick whereas the scale can grow much thicker. Substituting Eq. (2.10) in Eq. (2.5) in we can obtain an expression for the c_{m,H^+}:

$$c_{m,\mathrm{H^+}} = c_{b,\mathrm{H^+}}\left(1 + \frac{i_r - i_c}{i_{\mathrm{mt,lim}}}\right) \tag{2.15}$$

Using this relation in Eq. (2.2), the cathodic current can then be rewritten as:

$$i_c = \left(1 + \frac{i_r - i_c}{i_{\mathrm{lim,mt}}}\right) i'_0 \exp\left(-\frac{\alpha F}{RT}\Delta E\right) \tag{2.16}$$

where i'_0 is equivalent to i_0 but uses bulk concentrations instead of surface concentrations. For the HER:

$$i'_{0,\mathrm{HER}} = F k_{\mathrm{HER}} c_{b,\mathrm{H^+}} \exp\left(-\frac{\alpha_{\mathrm{HER}} F E_{0,\mathrm{HER}}}{RT}\right) \tag{2.17}$$

Solving Eq. (2.16) for i_c one can obtain the cathodic current density as a function of bulk concentrations as opposed to surface concentrations.

$$i_c = i'_{\mathrm{ct}}\left(\frac{i_r + i_{\mathrm{mt,lim}}}{i'_{\mathrm{ct}} + i_{\mathrm{mt,lim}}}\right) \tag{2.18}$$

This result contrasts with the parallel resistance model that results from a similar derivation when the H_2CO_3 reduction is assumed to be a significant component of the cathodic current.[39] However, it ultimately results in a similar behaviour, i.e. the cathodic reaction can be limited by the charge-transfer reaction or by the (reaction or mass transport) limiting current.

The anodic current density is controlled by the iron oxidation reaction. This reaction was studied by Nesic et al.[66] over a wide pH range (2-7) concluding empirically that the dependence of the reaction rate is not strongly dependent on the $[Fe^{2+}]$ in solution. However, it is dependent on $[OH^-]$ at $pH < 5$ and on CO_2 partial pressure (p_{CO_2}) from 10^{-2} to 1 bar.

$$i_a = k c_{m,\mathrm{OH^-}}^{a_1} (p_{\mathrm{CO_2}})^{a_2} \exp\left(-\frac{\alpha_a F}{RT}\eta\right) \tag{2.19}$$

where k is the rate of reaction constant, $c_{m,\mathrm{OH^-}}$ is the concentration of OH^- at the reactive

surface, a_1 and a_2 are reaction order parameters, p_{CO_2} is the partial pressure of CO_2, α_a is the anodic charge transfer coefficient and η is the applied potential.

In the present work, the corrosion potential (E_{corr}) is calculated from the assumption that a dynamic equilibrium has been reached in which there is no charge build-up during the corrosion process and therefore the total cathodic current is equal to the total anodic current. This is equivalent to the net current (i_{net}) being equal to zero.[36,39]

$$i_{net} = i_a(E_{corr}) - i_c(E_{corr}) = 0 \tag{2.20}$$

where i_a and i_c are defined in Eqs. (2.18) and (2.19) respectively and E_{corr} is the corrosion potential. Therefore, the corrosion current density can be expressed as

$$i_{corr} = i_a(E_{corr}) = i_c(E_{corr}) \tag{2.21}$$

2.2.3 Corrosion product precipitation

The mass transport of chemical species will be influenced by the morphology of the scale (if present) and the type of flow (or lack thereof).

Scale growth

The scale formed as a by-product of the CO_2 corrosion process is of great interest as it can offer protection against general corrosion by blocking corrosion sites and hindering the diffusion of

species. Therefore, an accurate model of the growth rate of the corrosion scale under different conditions is of paramount importance to optimise the protection offered by scale.

The first attempt at modelling the amount of precipitated corrosion product was led by Johnson and Tomson[67] in 1991 followed by Van Hunnik et al.[68] in 1996 who attempted to develop a more accurate equation under a wider range of supersaturation levels. In both studies the precipitation of the corrosion product was calculated indirectly by measuring the concentration of Fe_2^+ in solution, the so-called "Fe_2^+ method".[69] This method assumes that $FeCO_3$ is the main component of the precipitated corrosion product. Sun et al.[69] tested the validity of both equations in 2006 by using a more accurate method to measure the amount of precipitation on the steel surface, the weight gain/loss method, which consists in weighing the steel coupons before and after removing the corrosion scale.[69,70] Their results demonstrated that the Fe_2^+ concentration alone was insufficient to predict the weight of the corrosion product on the steel surface and suggested that not all the precipitated $FeCO_3$ deposits on the surface. Consequently, in 2008 Sun and Nešic[71] developed an alternative scale growth model which they called corrosion layer accumulation rate (CLAR) to distinguish it from the homogeneous precipitation rate equations used previously (Eq. (2.22)). The parameters of this equation were further improved in 2018 by using an Electrochemical Quartz Crystal Microbalance (EQCM) to measure *in-situ* the weight of the corrosion scale.[72] This empirical equation was reported to be significantly more reliable for predicting the time evolution of the total mass of the deposited scale and it is adopted in the present model.

$$R_{\mathrm{FeCO_3}} = k_r e^{-\frac{\Delta G}{RT}} K_{sp}(SS_{\mathrm{FeCO_3}} - 1) \tag{2.22}$$

The model uses the kinetic constant k_r and the activation energy ΔG obtained by Ma et al.[72] from a series of EQCM experiments between 50 °C and 80 °C:

$$k_r \quad = 1.8 \times 10^6\,\mathrm{m^4\,mol^{-1}\,s^{-1}}$$
$$\Delta G = 64\,851.4\,\mathrm{J}$$

The SS_{FeCO_3} is calculated as a function of the Fe_2^+ and CO_3^{2-} activities ($a_{Fe_2^+}$ and $a_{CO_3^{2-}}$ respectively):

$$SS_{FeCO_3} = \frac{a_{Fe_2^+} a_{CO_3^{2-}}}{K_{sp}} \tag{2.23}$$

The $FeCO_3$ solubility product (K_{sp}) can be obtained from the empirical equation developed by Sun, Nesic and Woollam relating the K_{sp} with the temperature (T_k) and ionic strength (I).[73,74]

$$\log K_{sp} = -59.3498 - 0.041377 T_k - \frac{2.1963}{T_k} + 24.5724 \log T_k + 2.518 I^{0.5} - 0.657 I \tag{2.24}$$

Equation (2.24) already incorporates the ionic strength dependence on the activity of Fe^{2+} and CO_3^{2-} so the activity of the species can be replaced by their concentrations.

$$SS_{FeCO_3} = \frac{c_{Fe_2^+} c_{CO_3^{2-}}}{K_{sp}} \tag{2.25}$$

A shortcoming of Eq. (2.22) is that it was fitted with SS_{FeCO_3} values obtained from the bulk of the solution and while the authors claim that in their measurements the surface SS_{FeCO_3} was not much different from the bulk SS_{FeCO_3} the model is then validated against other experiments where the difference between the bulk and the electrode surface could be significant. Furthermore, in the presence of a scale it is not obvious if one should use the SS_{FeCO_3} value of the bulk, the scale-electrolyte interface or the metal-scale interface. Since precipitation takes place throughout the scale the present model takes the mean SS_{FeCO_3} inside the scale obtained by calculating the SS_{FeCO_3} at each point of the scale from the

Fe_2^+ and CO_3^{2-} concentrations.

Scale dissolution

When the supersaturation is below 1 the scale starts dissolving. While this process is not generally modelled by CO_2 corrosion models it is an important part of the life cycle of the scale and may lead to a loss of corrosion protection under certain environments. Therefore, the present model incorporates a dissolution model.

There are not many CO_2 corrosion related studies that investigate the scale dissolution reaction. However, the dissolution kinetics of siderite have been previously studied in the geochemical sciences field.[75,76] The scale dissolution model will be based on the scale dissolution kinetics study carried out by Golubev et al.[76] . The main dissolution reactions are the irreversible carbonate surface protonation (Reaction {11}) and the reversible carbonate surface hydration (Reaction {12}).

$$\mathrm{FeCO_{3(s)}} + \mathrm{H^+_{(aq)}} \xrightarrow{k_{+,\mathrm{H^+}}} \mathrm{Fe^{2+}} + \mathrm{HCO_3^-} \qquad \{11\}$$

$$\mathrm{FeCO_{3(s)}} \underset{k_{-,\mathrm{H_2O}}}{\overset{k_{+,\mathrm{H_2O}}}{\rightleftharpoons}} \mathrm{Fe^{2+}} + \mathrm{CO_3^{2-}} \qquad \{12\}$$

Therefore, the net dissolution rate R_{diss} can be described by:

$$\begin{aligned} R_{\mathrm{diss}} &= R_{+,\mathrm{H^+}} + R_{+,\mathrm{H_2O}} - R_{-,\mathrm{H_2O}} \\ &= k_{+\mathrm{H^+}}(a_{\mathrm{H^+}})^n + k_{+\mathrm{H_2O}} - k_{-\mathrm{H_2O}} a_{\mathrm{Fe^{2+}}} a_{\mathrm{CO_3^{2-}}} \end{aligned} \tag{2.26}$$

R_+ and R_- refer to the rate of dissolution reactions and precipitation reactions respectively.

$k_{+,\mathrm{H^+}}$, $k_{+,\mathrm{H_2O}}$ and $k_{-,\mathrm{H_2O}}$ are the reaction rate constants, n the order of Reaction {11} and $a_{j,\mathrm{scale}}$ represents the activity of species j. The value of n has been reported to be 0.75 at 25 °C and very close to 1 from 60 °C to 100 °C.[76,77] Following the same assumption as in the model adopted by Golubev et al.[76] an n of 1 is used in this model.

While both Reactions {11} and {12} contribute to the dissolution of the scale $k_{+\mathrm{H^+}}$ is two orders of magnitude larger than $k_{+\mathrm{H_2O}}$, hence, Reaction {11} is generally much faster than Reaction {12} and can be neglected. The total dissolution rate (R_{diss}) can then be simplified to only include the protonation reaction.

$$R_{\mathrm{diss}} = R_{+,\mathrm{H^+}} = k_{+\mathrm{H^+}} a_{\mathrm{H^+}} \tag{2.27}$$

The temperature dependence of the reaction rate constants can be modelled using the Arrhenius equation.

$$k = k_{ref} \exp\left(\frac{-\Delta E_{act}}{R(T - T_{ref})}\right) \tag{2.28}$$

where ΔE_{act} is the activation energy, and k_{ref} is a reference reaction rate constant measured at temperature T_{ref}. Golubev et al.[76] reported a ΔE_{act} of 65 kJ mol^{-1}. Their $k_{+,\mathrm{H^+}}$ measurement at 60 °C (6.20×10^{-7} mol cm^{-2} s^{-1}) is used for $k_{+,\mathrm{H^+},ref}$.

Equation (2.27) can then be used to compute the dissolution rate at each discrete xy plane of the scale which can lead to different dissolution rates at different sections of the scale.

2.2.4 Mass transport

During the corrosion process electroactive species in the solution move away and towards the steel surface where the electrochemical reactions take place. In the oil and gas industry the solution is under constant turbulent flow. Therefore, the current model assumes that the bulk of the solution is under turbulent flow conditions which affects the mass transport of species between the bulk of the solution and the steel surface. If a corrosion scale is present the flow inside it is considered to be negligible and, hence, the mass transport is dominated by molecular diffusion. Diffusion inside the scale is influenced by the morphology, thickness and density of the scale. This section describes the mass transport models adopted for the mass transport of species inside and outside the scale.

Turbulent flow

Under turbulent flow conditions the mass transfer coefficients ($k_{\mathrm{mt},flow}$) between the bulk of the solution and the metal-electrolyte (or scale-electrolyte if a corrosion scale is present) interface are determined by the hydrodynamics of the system. Several empirical models are available in the literature for a variety of common flow types and geometries. Studies have shown these empirical equations work reasonably well in most situations.[78–81] Generally, these models correlate the Sherwood number (Sh)—a ratio of convective and diffusive mass transport— with the Reynolds number (Re)—a measure of how turbulent the flow is—and the Schmidt (Sc)—a ratio between the momentum diffusivity and mass diffusivity. For example, Eisenberg et al.[82] proposed the following equation for rotating cylinder electrodes (RCE):

$$Sh_j = 0.0791 v_L Re^{0.70} Sc_j^{0.356} \tag{2.29}$$

where Sh, Re and Sc are defined as

$$Sh_j = \frac{k_{\text{mt,flow}} L}{D_j}; \quad Re = \frac{\rho u L}{\mu}; \quad Sc_j = \frac{\mu}{\rho D_j} \tag{2.30}$$

where ρ and μ are the density and dynamic viscosity of the electrolyte u is the linear velocity of the fluid with respect to the surface of the electrode, L is the characteristic length of the geometry of the system (in this case the diameter of the cylinder electrode) and D_j is the diffusion coefficient of the chemical species j. A similar relation was obtained by Berger and Hau [83] for turbulent flow in straight pipes:

$$Sh = 0.0165 v_L Re^{0.86} Sc^{0.33} \tag{2.31}$$

Scale

The formation of a corrosion scale on the steel surface decreases the corrosion rate via two independent mechanisms: (I) the reduction of the steel surface area available for the anodic and cathodic reactions and (II) the internal geometry of the scale decreases the diffusion coefficient of the species flowing through it. [26]

The reduction in steel surface area can be addressed by assuming that the surface covered by the scale completely blocks corrosion from occurring underneath it. Then, the reduced current density ($i_{\text{corr,s}}$) can be obtained by multiplying the current density by the fraction of the surface not covered by the corrosion scale (θ_s):

$$i_{\text{corr,s}} = (1 - \theta_s) i_{\text{corr}} \tag{2.32}$$

where i_{corr} represents the corrosion current density without corrosion scale, θ_s is the fraction of the steel surface covered by the corrosion scale and $i_{\text{corr,s}}$ is the area-adjusted current density.

Within the scale the concentration of chemical species follows the reaction-diffusion equation:

$$\frac{\partial c}{\partial t} = \nabla \cdot J + R(c) \tag{2.33}$$

where c is the concentration of the species, J is the total flux and the function R accounts for all the chemical reactions.

Eq. (2.33) can be approximated by assuming a quasi-steady state ($\frac{\partial c}{\partial t} \approx 0$) for the duration of a small time interval. After integration, the following relation can be obtain:

$$J_z = J_m - \int_{z_m}^{z} R\, dz \tag{2.34}$$

where J_m is the integration constant which is equal to the flux at the metal-scale interface which can be obtained using Eq. (2.21). The integral term in Equation (2.34) can be discretised as

$$J_{n_z} = J_m - \sum_{n=n_m}^{n_z} R_n \Delta z \tag{2.35}$$

where n represents a coordinate in the discrete z axis normal to the electrode surface and Δz is the length of one discrete unit.

Negligible fluid flow—and thus convective transport—is assumed within the scale (although this might not hold true at the edge of the scale for very porous scales). Therefore, the total flux inside the scale can be described by Fick's first law of diffusion:

$$J = -D_{\text{eff}} \nabla c \tag{2.36}$$

Here, the effective diffusion (D_{eff}) is used instead of the diffusion coefficient in water (D) to account for the decreased diffusion inside the porous scale diffusion of species. The effective diffusion can be defined in terms of the diffusion coefficient as:[84]

$$D_{\text{eff}} = \frac{D\varepsilon_t\delta}{\tau} \tag{2.37}$$

ε_t is the effective transport-through porosity which accounts not only for the loss of cross-section area but also for those pores that are isolated and cannot be accessed by the solution. Assuming that there are no trapped pores, we can use the general porosity of the scale (ε). δ is the constrictivity and it has a value of 1 unless the molecule is of the same order of magnitude than the pores. Since the pores inside the scale are much larger than the individual chemical species, δ=1. τ is the tortuosity which is related to the geometry of the pores and how they are interconnected. It is not trivial to model τ especially for anisotropic systems where τ is related to the geometry of an ideal 1-dimensional capillaric model and not a 3-dimensional network.[85] To overcome this problem many empirical equations have been proposed in the literature which define the $\frac{\varepsilon}{\tau}$ ratio as a function of the porosity.[86] One of the most widely used models approximates the ε/τ ratio as a power of the porosity:[84]

$$\frac{\varepsilon}{\tau} \approx \varepsilon^m \Rightarrow D_{\text{eff}} \approx D\varepsilon^m \tag{2.38}$$

where parameter (m) is usually determined by fitting to observed transport rates. While a material can have a range of different values, the vast majority of diffusion experiments in the literature report values in the 1.5-2 range for different materials.[84,86] Previous sweet corrosion 1-dimensional models have used the value m=1.5 proposed by Newman for porous electrodes, also called the Bruggeman relation, and this is the value adopted in the current model.[42,87–89]

The absence of flow inside the scale and the difference in the effective diffusion coefficients (D_{eff}) inside and outside the scale implies that one cannot use the mass transfer coefficient associated with the flow conditions outside the scale ($k_{\text{mt,flow}}$). Kahyarian et al.[36] proposed to combine the mass transfer coefficients of the flow ($k_{\text{mt,flow}}$) and scale ($k_{\text{mt,scale}}$) into a *composite* mass transfer coefficient ($k_{\text{mt,comp}}$) via the following relation:

$$\frac{1}{k_{\text{mt,comp}}} = \frac{1}{k_{\text{mt,scale}}} + \frac{1}{k_{\text{mt,flow}}} \tag{2.39}$$

The sum of mass transport coefficient reciprocals implies that the *composite* mass transport coefficient is dominated by the smallest mass transport coefficient. In other words, the mass transport from the bulk to the steel surface is dictated by either the mass transport from the bulk of the solution to the scale-electrolyte interface or the diffusion of species across the scale, whichever is the slowest.

Firstly, we describe how porosity affects the concentration gradient for a system with constant flux. If the porosity of the scale is assumed to be uniform across the scale the difference between the edges of the scale is calculated using Fick's first law of diffusion and Eq. (2.38):

$$c_{se} - c_m = -\frac{JL_s}{D\varepsilon^m} \tag{2.40}$$

where L_s is the thickness of the scale, c_{se} is the concentration at the scale-electrolyte interface and c_m is the concentration at the steel-scale interface. This model constitutes a significant approximation to the real internal structure of the corrosion scale as the topology of the scale is reduced to the average porosity which is then used to estimate the tortuosity to approximate the effective diffusion coefficient. In the current work this approximation is partially improved by considering the change in average porosity in discrete intervals along

the direction normal to the surface (z):

$$c_{se} - c_m = -\frac{J\Delta z}{D} \sum_{n=n_m}^{n_{se}} \frac{1}{\varepsilon_n^m} \tag{2.41}$$

where Δz is the length of a discrete unit of space n represents a coordinate in the z direction in units of Δz, n_m and n_s represent the coordinates at the steel-scale interface and scale-electrolyte interface respectively.

Combining Eqs. (2.40) and (2.41) an *equivalent* porosity (ε_{eq}) can be defined for a scale with non-uniform porosity:

$$\frac{1}{\varepsilon_{\text{eq}}^m} = \frac{l}{L_s} \sum_{n=n_m}^{n_s} \frac{1}{\varepsilon^m(z)} = \frac{1}{n_{se} - n_m + 1} \sum_{n=n_m}^{n_s} \frac{1}{\varepsilon^m(z)} \tag{2.42}$$

The equivalent porosity is a useful metric to summarise the overall porosity of the scale as it corresponds to the uniform porosity that a scale of the same thickness would need to have to obtain the same concentration difference between both sides of the scale assuming a constant flux. Indeed, even if the flux is not constant across the scale this metric can provide a good indication of the overall porosity of the scale.

Due to the $FeCO_3$ precipitation reaction the Fe^{2+} flux at the steel surface does not remain constant throughout the scale as described by Eq. (2.35).

The homogeneous reactions of the carbonate equilibria reach thermodynamic equilibrium relatively quickly when compared to the diffusion of the respective chemical species so the chemical species involved in these reactions are considered to be in thermodynamic equilibrium throughout the scale. On the other hand, the concentration of Fe^{2+} is subject to the slow $FeCO_3$

precipitation reaction. Therefore, for $J_{\mathrm{Fe}^{2+}}$ the $R_{\mathrm{Fe}^{2+}}$ in Eq. (2.35) is simply the precipitation reaction rate as defined in Eq. (2.22) divided by the length of the scale ($R = R_{\mathrm{FeCO_3}}/L_s$) so that R is in $\mathrm{mol\,s^{-1}\,m^{-3}}$. The flux at the scale-electrolyte interface ($J_{se,\mathrm{Fe}^{2+}}$) can then be obtained from Eq. (2.35).

$$J_{se,\mathrm{Fe}^{2+}} = J_{m,\mathrm{Fe}^{2+}} - \sum_{n=n_m}^{n_{se}} \frac{R_{n,\mathrm{FeCO_3}}}{L_s}\Delta z = J_{m,\mathrm{Fe}^{2+}} - R_{\mathrm{FeCO_3}}(\overline{SS}_{\mathrm{FeCO_3}}) \tag{2.43}$$

where $R_{\mathrm{FeCO_3}}(n_z)$ is the precipitation rate calculated using the $SS_{\mathrm{FeCO_3}}$ at n_z and $\overline{SS}_{\mathrm{FeCO_3}}$ is the mean $SS_{\mathrm{FeCO_3}}$ inside the scale. Then, the Fe^{2+} concentration at the scale-electrolyte interface ($c_{se,\mathrm{Fe}^{2+}}$) can be calculated using Eq. (2.8) and Eq. (2.7):

$$c_{se,\mathrm{Fe}^{2+}} = \frac{J_{se,\mathrm{Fe}^{2+}}}{k_{\mathrm{mt,flow},\mathrm{Fe}^{2+}}} + c_{b,\mathrm{Fe}^{2+}} \tag{2.44}$$

The Fe^{2+} concentration at the discrete coordinate inside the scale that is closest to the scale-electrolyte interface ($c_{n_{se}-1,\mathrm{Fe}^{2+}}$) can be obtained using the following relation:

$$c_{n_{se}-1,\mathrm{Fe}^{2+}} = \frac{\Delta z J_{n_{se},\mathrm{Fe}^{2+}}}{D_{\mathrm{Fe}^{2+}}\varepsilon^m_{n_{se}}} + c_{n_{se},\mathrm{Fe}^{2+}} \tag{2.45}$$

More generally, the Fe^{2+} concentration at each discrete node in the scale is calculated by sequentially solving the following equation:

$$c_{n_{se}-i,\mathrm{Fe}^{2+}} = \frac{\Delta z J_{n_{se}-i+1,\mathrm{Fe}^{2+}}}{D_{\mathrm{Fe}^{2+}}\varepsilon^m_{n_s-i+1}} + c_{n_s-i+1,\mathrm{Fe}^{2+}} \tag{2.46}$$

Starting at the scale-electrolyte interface (n_{se}) where the concentration is known from Eq. (2.44) the concentration at the steel-scale interface can be obtained by repeatedly applying Eq. (2.46). However, in order to calculate $c_{n_{se}-1,\mathrm{Fe}^{2+}}$ (Eq. (2.44)) the $J_{se,\mathrm{Fe}^{2+}}$ is needed which depends on the mean supersaturation inside the scale (Eq. (2.43)) and can only be calculated from the

Fe^{2+} concentrations inside the scale (Eq. (2.46)). Therefore, Eqs. (2.43) and (2.46) must be solved iteratively using the self-consistent method.

The model described up to this point is 1-dimensional. However, the simulation takes place in a 3-dimensional space. In order to accommodate the 1-dimensional model into the 3-dimensional space the concentrations of all species and the porosity of the scale are averaged over the xy-plane parallel to the steel surface for each n_z.

In the 3-dimensional model, both the steel-scale interface and the scale-electrolyte interface (now defined as θ_m and θ_{se} respectively) are obtained by taking the average over all (x, y) coordinates of the lowest and highest z coordinate respectively:

$$\theta_m = \frac{1}{N_x N_y} \sum_{n_x=1}^{N_x} \sum_{n_y=1}^{N_y} \min n_{z,s}(n_x, n_y) \tag{2.47}$$

$$\theta_{se} = \frac{1}{N_x N_y} \sum_{n_x=1}^{N_x} \sum_{n_y=1}^{N_y} \max n_{z,s}(n_x, n_y) \tag{2.48}$$

where N_x and N_y are the number of discrete units in the x and y directions and $n_{z,s}(n_x, n_y)$ represents the subset of discrete volume units at (n_x, n_y) that are part of the scale. As an example, Fig. 2.3 displays a 3-dimensional cell where n_{metal} and n_s positions are indicated in its cross sectional representation.

Therefore, the limits of the scale and, hence, its thickness are pseudo-continuous, i.e. they increase in increments of $\frac{\Delta z}{N_x N_y}$. To account for the pseudo-continuous scale limits a weight function can be introduced to correct the weight that porosity at the extremes has on the diffusion of species. This correction ensures that the diffusion coefficients vary smoothly as

the scale grows.

$$c_{n_{se}-i,\mathrm{Fe}^{2+}} = \frac{w_{n_{se}-i+1}\Delta z J_{n_{se}-i+1,\mathrm{Fe}^{2+}}}{D_{\mathrm{Fe}^{2+}}\varepsilon^{m}_{n_s-i+1}} + c_{n_s-i+1,\mathrm{Fe}^{2+}} \tag{2.49}$$

with

$$w_{n_z}\begin{cases}\theta_m & \text{if } n_z = n_m \\ \theta_{se} & \text{if } n_z = n_{se} \\ 1 & \text{otherwise}\end{cases} \tag{2.50}$$

where θ_{se} and θ_m are the fraction of Δz occupied by the scale at the extremes. Therefore, by definition the scale thickness is:

$$T_{scale} = (\theta_m + (n_{se} - n_m - 1) + \theta_{se})\Delta z \tag{2.51}$$

The total precipitation rate is therefore calculated as a weighted average of the precipitation rate at each n_z of the scale

$$R_{\mathrm{FeCO_3}}(\overline{SS}_{\mathrm{FeCO_3}}) = \frac{\sum_{n_z=n_m}^{n_{se}} w_{n_z} R_{\mathrm{FeCO_3},n_z}}{\sum_{n_z=n_m}^{n_{se}} w_{n_z}} \tag{2.52}$$

Δz is an important parameter of the model. It constraints both the internal and external structure of the scale to a minimum length. The changes in the structure of the scale can result in scales with different protective properties and thus different corrosion rates. Therefore, it is important to select an adequate value for Δz. The CO_2 corrosion scales are mostly made of siderite crystallites of sizes of a few micrometres. These crystallites constraint the structure of the scale in a similar way. Therefore it is appropriate to set the value of Δz to a representative size of these crystallites. While siderite crystallite dimensions may change during the formation of the corrosion scale generally the smallest crystallites are around 5 µm in size[54,90]. Therefore, the Δz chosen for the current CO_2 corrosion model is 5 µm.

2.2.5 Stochastic 3-dimensional model

Despite the recent advancements in general CO_2 corrosion models their inability to describe the stochastic nature of the corrosion and scale formation phenomena limits their predictive power.[47,48] The present model addresses this limitation by extending the 1-dimensional CO_2 corrosion model described in Sections 2.2.1 to 2.2.4 into a 3-dimensional discrete space and introducing a stochastic method to drive the corrosion and scale formation process at the micro-scale.

The stochastic method adopted in the present model is inspired by cellular automaton models which have been used to model general stochastic phenomena successfully.[47,91] Time and space are discretised in the order of seconds and micrometers respectively and the simulation takes place in a 3-dimensional cell which is periodic in the x and y directions which correspond to the steel surface plane. Each discrete unit of volume (voxel) can have one of 3 different states: metal (M), corrosion product (S) or electrolyte (E). The cell is initialised with two layers of steel (M) and two layers of electrolyte (E) above the steel layers. The cell dynamically grows in the z direction to accommodate for the corroding steel surface and the corrosion scale growth

In the present model, steel surface corrosion and corrosion product precipitation take place in discrete voxel units, the smallest unit of volume in the simulation cell. The length of a voxel is a parameter of the model. Since the model must reproduce the micro-scale features of a CO_2 corrosion scale the length of a voxel is set to the size of the $FeCO_3$ crystallites that make up the scale which are on the order of a few µm. Figure 2.3 shows a 3D representation of the simulation cell as well as a vertical cross section of the cell.

Once the corrosion current density (i_{corr}) is calculated for time t^n using Eq. (2.21) the total volume of steel dissolved due to corrosion (V_{corr}) during time-step $\Delta t^n = t^{n+1} - t^n$ (where Δt^n changes throughout the simulation as explained below) can be obtained using the following conversion factor:

$$V^n_{\text{corr}} = (1 - \theta_{scale}) i^n_{corr} \frac{M(\text{Fe})}{2F\rho_{\text{steel}}} \Delta t^n \tag{2.53}$$

where $M(\text{Fe})$ is the molecular weight of Fe, F is the Faraday constant and ρ_{steel} is the density of the steel. Then, the number of steel voxels that "dissolve" in this time-step (turn into electrolyte voxels) can be calculated as:

$$N_{ME} = \frac{V_{\text{corr}}}{V_{\text{voxel}}} \tag{2.54}$$

where N_{ME} is the number of steel voxels that have to turn into electrolyte voxels. N_{ME} is rounded to the nearest integer as voxels are indivisible units of volume in this model. The residual decimal part of N_{ME} is then stored and added to the N_{ME} of the next time interval. The N_{ME} steel voxels that will change their state to electrolyte are selected from the subset of steel voxels that have at least one electrolyte neighbour, i.e. they form at least one steel-electrolyte interface with any of their six neighbouring voxels. Valid corrosion sites are marked with a "C" in Fig. 2.3. These voxels are sampled from a uniform probability distribution of all the existing steel-electrolyte interfaces in the simulation cell. Hence, steel voxels with more steel-electrolyte interfaces, i.e. more surface area exposed to the electrolyte, have a higher probability of developing corrosion and dissolving into the electrolyte. This probability distribution is updated after each change of state to remove the previous selected voxel from the distribution.

Similarly, the total volume of corrosion product precipitated can be obtained from the

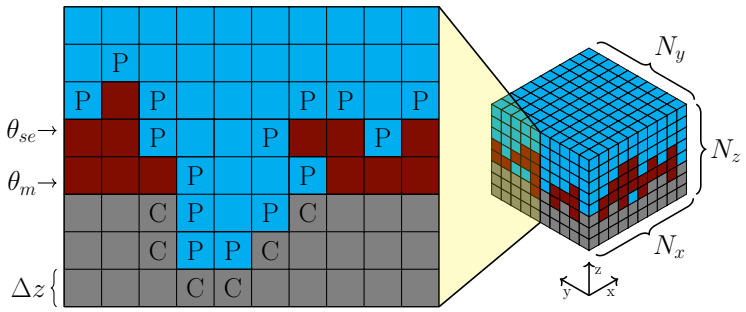


Figure 2.3: Cross section of the 3-dimensional simulation cell. Square represents on of the three phases: steel (gray), scale (dark red) and water (cyan). Steel squares marked with a C are candidates to be dissolved in the next iteration cycle. Water squares marked with a P are sites where precipitation may take place in the next iteration cycle.

total precipitation rate (R_{tot}) calculated using Eq. (2.52).

$$V^n_{\text{precip}} = R^n_{\text{tot}} \frac{M(\text{FeCO}_3)}{\rho_{\text{siderite}}} \Delta t^n \tag{2.55}$$

where $M(\text{FeCO}_3)$ is the molecular weight of FeCO_3 and ρ_{FeCO3} is the density of FeCO3. Then, the number of electrolyte voxels to "precipitate" (turn into scale voxels) can be calculated as:

$$N_{ES} = \frac{V_{\text{precip}}}{V_{\text{voxel}}} \tag{2.56}$$

where N_{ES} is the number of electrolyte voxels that have to turn into scale voxels. As with N_{ME}, N_{ES} is rounded to the nearest integer and the residual decimal part of N_{ES} is then stored and added to the N_{ES} of the next time interval.

Corrosion product precipitation can only take place in electrolyte voxels with neighbouring steel or scale voxels, i.e. precipitation is only allowed on top of either steel or scale surface. Indeed, homogeneous precipitation is ignored in the current model as most of the precipitation occurs directly on the metal or scale surface where the SS_{FeCO_3} is the highest.[92] Furthermore, precipitation is considered equally as likely to occur on the steel surface than on the scale

surface. Valid precipitation sites are those marked with a "P" in Fig. 2.3.

The N_{ES} electrolyte voxels to change their state to scale are sampled from a probability distribution of all electrolyte-metal and electrolyte-scale interfaces weighted by their corresponding local $SS_{\mathrm{FeCO_3}}$, i.e. the $SS_{\mathrm{FeCO_3}}$ calculated at the xy plane of the corresponding interface. Consequently, electrolyte voxels at high $SS_{\mathrm{FeCO_3}}$ will have a higher likelihood of undergoing precipitation compared to those at low $SS_{\mathrm{FeCO_3}}$. As with the probability distribution of N_{ME}, this probability distribution is also updated after each change of state to remove the previous selected voxel from the distribution.

The corrosion and precipitation processes result in physical changes to the surface of the steel and the corrosion scale and concentration changes in the solution which in turn determine the precipitation and corrosion rates of the next time interval. Therefore, it is important to select a time-step that is short enough so that both the precipitation and corrosion rates change gradually but long enough that simulations take a reasonable amount of time to complete. This is achieved by using a dynamic time-step that is adjusted at every step to only change the state of less than $N_x N_y \times 1\%$ of voxels per time interval.

Since the probability distributions for both corrosion and precipitation change after a voxel's change of state these changes form a Markov chain and consequently the order in which corrosion and precipitation are changing states within a time interval is important. For example, if in a given time interval all corrosion changes of state are carried out first followed by all precipitation changes of state it would be equivalent to a high corrosion rate followed by a high precipitation rate. While this issue is partly mitigated by the small dynamic time-step described above, additionally, the N_{ME} and N_{ES} changes of state are processed in small batches of n_{ME} and n_{ES} where the $n_{ME} : n_{ES}$ ratio within each batch is as close as possible to the $N_{ME} : N_{ES}$ ratio.

With this stochastic method the corrosion and scale formation will still follow general CO_2 corrosion trends but now each simulation run will result in a different outcome due to the non-deterministic nature of the model. The next section investigates the associated variance of these stochastic simulations.

2.3 Algorithm

All the electrochemical, chemical and transport equations used by the SLCA model have been described in Sections 2.2.1 to 2.2.5. This section explains the general steps that the algorithm follows during a simulation run.

2.3.1 Initialisation

1. Initialise the 3-dimensional cell with a flat steel surface. That is two xy layers of electrolyte (E) on top of two xy layers of steel (M).
2. Initialise the mass transport coefficients using either Eq. (2.29) or Eq. (2.31).
3. Initialise bulk concentrations.
4. Initialise electrochemical constants for the cathodic and anodic reactions.
5. Initialise corrosion and precipitation rates.

2.3.2 Solution chemistry

The model assumes that the solution remains locally electroneutral. Therefore, one can calculate the H^+ concentration from Eq. (2.1) using the Newton-Raphson method provided the Fe^{2+} concentration is known. Then, HCO_3^- and CO_3^- can be calculated using the corresponding thermodynamic equilibrium equation from the carbonate equilibria (Table B.2).

The model also incorporates a Pitzer model (Appendix B.2) that calculates the activity coefficients of the chemical species which are used in the carbonate equilibria thermodynamic equations (Table B.2) to calculate the activities of the chemical species. However, the Pitzer model requires the concentration of the species to calculate their respective activity coefficients. Therefore, the solution chemistry must be solved by calculating the concentrations and activity coefficients iteratively until a self-consistent result is reached given a convergence criteria. In this case, the convergence criteria is reached when the H^+ concentration is known with a precision of 10^{-14} times its value. The H^+ concentration is chosen as the convergence criteria because all other concentrations are derived from it.

2.3.3 Corrosion and precipitation rates calculation

The corrosion rate can be calculated by solving Eq. (2.20) using the Newton-Raphson method. The precipitation rate depends on the mean SS_{FeCO_3} inside the scale which is calculated from all the local SS_{FeCO_3} across the scale. The local SS_{FeCO_3} depends on the local Fe^{2+} and CO_3^{2-} concentrations which are obtained from the Fe^{2+} flux inside the scale (Eq. (2.46)) and Eq. (2.1) and Table B.2 respectively. The Fe^{2+} flux inside the scale depends on the precipitation rate at each point of the scale Eq. (2.35) which is a function of the local

$SS_{\mathrm{FeCO_3}}$. Therefore, the local and global precipitation rate must be solved iteratively until a self-consistent result is reached. The bisection method is used to find a global precipitation rate that is consistent with the mean of all local precipitation rates. The lower and upper limits of the bisection algorithm are set to $[0, F_{\mathrm{corr}} + F_{\mathrm{lim,Fe^{2+}}}]$ where F_{corr} is the Fe^{2+} flux due to corrosion and $F_{\mathrm{lim,Fe^{2+}}}$ is the maximum mass transport current from the bulk of the solution to the scale-electrolyte interface. The calculation is considered converged when the global precipitation rate is known with a precision of 10^{-14} times its value.

2.3.4 Iteration cycle

After the initialisation of the model, the simulation goes through a series of iteration cycles that evolve the corrosion system until the time limit is reached. Each iteration cycle contains the following steps:

1. Select a time-step (in µs) where N_{ME} and N_{ES} are less than 1% of $N_x \times N_y$.
2. Calculate N_{ME} and N_{ES} (Eqs. (2.54) and (2.56)).
3. Apply the N_{ME} and N_{ES} changes of state in batches that keep the $N_{ME} : N_{ES}$ ratio.
4. Update the bulk Fe^{2+} concentration.
5. Update the bulk concentrations of all species.
6. Update mass transport coefficients $k_{\mathrm{mt,comp}}$.
7. Update corrosion rate.
8. Update precipitation rate.

2.4 Model variance

The stochastic method used in the model plays a key role in describing both the dissolution of steel due to corrosion and the precipitation of corrosion product on the steel surface. However, this results in a non-deterministic simulation. Therefore, it is instructive to investigate the variance of the metrics calculated by the model at different points in time. Figures 2.4 and 2.5 displays the standard deviation of the corrosion rate, precipitation rate, surface coverage and equivalent porosity of 50 simulations at pH 5 and pH 6, a A/V of $1\,\mathrm{m}^{-1}$, 80 °C, 1% NaCl with a RCE of 2 cm of diameter rotating a X-65 steel sample at 1000 rpm. The simulation cell was configured with a square cell width of 200 voxels. The corrosion rate standard deviation increases rapidly during the initial stages of the simulation, it plateaus during the corrosion scale growth stage and drops once the scale has formed. The standard deviation at pH 5 has a similar shape to that at pH 6 but it rises and drops later due to the slower film formation. The standard deviation of the precipitation rate increases as the film grows until the precipitation rate reaches its peak and the standard deviation remains constant for the rest of the simulation. A similar trend can be observed for the surface coverage and equivalent porosity.

These results not only showcase the expected standard deviation of the model but, crucially, they provide qualitative insights on the inherent volatility of the corrosion and scale formation process. Both the corrosion and precipitation rate exhibit close to an order of magnitude difference in standard deviation between the start of the simulation and the partial formation of the corrosion film. Indeed, the CO_2 corrosion system appears to be most volatile during the scale formation stages, in particular when the precipitation rate reaches its maximum. Furthermore, this volatility in the corrosion and precipitation rate is carried over to the physical properties of the corrosion scale such as the coverage and equivalent porosity shown

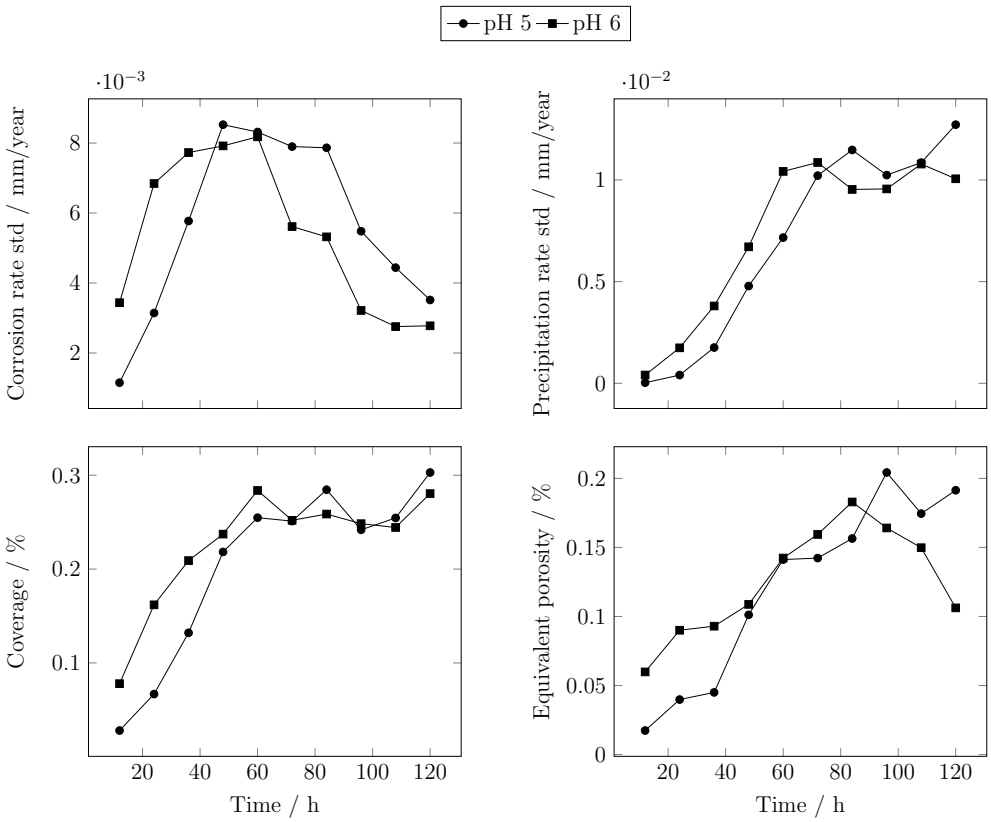


Figure 2.4: Standard Deviation of the corrosion rate, precipitation rate, surface coverage and equivalent porosity at pH 5 and pH 6. Simulation conditions: 80 °C, 1 bar, 1% NaCl, 1 m^{-1} A/V and 1000 rpm RCE.

in Fig. 2.4. While the standard deviation of these metrics constitute only a small fraction of their respective mean value these small macroscopic variations can arise from significant local changes. These variations originating from the stochastic nature of the model are observed in phenomena such as localised corrosion, a type of corrosion that only affects a small area of the surface but can result in critical damage to the material.[93–100]

The size of the simulation cell is investigated in Figs. 2.6 and 2.7 where the mean and standard deviation for the corrosion rate, precipitation rate, steel surface coverage and equivalent porosity are displayed for three sets of 50 120h simulations with cell widths of 20, 40 and 60 voxels. The simulations were initialised with the same conditions used in Figs. 2.6

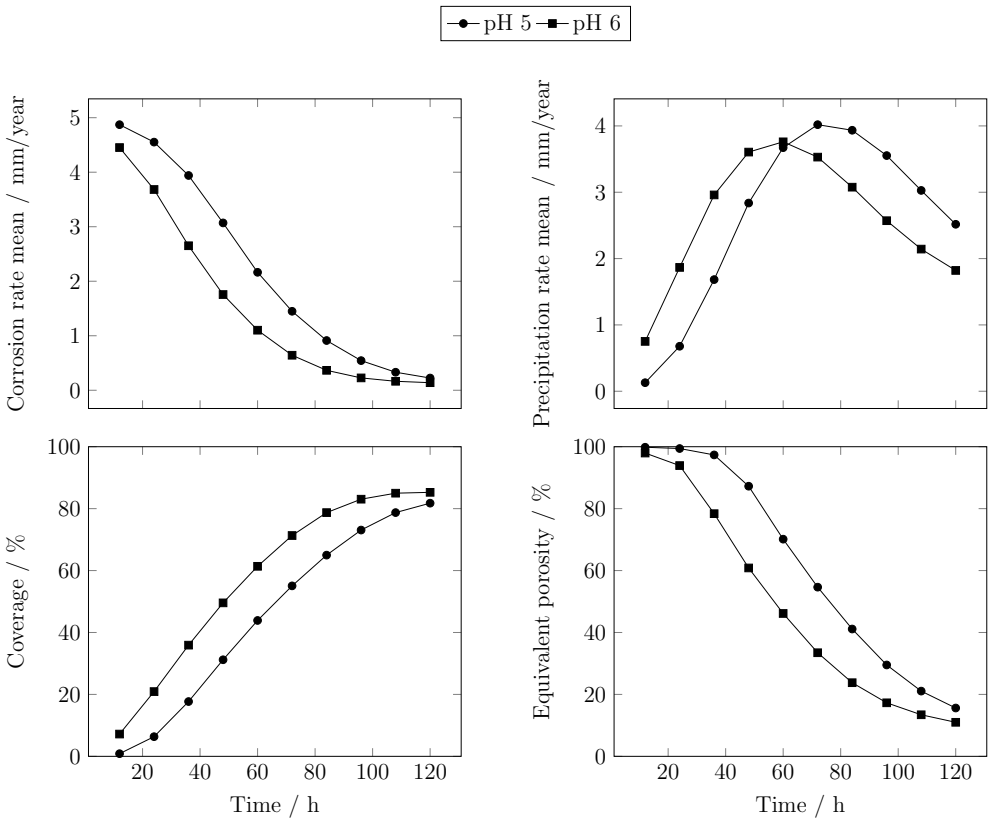


Figure 2.5: Mean corrosion rate, precipitation rate, surface coverage and equivalent porosity at pH 5 and pH 6. Simulation conditions: 80 °C, 1 bar, 1% NaCl, 1 m^{-1} A/V and 1000 rpm RCE.

and 2.7 at pH 6. The mean is not significantly different between any of the three cell widths for the four metrics displayed in Fig. 2.6. However, the standard deviation (Fig. 2.7) increases for lower cell widths. Moreover, the set of simulations with a cell of 20 voxels wide displays considerably higher standard deviation compared to cell widths of 40 and 60 voxels suggesting that the standard deviation converges for a high enough cell width value. The convergence of both the standard deviation and the mean is explored in Fig. 2.8 where the corrosion rate standard deviation and the mean corrosion rate is plotted against the number of voxels in the xy cross section of the simulation cell ($N_y \times N_x$). At 40,000 voxels—a square cell width of 200 voxels—both the standard deviation and the mean have converged to a stable value. Therefore, from here onwards all simulations will be run with a simulation cell 200 voxels

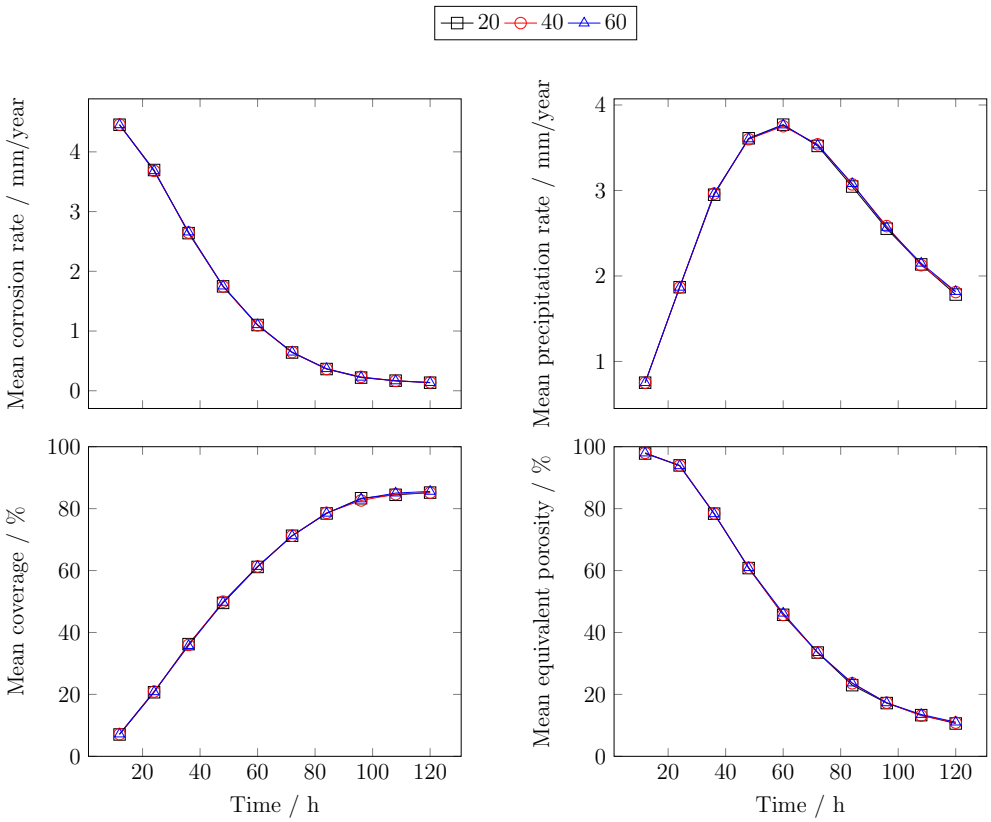


Figure 2.6: Mean corrosion rate, precipitation rate, surface coverage and equivalent porosity for a square cell width of 20, 40 and 60 voxels. Simulation conditions: 80 °C, pH 6, 1 bar, 1% NaCl, 1 m^{-1} A/V and 1000 rpm RCE.

wide unless otherwise specified.

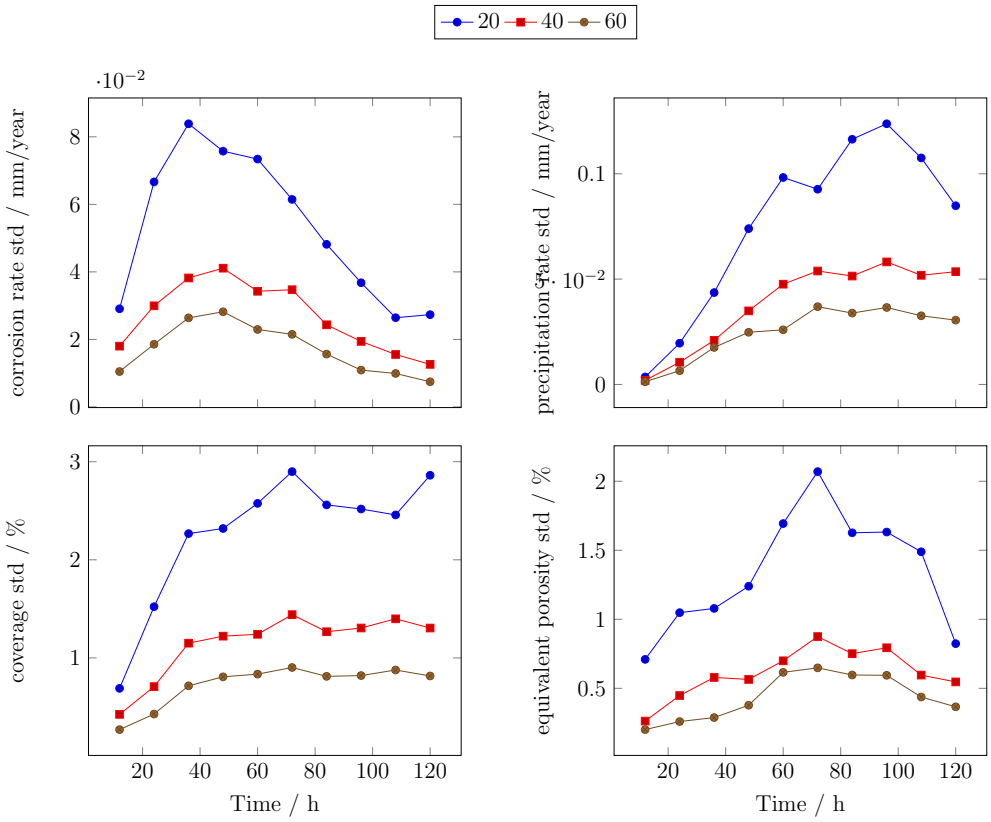


Figure 2.7: Standard Deviation of the corrosion rate, precipitation rate, surface coverage and equivalent porosity for a square cell width of 20, 40 and 60 voxels. Simulation conditions: 80 °C, pH 6, 1 bar, 1% NaCl, 1 m^{-1} A/V and 1000 rpm RCE.

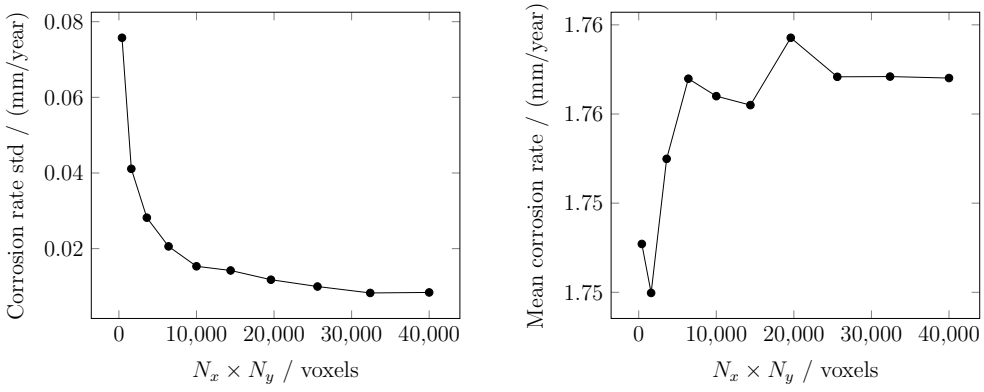


Figure 2.8: Standard Deviation and mean of the corrosion rate as a function of the number of voxels in the xy plane. Simulation conditions: 80 °C, pH 6, 1 bar, 1% NaCl, 1 m^{-1} A/V and 1000 rpm, 2 cm RCE.

2.5 Conclusions

The present work introduces the Semi-local Corrosion Approximation (SLCA), a hybrid corrosion model that combines a general CO_2 corrosion model with elements of Cellular Automata models to incorporate the heterogeneous and stochastic component that current general corrosion models are lacking. The general corrosion model includes a water chemistry model, an electrochemical model, a corrosion product precipitation model and a mass transport model.

The water chemistry model incorporates the carbonate equilibria thermodynamic equations and a charge balance equation. The activity coefficients are calculated using a Pitzer model.

The electrochemical model describes the anodic iron oxidation reaction and the cathodic HER reaction. The cathodic limiting current density (i_{lim}) includes the H^+ mass transport limiting current density ($i_{\text{lim,mt}}$) and the CO_2 hydration reaction limiting current ($i_{r,\text{lim}}$) which controls the so-called buffering effect. The corrosion current density and corrosion potential is obtained by assuming that the total current density is zero, i.e. there is no charge build-up in the electrochemical system.

The corrosion product precipitation model is adapted from the well established corrosion layer accumulation rate (CLAR) model first introduced by Sun and Nešic[71] and using the $FeCO_3$ solubility product equation first developed by Sun et al.[73]. Additionally, a dissolution model for $FeCO_3$ was developed to account for scale dissolution in those environments where SS_{FeCO_3} drops below 1.

The mass transport model introduces defines the mass transport coefficients for different

flow geometries. Additionally, a simplified diffusion model is used to describe the combined mass transport and corrosion product precipitation inside the scale. The effective diffusion coefficient inside the scale is approximated by the porosity of the scale which is discretised to account for a non-uniform porosity across the scale. Lastly, a series of equations are derived to obtain the concentration profile of Fe_2^+ from the bulk of the solution to the steel surface allowing to compute the average supersaturation inside the scale.

The 1-dimensional corrosion model was then adapted to a 3-dimensional system by averaging some key metrics in the xy-plane such as the porosity and the limits of the scale.

A 3-dimensional stochastic model was developed to reproduce the intrinsic randomness of the local corrosion and precipitation processes. Similar to cellular automaton models, the time and space is discretised and discrete volume units (voxels) can have one of three different states: metal (M), corrosion product (S) or electrolyte (E). Then, corrosion events are defined as the transition from a metal state to an electrolyte state whereas precipitation events are defined as the transition from an electrolyte state to a corrosion product state. Once the volume of steel to dissolve and corrosion product to precipitate are calculated from the corrosion and precipitation rates, the stochastic model selects the voxels that will corrode and precipitate in the current time interval from all possible candidates by sampling from a probability distribution given by basic rules. For corrosion only metal voxels exposed to electrolyte voxels are able to corrode and the more exposure to electrolyte voxels the higher the probability of getting picked. For precipitation, any electrolyte voxel with a neighbouring metal or scale voxel can be selected for precipitation. As with the corrosion probability distribution, more metal and scale neighbours results in a higher probability but, in addition, each voxel is weighted by its local SS_{FeCO_3} so that higher supersaturation results in higher chance of precipitation.

Finally, the variance associated to the stochastic model was studied as a function of time. The analysis revealed that the variance of the corrosion and precipitation rate as well as scale properties such as the scale surface coverage and the equivalent porosity generally increases during the formation of the corrosion scale and either decrease or remain stable once the scale is fully formed. In addition, the optimum xy cell dimensions found to be 200×200 voxels.

This novel modelling technique is developed with the goal of understanding the heterogeneous and stochastic interaction between the metal surface and the corrosion scale that occur naturally during the corrosion process. To the author's knowledge no CO_2 corrosion model is able to describe this process explicitly. Furthermore, the simplicity of the 3-dimensional stochastic model allows additional use cases to be incorporated with ease as demonstrated in Section 5.3 where a simple inhibitor model is incorporated to the SLCA model.

Next chapter will focus on the validation of the model and the predictions obtained by the model for different corrosion environments.

Chapter 3

CO_2 corrosion time-series analysis

3.1 Introduction

The measurement of the corrosion rate in steel substrates is a challenging task with many factors at play. Small variations in the preparation, composition, surface chemistry and roughness of the samples can lead to corrosion rates that are difficult to reproduce, especially between different research groups. Most of these variations can be mitigated to a certain extend but can never be completely eliminated. This is an important issue for the development of corrosion models as the data from corrosion experiments is used to fit these models and, consequently, the accuracy of a model can only be as good as the accuracy of the measurements.

Corrosion rates are typically calculated by either the linear polarization resistance (LPR) or the weight gain/loss (WGL) methods.[101] The LPR method is an electrochemical technique that measures the polarization resistance which is inversely proportional to the current

density. The WGL method consists on scraping the corrosion product off the sample after the experiments and compare the weight of the sample to its original weight. Using LPR one can take continuous measurements of the same sample, however the current density can only be obtained through calibration against the electrochemical system under study. On the other hand, one can obtain the mass lost due to corrosion using the WGL method, however this is a destructive measurement so multiple samples are needed to take measurements over time.

Since mass transport in the oil and gas pipelines is driven by turbulent flow it is important to reproduce similar flow conditions in corrosion experiments to obtain results that are representative of the corrosion systems found in the field. However, such experiments require a more complex setup and, consequently, are less common compared to experiments carried out under stagnant conditions.

Despite the these challenges, carefully designed measurements can still elucidate the trends and patterns arising from these complex electrochemical systems. This chapter validates the SLCA model against experimental data and explores how the conditions of the environment affect the development of the corrosion process and the formation of the corrosion scale.

3.2 Validation of the model

The model presented in this work is aimed at predicting CO_2 corrosion of the ubiquitous X-65 steel under scaling conditions and turbulent flow. However, time-series measurements of experiments under these conditions are scarce. The work carried out by Tanupabrungsun [1] in 2013 is one of the very few studies that measure the corrosion of X-65 steel under turbulent flow and scaling conditions. In his study the corrosion rate of X-65 steel substrates was

measured for different flow velocities (100, 500 and 1000 rpm) at high temperature (120 °C). Although most of the electrochemical and thermodynamic equations and constants used in this model were not validated at such high temperatures we nevertheless attempt to use this study as a reference as is currently the only available data available. Therefore, to facilitate the comparison between the experimental and theoretical results the current density was scaled to match the experimental corrosion rate at 100 rpm. Thus the prediction being validated is the subsequent trend in the corrosion rate and properties of the scale. However, it is also worth noting that the relative initial corrosion rate between the three systems is similar to the one predicted by the model.

Figure 3.1 shows the measured and predicted corrosion rate. The initial corrosion rate follows the same trend in both the experiment and the model predictions for the three velocities. Higher initial corrosion rates are observed at lower flow velocities where lower mass transfer is offset by the lower pH at the surface due to the larger concentration gradient. The model predicts a higher initial surface SS_{FeCO_3} at 100 rpm compared to 500 and 1000 rpm (Fig. 3.1). This translates into an immediate $FeCO_3$ precipitation on the steel surface at 100 rpm Fig. 3.2, and consequently a rapid reduction in the rate of corrosion. The experimental measurements also show a rapid decrease in corrosion rate in all flow conditions tested but it is fastest at 100 rpm suggesting that at the conditions of the experiment the precipitation rate, and hence the surface $FeCO_3$ supersaturation, is higher at low flow velocities in agreement with the model predictions. At higher flow velocities the $FeCO_3$ supersaturation, and hence the precipitation rate, is lower, thus, the corrosion rate decreases at a lower rate.

Analysing the model one can see that the rapid precipitation of corrosion product at low flow velocities lowers the corrosion rate by (I) covering active corroding sites on the steel surface and by (II) acting as a mass transport barrier for the electrochemical species. The

predicted cross section of the corrosion scale formed after 20 hours of simulation can be observed in Fig. 3.3. The surface coverage can be calculated as the fraction of the steel surface covered by the corrosion scale. The cross section graphics show partially covered steel surfaces for 1000, 500 and 100 rpm with a surface coverage of 29%, 38% and 48% and average scale thickness of 26, 36 and 45 µm respectively. The additional scale coverage and thickness that develops at low flow velocities provides a better protection against corrosion which is predicted to result in lower long term corrosion rates in agreement with the experimental measurements. The final corrosion rates predicted by the model are considerably different from the ones observed experimentally. This is attributed to an underestimation of the precipitation rate at high temperatures by the precipitation model. Indeed, the $FeCO_3$ precipitation kinetics model used in Eq. (2.22) was only fitted for temperatures up to 80 °C and it is likely that this leads to the underestimate of the precipitation at higher temperatures.[72]

The current model extends beyond the prediction capabilities of current CO_2 corrosion models by providing a in-depth analysis of the generalised structure of the corroding surface as a function of time. Thanks to the explicit simulation of the steel surface 3D structure other important metrics can also be extracted from the model as time series data such as the local porosity, surface coverage, scale thickness, surface roughness, pit size distribution, pit density distribution, and concentration profile of chemical species. This new data brings a novel perspective on the evolution of the CO_2 corrosion process and improves our understanding of the metal dissolution and film growth dynamics. This is explored further below.

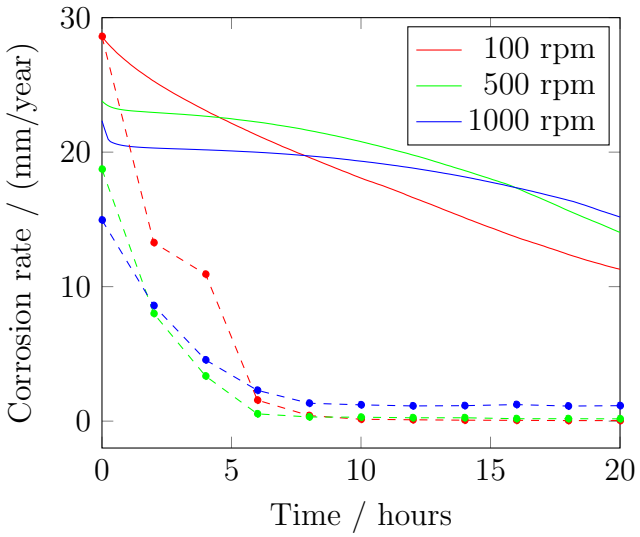


Figure 3.1: Comparison between the corrosion rates from the experimental results from Tanupabrungsun[1] (dashed line) and the model predictions (solid line) under the same conditions.

3.3 Predictions of scale growth

Having validated the general predictions of the model for the time evolution of growth rates it is interesting to see the insights it provides about the growth of the 3D scale structure under different conditions.

The purpose of the model developed herein is to improve our understanding of the corrosion and scale formation process under different environments. In this section the predictions of the model for conditions in which four key parameters—initial pH, area/volume ratio (A/V), temperature and pressure—are modified will be discussed and compared to the current general understanding of CO_2 corrosion. These parameters have been chosen for their relevance in the oil and gas industry and for their significant impact in the corrosion process. The simulations run under turbulent flow conditions simulating the mass transfer of a RCE of 2 cm diameter rotating at 1000 rpm with a sample of X-65 steel.

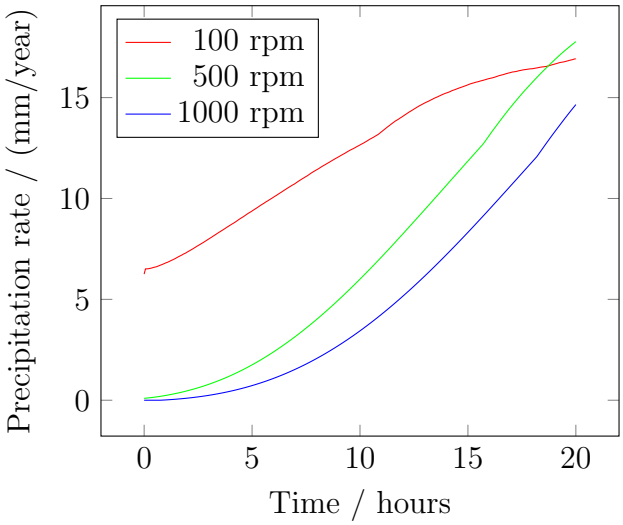


Figure 3.2: Predicted precipitation rates for 100, 500 and 1000. Simulation conditions: 120 °C, pH 4, 5.2 bar, 1% NaCl and 0.63 m^{-1} A/V and a 2 cm diameter RCE.

3.3.1 pH dependence

The pH of the water phase is of great importance to the industry because it is one of the few parameters that can be controlled to a certain degree using different pH stabilisation techniques.[102] These techniques typically aim to reduce the acidity of the water phase to promote the formation of corrosion product films, thereby reducing the corrosion rate. Indeed, the solution pH has proven to be a determining factor in the formation and growth of the corrosion scale.[54,103,104] To understand the effect of pH on the film formation three corrosion systems were simulated for 5 days with initial pH values 5.4, 6 and 6.6, an A/V of 1 m^{-1}, 80 °C and 1% NaCl.

At the start of the simulation the precipitation rate at pH 6.6 is the highest of the three whereas for pH 5.4 and 6 is close to zero since the concentration of CO_3^{2-} is not as high. During the initial stages of the simulation where a film hasn't fully formed the precipitation rate will increase steadily for all three initial bulk acidities as the Fe^{2+} concentration increases

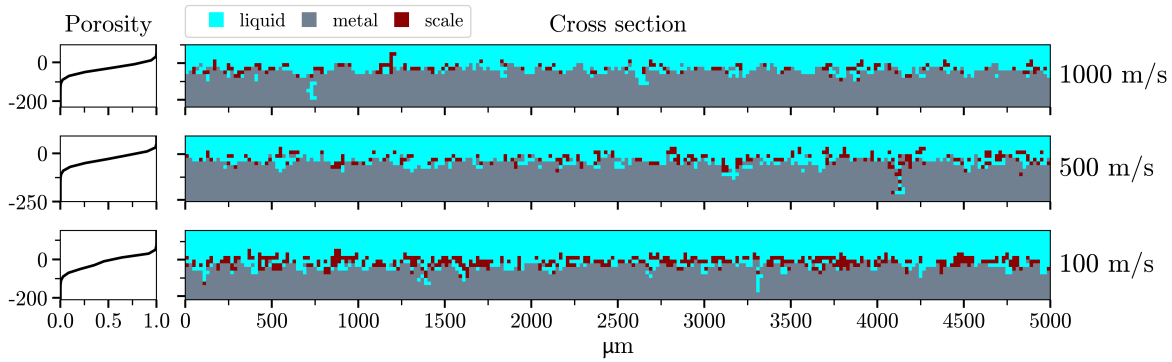


Figure 3.3: Cross-sections and porosity profiles of the 3-dimensional simulation cells after 20 hours of simulation for 100, 500 and 1000 $\mathrm{m\,s^{-1}}$. Simulation conditions: 120 °C, pH 4, 5.2 bar, 1% NaCl and 0.63 $\mathrm{m^{-1}}$ A/V

due to the corrosion reaction. Additionally, the $[CO_3^{2-}]$ increases as the solution shifts to higher pH as a result of the corrosion reaction which further contributes to the precipitation rate increase (Fig. 3.4).

As the steel surface is covered by the corrosion product the corrosion rate and its respective diffusion gradient decrease steadily (Fig. 3.4). Consequently, the difference between species concentrations at the bulk and at the steel surface shrink, and hence so does the SS_{FeCO_3} which causes the precipitation rate to drop. For the three pH values tested the precipitation rate peaks at about 4 mm/year; however, the peak is reached considerably sooner at pH 6.6 since the higher $[CO_3^{2-}]$ results in higher SS_{FeCO_3} for the same Fe^{2+} concentration.

After 40 hours of simulation the corrosion rate at pH 6.6 stabilises and subsequently increases slightly for the rest of the simulation as a dynamic equilibrium is achieved between continuing corrosion and precipitation. At pH 5.4 and 6 the precipitation rate is still decreasing after 120 hours and at this point the corrosion becomes lower than that computed for pH 6.6. We examine this interesting cross-over below.

Figure 3.5 shows the different computed physical properties of the scale such as its coverage

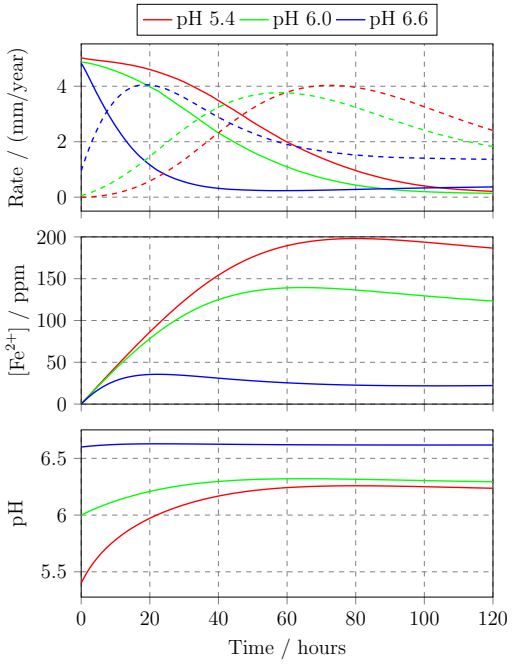


Figure 3.4: Model predictions of corrosion rate (solid line), precipitation rate (dashed line), bulk $[Fe^{2+}]$ and bulk pH for pH 5.4, 6 and 6.6. Simulation conditions: 80 °C, 1 bar, 1% NaCl and 1 m^{-1} A/V.

over the steel surface, equivalent porosity, weight, and average thickness. The total mass of the pH 6.6 scale cross over the masses of the other two scales as the precipitation rate drops at 120 hours. This result has recently been reproduced experimentally at similar pH values.[54]

The emerging physical properties illuminate the growth process. The scale forms significantly quicker at pH 6.6. After 40 hours of simulation the scale is considerably thicker and less porous than at pH 5.4 and 6 while also covering a larger area of the steel surface (Fig. 3.5). However, by the end of the simulation the scales formed at pH 5.4 and 6 exhibit a larger coverage of the steel surface, a similar porosity and greater thickness. This suggests that when the scale is rapidly formed it may not cover the entirety of the steel surface. Indeed, at pH 6.6 the scale reaches a maximum coverage of 84% leaving some small areas of the steel surface exposed to corrosion. These small areas can then develop localised corrosion and compromise the structural integrity of the steel. Figure 3.6 shows the cross-section of the 3-dimensional

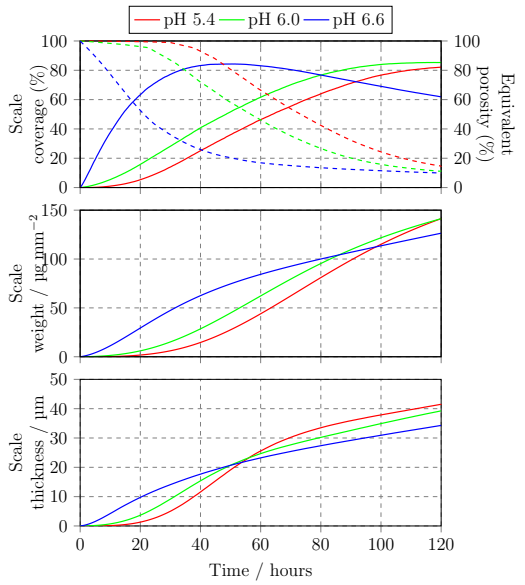


Figure 3.5: Model predictions of surface coverage (solid line), equivalent porosity (dashed line), scale weight and scale thickness for pH 5.4, 6 and 6.6. Simulation conditions: 80 °C, 1 bar, 1% NaCl and 1 m^{-1} A/V.

simulation cells after 120 hours where the panels on the left side display the fraction of void volume (porosity). While all three scales exhibit a similar density at the centre of the scale, the interface between the steel surface and the scale is significantly more porous at pH 6.6. Moreover, the 2-dimensional cross-section shows fairly localised porous sites rather than a uniformly distributed porosity across the interface hinting that localised corrosion is taking place. This result is in good agreement with reports of localised corrosion observed after the formation of a protective scale at high pH.[53,105] At both pH 5.4 and 6 the model predicts that rather similar, dense scales form with a lower porosity at the steel-scale interface which provides a better corrosion protection after 120 hours compared to pH 6.6 as indicated by the crossover in corrosion rates at that point.

Overall, these findings highlight the importance of incorporating a 3-dimensional component to corrosion modelling and the difficulty in defining and identifying a *protective* corrosion scale. Several studies reported increased corrosion protection at high pH.[54,70] However, these

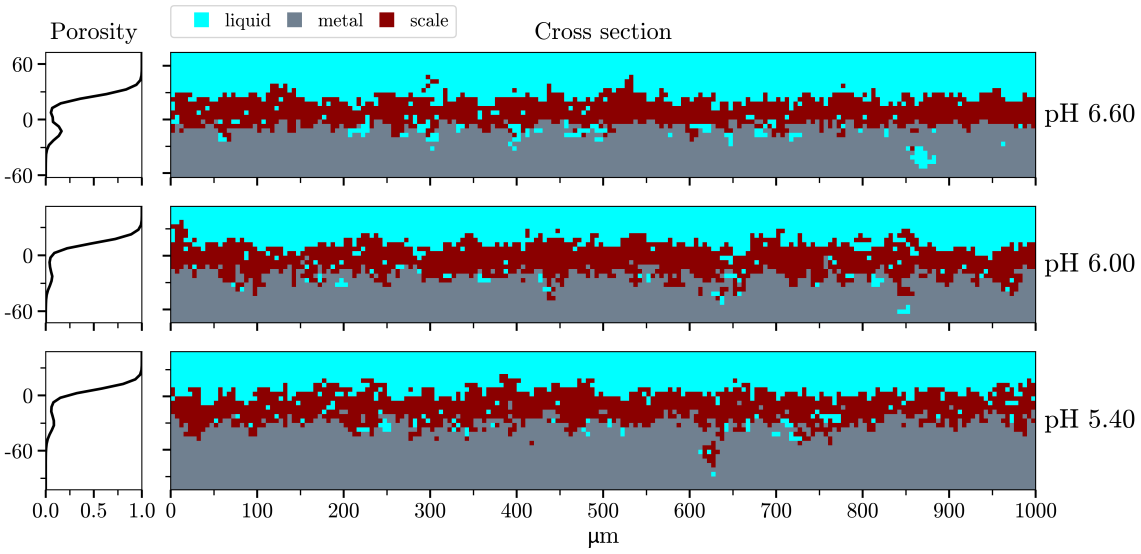


Figure 3.6: Cross-sections and porosity profiles of the 3-dimensional simulation cells after 120 hours of simulation for pH 5.4, 6 and 6.6. Simulation conditions: 80 °C, 1 bar, 1% NaCl, $1\,\mathrm{m}^{-1}$ A/V.

experiments typically run for no longer than a few days which the current model suggests may not be enough time to assess the long term protectiveness of a scale. The results presented in this section demonstrate that the long protectiveness of the scale cannot always be derived from the total corrosion product deposited on the steel surface. Instead, the formation process of the scale has to be taken into account in order to determine the stability of a fully formed corrosion scale. This includes analysing the evolution of key metrics such as the scale coverage and the porosity of the scale. The CO_2 corrosion model presented in this work is able to predict these properties by explicitly modelling the corrosion scale in the 3-dimensional space, a key feature that current CO_2 corrosion models are lacking. Furthermore, thanks to the 3D description of the scale the model allow us to observe how localised corrosion appears underneath rapidly formed corrosion scales. This level of insight is key to describe corrosion scale and their protective properties.

3.3.2 A/V dependence

The total macroscopic metal surface area and the volume of electrolyte are also key parameters that affect the corrosion process and the formation of the film. In a pipeline flow the surface area is proportional to the radius of the pipe and the volume is proportional to the radius squared, hence the A/V ratio is inversely proportional to the radius of the pipe. The effective surface area in contact with the water and the volume of water also depend on the proportion of water in the oil/gas/water multiphase system flowing through the pipe. The higher the A/V ratio the faster the electrolyte will reach $FeCO_3$ supersaturation leading to more precipitation in a shorter period of time. Figure 3.7 illustrates the results of the model for a 5-day simulation of three systems with 0.1, 1 and 10 m^{-1} A/V, pH 5.8, 80 °C and 1% NaCl.

For the same amount of iron dissolved into solution the system with an A/V of 10 m^{-1} increases the Fe^{2+} concentration 10 and 100 times faster than for 1 and 0.1 m^{-1} (Fig. 3.7). This results in a rapid buildup of SS_{FeCO_3} causing a sudden increase in precipitation rate for the first 8 hours followed by an equally rapid decline as the corrosion scale forms and protects the steel surface from further corrosion and hence limiting the source of Fe^{2+} and reducing the SS_{FeCO_3}. At 1 m^{-1} the buildup of $[Fe^{2+}]$ is slower which results in a gradual change in precipitation rate over the course of the simulation. At 0.1 m^{-1} the increase in Fe^{2+} concentration is even slower as there is more electrolyte per unit area. In this case there is minimal precipitation on the metal surface and a scale is never formed. Consequently, the corrosion rate stays constant throughout the simulation.

The scales formed at 10 and 1 m^{-1} are significantly different (Fig. 3.8). The scale formed at 10 m^{-1} is considerably thinner and more compact as the steel surface underneath the scale didn't corrode significantly due to the rapid formation of the scale and therefore is rather

flat. On the other hand, the scale formed at $1\,\mathrm{m}^{-1}$ is thicker and since the steel surface has corroded for considerably longer the resulting scale exhibits a rather irregular interface between the steel and the scale which is also slightly more porous than the $10\,\mathrm{m}^{-1}$ scale as indicated by the porosity panel on the left side of the figure. Finally, the simulation performed at $0.1\,\mathrm{m}^{-1}$ left a completely eroded steel surface due to the continuous corrosion throughout the simulation as no scale was able to form under this conditions.

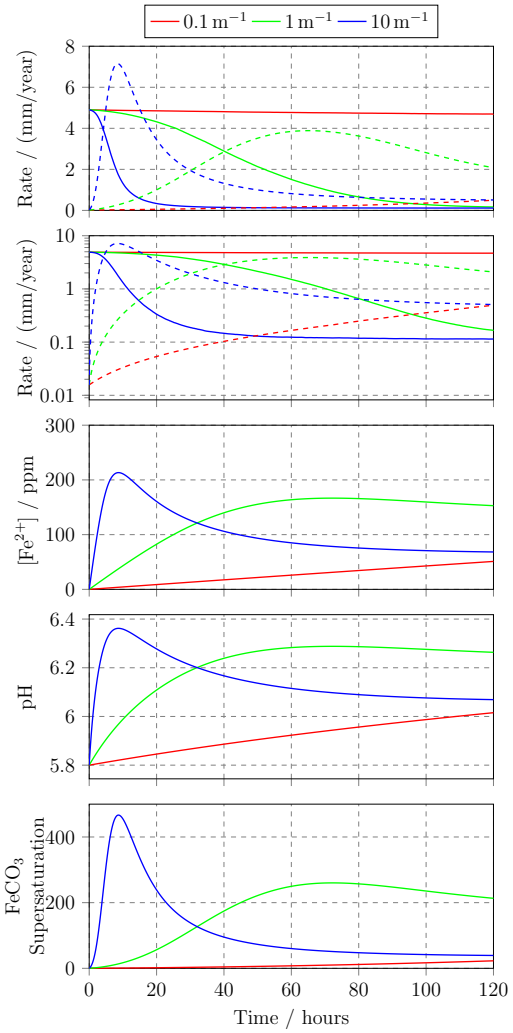


Figure 3.7: Model predictions of corrosion rate (solid line), precipitation rate (dashed line), bulk $[Fe^{2+}]$, bulk pH and bulk supersaturation for A/V ratios of 0.1, 1 and $10\,\mathrm{m}^{-1}$. Simulation conditions: 80 °C, 1 bar, pH 5.8, 1% NaCl.

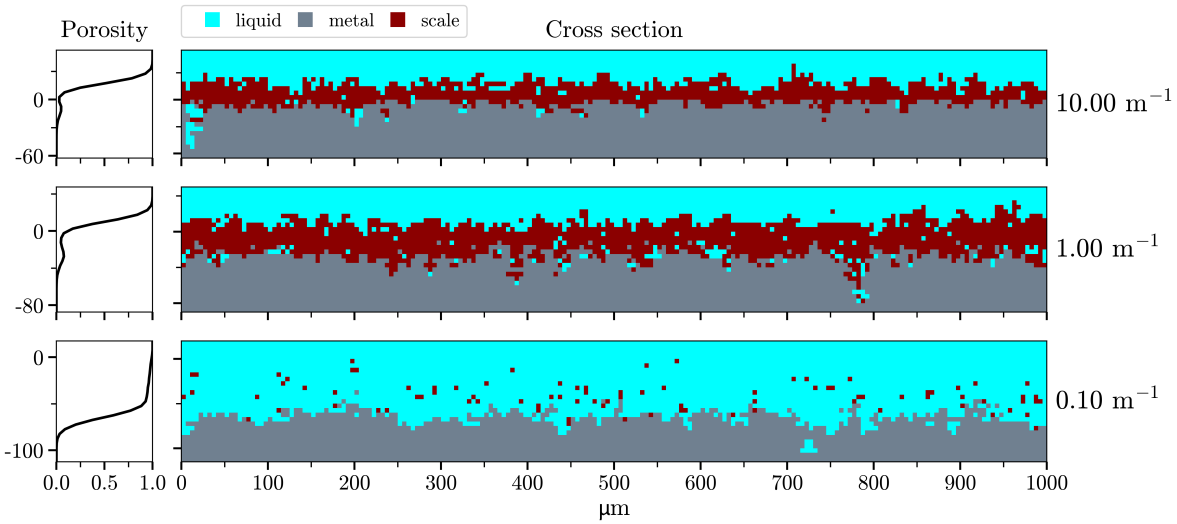


Figure 3.8: Cross-sections and porosity profiles of the 3-dimensional simulation cells for A/V ratios of 0.1, 1 and 10 m^{-1} after 120 hours. Simulation conditions: 80 °C, 1 bar, pH 5.8, 1% NaCl.

3.3.3 Temperature dependence

Temperature is a key factor in electrochemical systems. Higher temperatures enhance the kinetics of chemical and electrochemical reactions and facilitates the diffusion of species in solution. In the context of CO_2 corrosion temperature accelerates both the corrosion reaction and the precipitation reaction.[54,106] Since $FeCO_3$ precipitation is a considerably slower reaction the enhanced kinetics at higher temperatures have a significant impact in the precipitation rate. The $FeCO_3$ solubility also decreases at high temperatures hence increasing the SS_{FeCO_3}.[73,74,107] Therefore, the increase in precipitation has previously been hypothesised to compensates for the enhanced corrosion kinetics. To better understand the effect of temperature on the corrosion and scale growth three corrosion systems at 60, 70 and 80 °C were simulated for 5 days with an A/V of 1 m^{-1}, pH 6 and 1% NaCl.

The simulated initial corrosion rate increases with temperature as reported in the literature (Figure 3.9).[54,106] At the initial conditions there's not enough surface SS_{FeCO_3} for $FeCO_3$ to

precipitate immediately. Instead, as the surface SS_{FeCO_3} increases so does the precipitation rate. Following the same trend as the corrosion rate the precipitation rate increases faster at high temperatures. This is explained by the combined effect of (I) a higher supersaturation due to the higher corrosion rate at high temperatures and (II) enhanced precipitation reaction kinetics at high temperatures. At 80 °C the higher precipitation rate results in the rapid formation of a corrosion scale. Despite starting at a higher corrosion rate this scale decreases the corrosion rate below those formed at 60 and 70 °C in less than 40 hours and by the end of the simulation the scale manages to block the majority of the corrosion on the steel surface. At 60 and 70 °C the simulations follow a similar trend but the formation of the scale is slower, especially at 60 °C. Interestingly, by the end of the simulation the corrosion rate at 70 °C is similar to that at 80 °C despite the slower formation of the scale.

Figure 3.10 displays the cross-section of the 3-dimensional simulation cells for 60, 70 and 80 °C after 120 hours. The scale formed at 80 °C appears to be the only fully formed scale of the three. At 70 °C the scale is of similar thickness to the one at 80 °C but is more porous despite having a similar level of protection in terms of corrosion rate. In contrast, the scale formed at 60 °C is still in the early stages of growth and it's significantly more porous than the other two.

According to the predictions obtained from the model higher temperatures accelerate the growth of the corrosion scale which result in the rapid decrease of the corrosion rate even at the expense of higher initial corrosion rates. Therefore, the model supports the general consensus that more protective scales are formed at higher temperatures and quickly offset the initial higher corrosion rates.

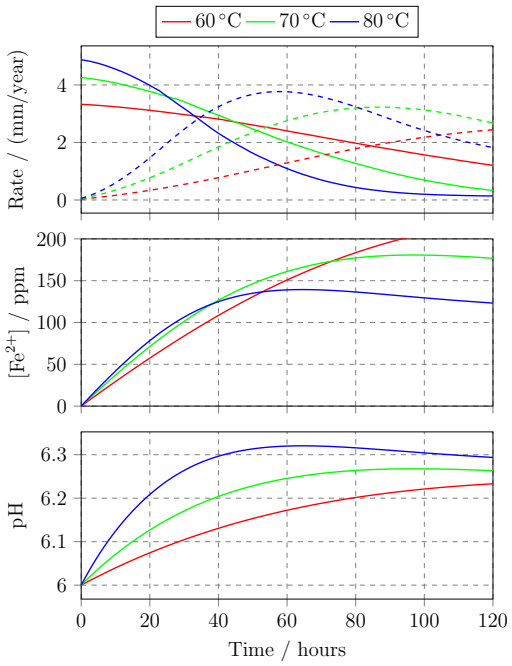


Figure 3.9: Model predictions of corrosion rate (solid line), precipitation rate (dashed line), bulk $[Fe^{2+}]$ and bulk pH at 60, 70 and 80 °C. Simulation conditions: 1 bar, pH 6, 1% NaCl and 1 m^{-1} A/V.

3.3.4 Pressure dependence

The total pressure determines the CO_2 partial pressure and, hence, the total number of carbonate species in solution. An increase in total pressure increases the concentration of carbonic acid which enhances the *buffering* effect contribution to the HER and, consequently, it increases the corrosion rate. Similarly, an increase in total pressure also increases the carbonate concentration which results in an increase in SS_{FeCO_3} and a higher precipitation rate. Since the total pressure affects both the corrosion and the precipitation it is difficult to provide general trends about the formation of the scale and its protectiveness without explicitly simulating the system with predictive corrosion models like the one presented herein. In this section the effect of the total pressure is investigated by simulating three corrosion systems at 1, 2 and 3 bar of total pressure for 5 days. The corrosion systems are initialised

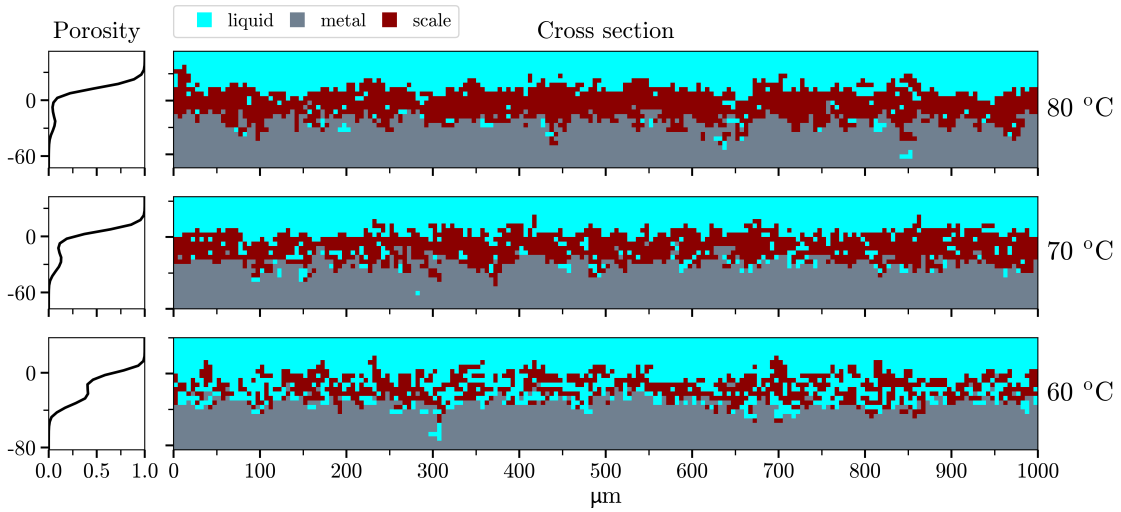


Figure 3.10: Cross-sections and porosity profiles of the 3-dimensional simulation cells at 60, 70 and 80 °C after 120 hours of simulation. Simulation conditions: 1 bar, pH 6, 1% NaCl and 1 m^{-1} A/V.

with the following conditions: 80 °C, an A/V of 0.1 m^{-1}, pH 6 and 1% NaCl.

Figure 3.11 displays the predicted corrosion rate, precipitation rate, Fe^{2+} bulk concentration, SS_{FeCO_3} and scale surface coverage as a function of simulation time. Both the initial corrosion rate and precipitation rate are predicted to increase at higher total pressures due to the aforementioned increase in H_2CO_3 and CO_3^{2-} concentrations. As the corrosion process dissolves iron into solution the SS_{FeCO_3} increases which accelerates the precipitation of corrosion product. As the corrosion product covers the surface of the steel and creates a diffusion barrier for electroactive species the corrosion rate decreases steadily. When the corrosion and precipitation process generate and consume (respectively) the same amount of Fe^{2+} the supersaturation stops increasing. From that point on, high pressure environments may exhibit a significantly higher precipitation rate compared to the corrosion rate creating a net consumption of Fe^{2+} ions inside the scale which results in a lower supersaturation compared to the bulk. Therefore, the precipitation rate drops while the bulk SS_{FeCO_3} remains stable. This is particularly noticeable at 2 and 3 bar due to the high precipitation rate and

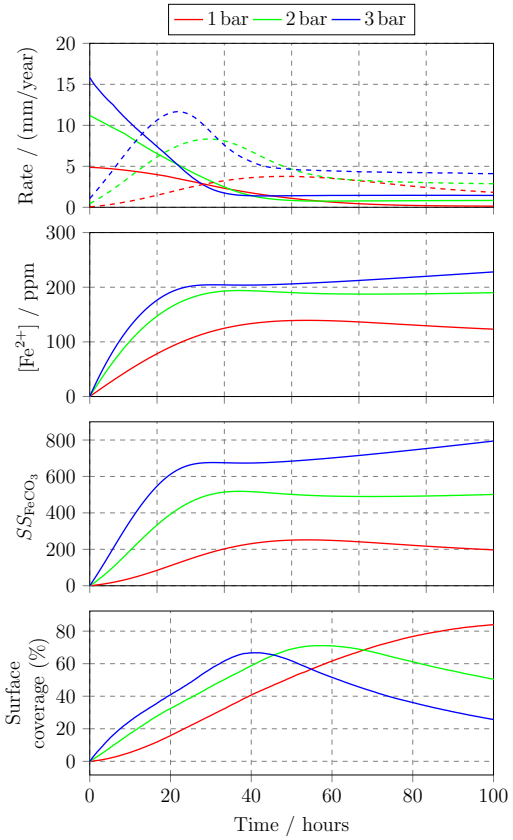


Figure 3.11: Model predictions of corrosion rate (solid line), precipitation rate (dashed line), bulk $[Fe^{2+}]$ at 1, 2 and 3 bar. Simulation conditions: 80 °C, pH 6, 1% NaCl and 0.1 m^{-1} A/V.

it leads to a rapid decrease of the scale surface coverage soon after the precipitation rate drops as corrosion undermines the scale. On the other hand, at 1 bar the precipitation rate is considerably lower during the initial stages of the simulation resulting in a sustainable growth of the corrosion scale which achieved an 80% coverage of the corrosion surface.

Figure 3.12 displays a cross section of the 3-dimensional simulation cell after 5 days for the three simulated environments. At 1 bar the corrosion scale is thinner compared to the thicker scale developed at 2 and 3 bar and the steel-scale interface is significantly less porous providing a stronger adhesion to the steel. In contrast, the scales developed at higher pressures (2 and 3 bar) are thicker due to the higher precipitation rate but the corrosion has undermined the scale to the point where the scale is at risk of detaching from the steel surface.

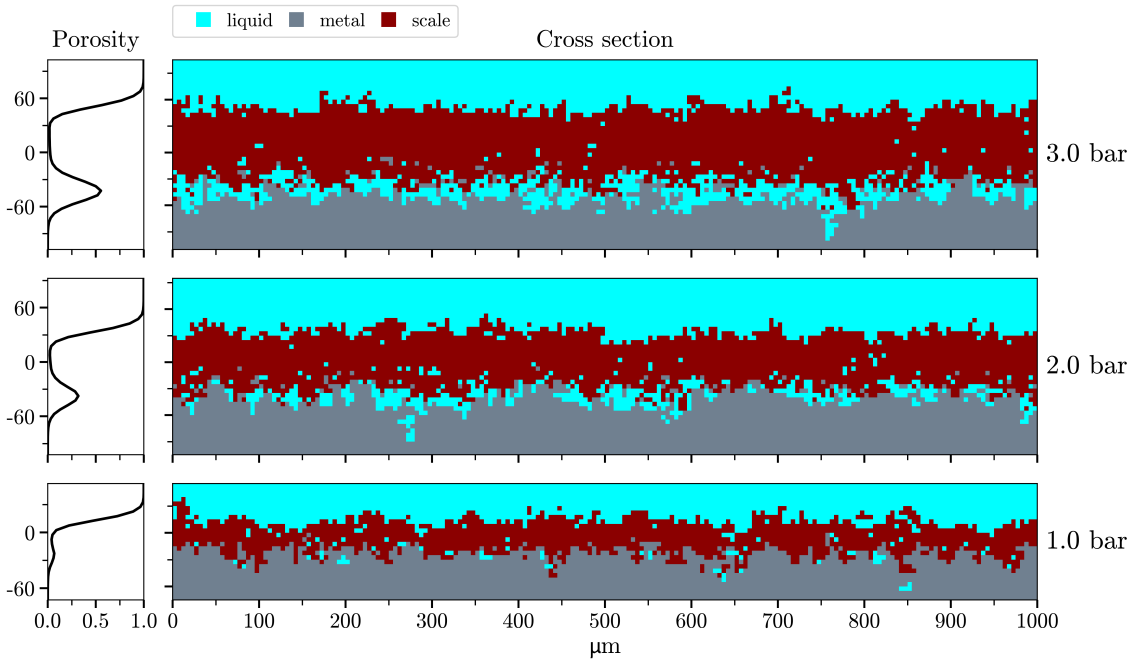


Figure 3.12: Cross-sections and porosity profiles of the 3-dimensional simulation cells after 120 hours of simulation at 1, 2 and 3 bar. Simulation conditions: 80 °C, pH 6, 1% NaCl and 0.1 m^{-1} A/V.

3.4 Conclusions

This chapter focused on the validation of the model described in Chapter 2 and the analysis of the model predictions. Four key parameters in CO_2 corrosion—initial pH, A/V ratio, temperature and total pressure—were analysed due to their relevance in the oil and gas industry.

The model was validated against a high temperature, turbulent flow experiment where X-65 steel samples were corroded at 100, 500 and 1000 rpm. The model was able to reproduce the corrosion rate trends of the experimental data adequately and its predictions are consistent with the current understanding of the corrosion process. However, the absolute values could not be reproduced reliably likely due to the precipitation rate model not being validated at

such high temperatures.

When comparing the same corrosion system at different pH values the model predicts a thinner and denser film at high pH while porous thicker films are obtained at low pH, a result consistent with the current literature. Furthermore, the model was able to explain this phenomena in terms of the growth characteristics of the corrosion film for each pH tested.

The simulations at different A/V ratios emphasized the importance of the macroscopic geometry of the system during the scale growth phase and suggests that fast precipitation might not always be desirable to form a protective film.

The model demonstrated how temperature influences both the corrosion and precipitation reaction by simulating the same corrosion system at 60, 70 and 80 °C. The temperature effect on the corrosion rate is predicted to only be significant during the initial stages of corrosion whereas the impact of temperature on the precipitation rate is considerably greater and longer-lasting. Therefore, corrosion at different temperature exhibit a similar steel dissolution but a faster film formation at high temperatures.

Lastly, three simulations were carried out at 1, 2 and 3 bar to investigate the effect of the total pressure of the system on the corrosion and scale formation. It was found that at high pressures the initial corrosion rate is higher due to the increased H_2CO_3 concentration. Moreover, due to the fast corrosion product precipitation at high pressures the corrosion rate decreases rapidly to the point where it is so low compared to the precipitation rate that more Fe^{2+} is consumed by the precipitation reaction than produced by the corrosion reaction. This leads to an interesting scenario where the SS_{FeCO_3} inside the scale is lower than the SS_{FeCO_3} at the bulk of the solution which drives the precipitation rate down.

The analysis of these parameters in isolation illustrates the value the present model. Each parameter affects the steel dissolution and scale formation process differently and thanks to the additional structural data provided by the present model we are able to decompose each effect independently and obtain a detailed history of the microscopic events that led to the final structure of the steel and the corrosion scale. This new level of detail in the description of the corrosion process is key to understand the relationship between the 3D structure and growth characteristics of the corrosion scale and the degree of protection it offers against corrosion.

Chapter 4

CO_2 corrosion multiparameter analysis

4.1 Introduction

In experimental investigations it is important to isolate the variable under study by controlling or fixing all other variables so that the effect can be directly correlated with the isolated variable. In CO_2 corrosion experiments this methodology, while necessary, is often complex and time consuming resulting in very few data points to draw conclusions from. Furthermore, in complex systems with multiple parameters such as CO_2 corrosion environments it is important to understand the interactions between parameters which requires a prohibitive number of data points for experimental work.

CO_2 corrosion models not only provide forecasting capabilities but also allow us to carry out a comprehensive exploratory analysis of the parameter space which would otherwise be unfeasible experimentally. This is important when generalising trends observed in the data as

the validity of these trends is constraint to the set of conditions tested. Therefore, the ability of models to test a wide range of different conditions in a reasonable amount of time is key to draw accurate conclusions from the data.

The temperature, pressure and pH are known to have a profound effect in the development of CO_2 corrosion.[14,43] This chapter explores the relationships amongst these three parameters by running 336 simulations with different combinations of environment parameters and analysing 4 important metrics in CO_2corrosion: the corrosion rate, the surface coverage, the porosity and the total volume of steel lost. The results will shed some light on the complex relationships between the investigated parameters and help to establish general CO_2 corrosion trends valid for a wide range of the parameter space.

4.2 Multiparameter analysis

This section investigates the corrosion rate, the corrrosion scale surface coverage, the equivalent porosity and the amount of steel lost at the end of a 2-day simulation. A set of 336 simulations of a X-65 steel sample where carried out for the following parameter ranges: 60 °C to 90 °C, 1 bar to 6 bar and pH 5 to pH 6.4. All simulations are initialised with the following parameters: 1% NaCl, 1 m^{-1} A/V and a 2 cm diameter RCE at 1000 rpm. The data is analysed in the following figures in a series of *heatmaps* that display two variables simultaneously. Each figure consists of a 3×3 matrix where each row contains heatmaps with a different pair of the parameters under study (temperature, pressure and pH) and each of the columns within a row represent a different value of the third parameter. This comprehensive visual inspection of the data facilitates the identification of trends and patterns across the parameter space.

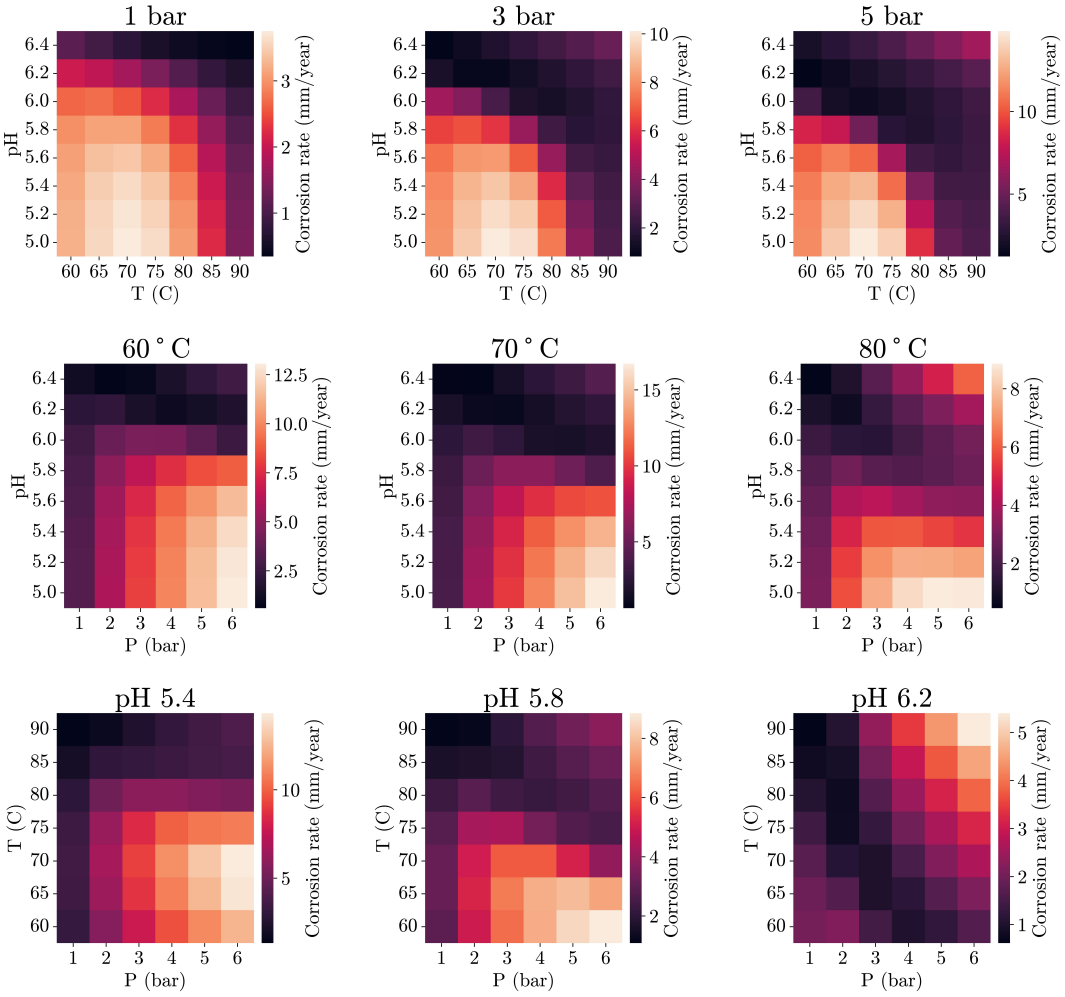


Figure 4.1: Matrix of heatmaps displaying the corrosion rate after 120 hours of simulation as a function of two of the following three parameters: temperature, pressure and pH. The third unused parameter is represented across each row of the matrix. Simulation conditions: 1% NaCl, 1 m^{-1} A/V, and a 2 cm diameter RCE at 1000 rpm.

The corrosion rate is examined in Fig. 4.1. The top row displays the T-pH heatmaps showing a low corrosion rate at high temperatures and (or) high pH likely due to the increased precipitation kinetics and carbonate concentration respectively which boost the precipitation rate. The corrosion rate decreases at low pH, however the maximum corrosion rate is achieved at 70 °C. This is attributed to the slower corrosion kinetics at lower temperatures. Increasing the total pressure from 1 bar to 5 bar does not change the relative corrosion rates significantly but it does increase the absolute corrosion rate due to the higher carbonic acid concentration. This is clearly observed in the P-pH heatmaps of the second row where the corrosion rate increases with the total pressure except at pH 6 and above where the corrosion rate is generally low across all pressures due to the formation of a protective corrosion scale. Furthermore, at 80 °C a new hotspot is observed at high pH and high pressure. Under these conditions there is a remarkably high amount of precipitation occurring in a short period of time resulting in an incomplete formation of the scale which is subsequently undermined by the corrosion process. The bottom row provides a better visualisation of this phenomenon. At pH 5.4 and 5.8 the precipitation rate is only high enough to form a protective corrosion scale at temperatures of 80 °C and above or at very low pressure otherwise the high pressure increases the corrosion rate to the point where the precipitation process is not fast enough to form a scale. At pH 6.2 the heatmap is notably different, the majority of the parameter space displays a low corrosion rate indicating the successful formation of a protective corrosion scale. However, at high pressure and high temperature there is an increase in corrosion rate due to the aforementioned intense but short-lived precipitation. Furthermore, the heatmap for pH 6.2 clearly divides the parameter space in three sections: the bottom left corner where the temperature and pressure are too low to generate enough precipitation to form a corrosion scale fast enough to overcome the steel dissolution, the top right corner where the temperature and pressure are too high to form a stable scale and a band separating these two section corresponding to the dark area of the heatmap that represents the section of the parameter space where a

protective scale has formed as indicated by the low corrosion rate.

Figure 4.2 displays the data for the fraction of the steel surface that is covered by the corrosion scale. The first row examines the T-pH heatmaps. At 1 bar high pH and high temperature correlate with a larger surface area the corrosion scale covers, in line with the corresponding heatmap from Fig. 4.1. However, at 3 and 5 bar the surface coverage of the corrosion scale is significantly lower at high temperature and high pH suggesting that scales formed at those conditions are likely to eventually detach from the steel surface. Instead, the higher coverage corrosion scales are found at high pH and low temperature which typically corresponds to a slow corrosion environment and a slow corrosion scale formation. On the second row the P-pH heatmaps show that most high coverage scales form under high pH and low pressure conditions. However, the scales formed at 80 °C exhibit a significantly larger surface coverage than those formed at lower temperatures. The bottom row clearly shows the band that separates the scales that have not yet formed (bottom left corner) from those scales that have formed but have lost their adhesion to the steel surface (top right corner). The band is particularly visible at pH 5.8 and 6.2 and represents scales with a large steel surface coverage. Additionally, it there exist a clear maxima for the surface coverage in most of the heatmap plots presented in Fig. 4.2. This suggests that one could in principle optimise the parameters to obtain the maximum surface coverage thereby maximizing the protectiveness of the formed scale.

The porosity of the corrosion scale is examined in Fig. 4.3. Overall, the porosity is predicted to decrease monotonically as the temperature, pressure and/or pH increases. This is attributed to the increased precipitation rate whenever any of these three parameters increases. Therefore, the porosity is predicted to be directly correlated with the precipitation rate as opposed to the scale surface coverage. Indeed, a high precipitation environment—high

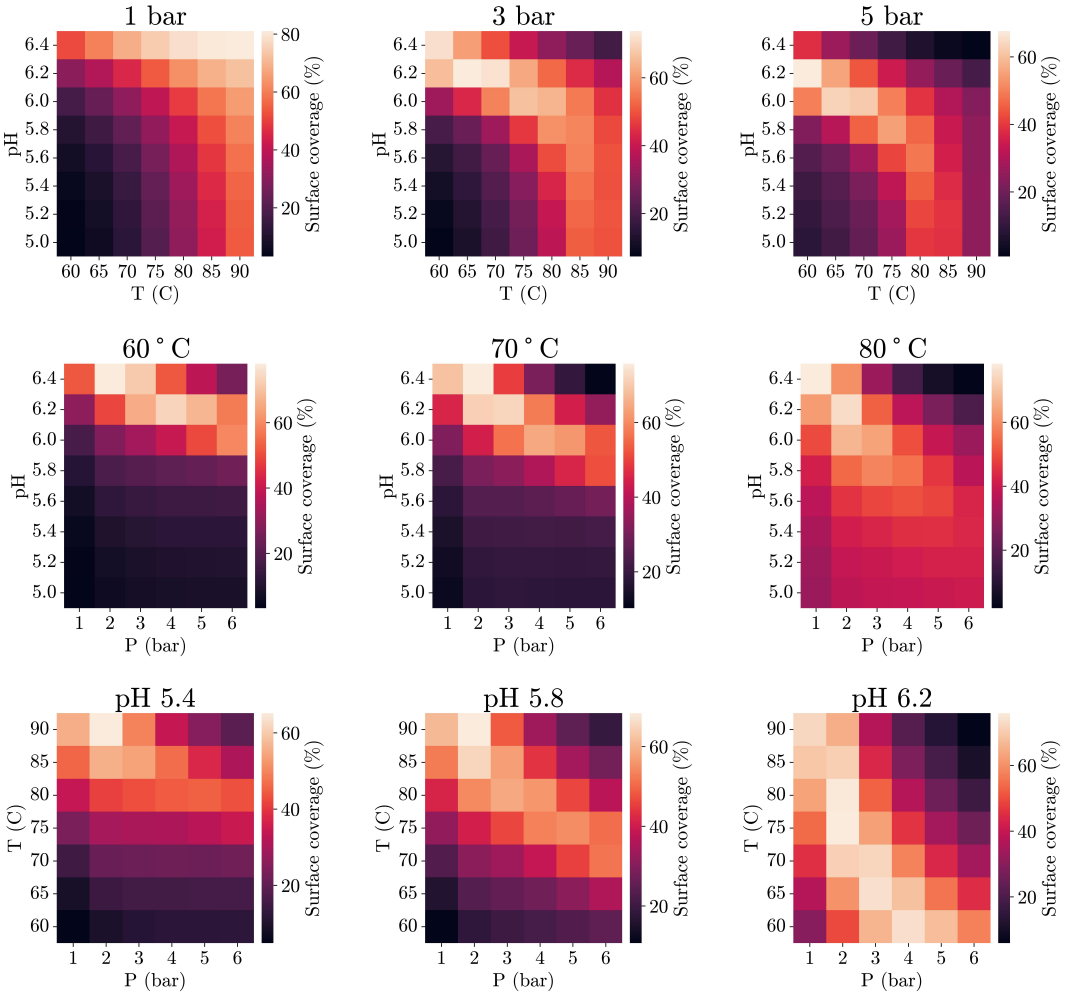


Figure 4.2: Matrix of heatmaps displaying the corrosion scale surface coverage after 120 hours of simulation as a function of two of the following three parameters: temperature, pressure and pH. The third unused parameter is represented across each row of the matrix. Simulation conditions: 1% NaCl, 1 m^{-1} A/V and a 2 cm diameter RCE at 1000 rpm.

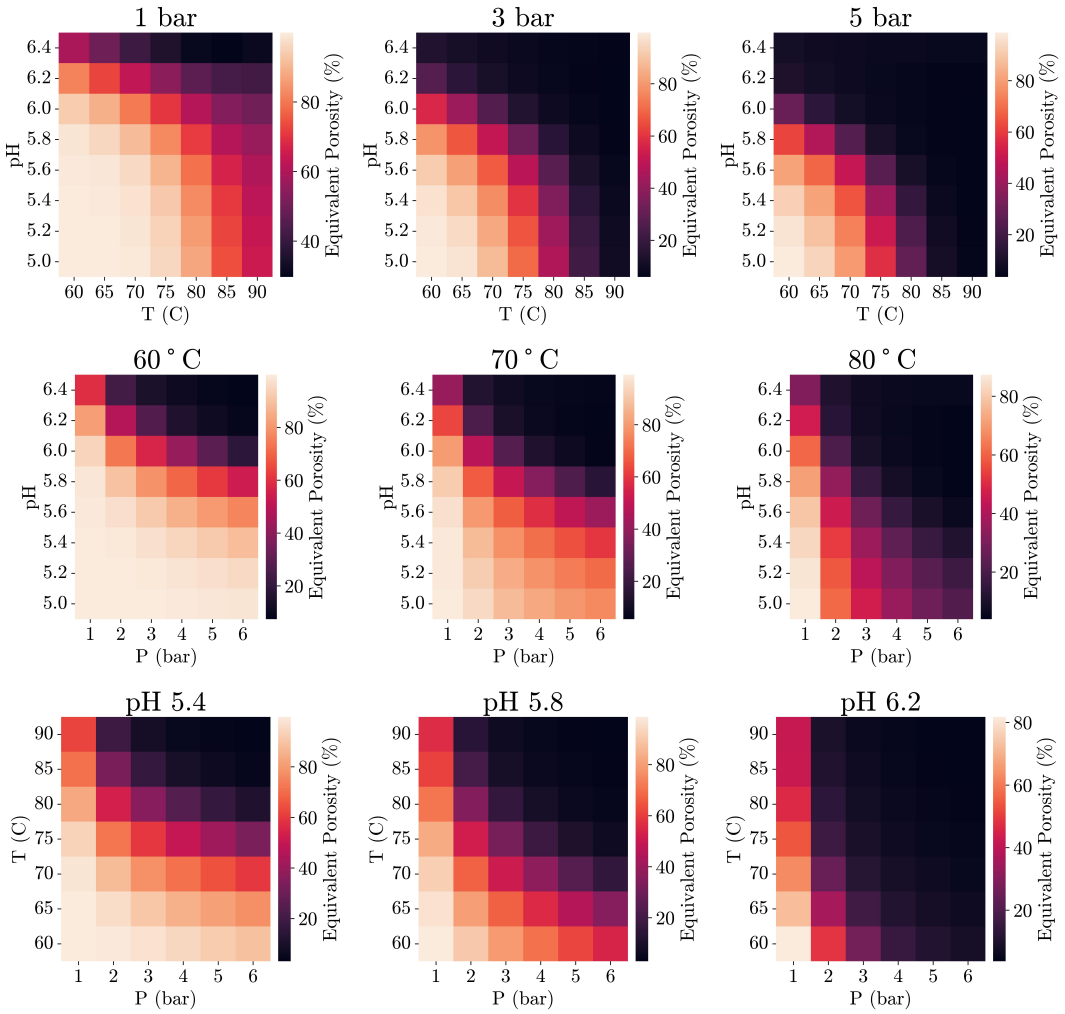


Figure 4.3: Matrix of heatmaps displaying the porosity after 120 hours of simulation as a function of two of the following three parameters: temperature, pressure and pH. The third unused parameter is represented across each row of the matrix. Simulation conditions: 1% NaCl, 1 m^{-1} A/V and a 2 cm diameter RCE at 1000 rpm.

temperature, high pressure and high pH—does not guarantee the protection of steel surface against corrosion as it is only weakly correlated with the surface coverage of the corrosion scale, however it is strongly correlated with the formation of a dense scale as observed in Fig. 4.3.

While it is important to develop a protective scale it is preferred to do so with minimal steel loss. In Fig. 4.4 the total volume of steel lost is investigated to better understand the trade-off between the rapid formation of a protective scale and the loss of steel incurred throughout the process. In Fig. 4.1 low corrosion rates are observed both at high pH and at high temperature, however the T-pH heatmaps from Fig. 4.4 suggest that there is a significant loss of steel associated with that corrosion rate reduction at high temperatures whereas the corrosion rate reduction observed at high pH is not predicted to come at the expense of a significant loss of steel. This is the result of two different mechanisms by which precipitation is enhanced. On the one hand, a temperature increase improves the precipitation kinetics at the expense of also increasing the corrosion reaction kinetics resulting in a considerable amount of steel dissolved. On the other hand, at high pH there is a high concentration of CO_3^{2-} which leads to a higher SS_{FeCO_3} faster than at low pH reducing the amount of steel that must dissolve in order to reach the same SS_{FeCO_3}. The lowest amount of steel lost is found at 90 °C, pH 6.4 and 1 bar due to the rapid formation of a corrosion scale that covers 80% of the steel surface—the highest surface coverage from all conditions tested (Fig. 4.2)—preventing further corrosion.

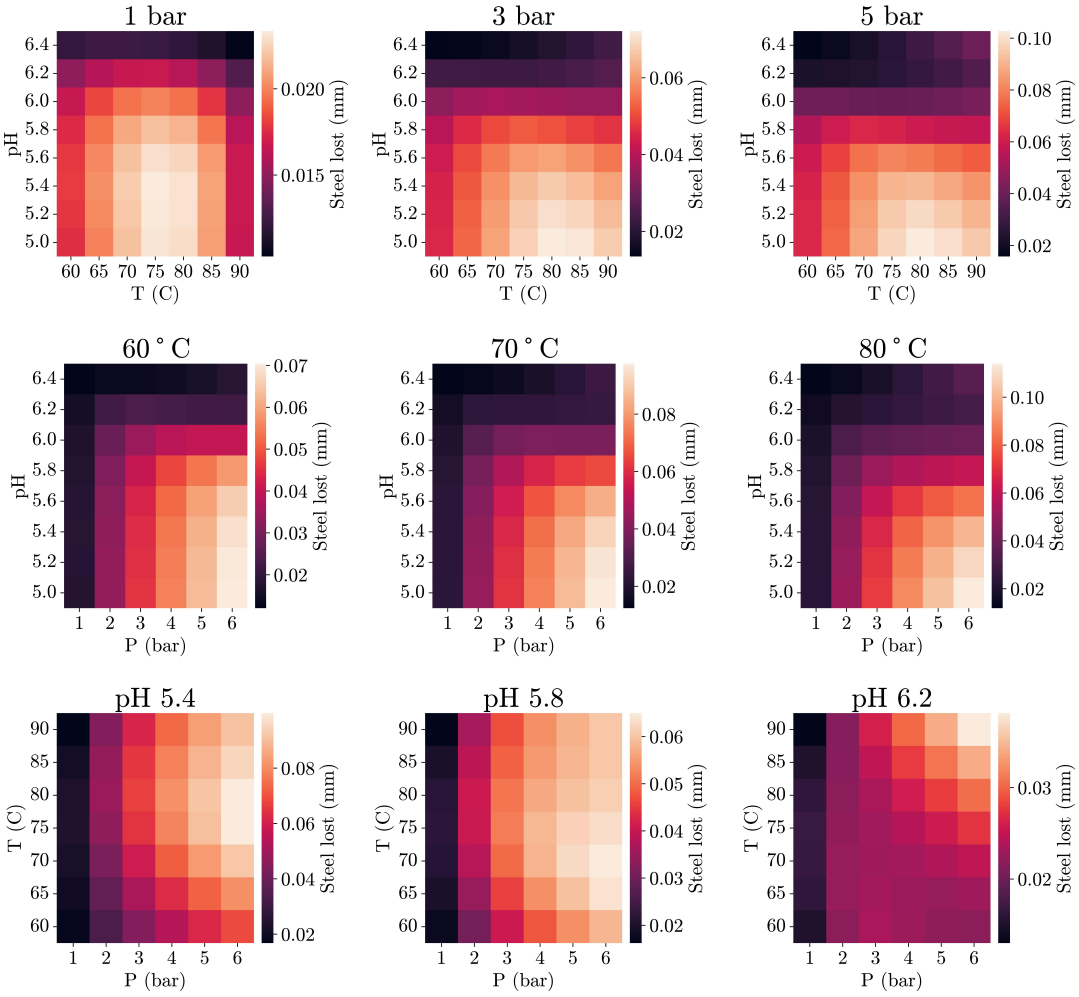


Figure 4.4: Matrix of heatmaps displaying the volume of steel lost after 120 hours of simulation as a function of two of the following three parameters: temperature, pressure and pH. The third unused parameter is represented across each row of the matrix. Simulation conditions: 1% NaCl, $1\,\mathrm{m}^{-1}$ A/V and a 2 cm diameter RCE at 1000 rpm.

4.3 Conclusions

In this chapter the intricate relationships amongst three key environment parameters—temperature, total pressure and initial pH—were investigated by carrying out simulations combining different values of these parameters in a grid-like approach and analysing the corrosion rate, surface coverage, porosity and total volume of steel lost after 120 hours of simulation time.

The results were analysed using a series of 3×3 matrices containing heatmaps of the metrics under study as a function of two of the three parameters investigated (temperature, total pressure and initial pH).

The predicted corrosion rates show that both the temperature and initial pH are positively correlated with the corrosion rate. The T-P heatmap at pH 6.2 revealed a band where the corrosion rate was the lowest. This band separates the region of the parameter space that leads to a porous scale (low temperature and pressure) from that where a corrosion scale has formed so fast that it could not cover most of the steel surface and the also fast steel dissolution undermines the steel underneath the scale (high temperature and pressure). The surface coverage supports this view as it shows a similar band for the same set of conditions. Additionally, Fig. 4.2 exhibits a clear maxima in the displayed heatmaps which opens new avenues to obtain the maximum scale protection by maximasing the corrosion scale coverage.

Unsurprisingly, the porosity of the corrosion scale was found to be positively correlated with low scaling conditions such as low temperature, low pH and low pressure.

Finally, the heatmaps displaying volume of steel lost due the oxidation reaction showed

that high temperatures lead to more metal loss than high pH despite forming scales with similar protection against corrosion. This is due to the fact that the corrosion kinetics are enhanced at high temperatures. The corrosion system simulated at 90 °C, pH 6.4 and 1 bar was found to lose the lowest amount of steel due to the fast and complete formation of the corrosion scale.

Chapter 5

Additional use cases

5.1 Introduction

The SLCA model is designed to be modular and flexible so that it can be adapted to a wide range of different scenarios. This chapter explores two unique applications of the SLCA model.

Firstly, the model is used to study the stability of the corrosion scale upon a change in the environment, at use case commonly encountered in the field. Secondly, an inhibitor model is build on top of the SLCA model to investigate the effect of the inhibitor on the corrosion scale. The inhibitor protection mechanism is based on blocking the corrosion active sites.

5.2 Changes in the environment

In both experiments and models the environment conditions are generally kept fixed while the experiment or simulation is running. In this way, one can map the results to a specific set of conditions and be confident about the rationale of the conclusions. However, the conditions in the field are rarely ever constant. The environment inside an oil and gas pipeline evolves as the oil reservoir depletes and the chemistry and composition of the multiphase system changes. Under such a dynamic environment there is a concern about the stability of a "protective" corrosion scale once the environment changes. Additionally, one of the suggested approaches to utilise protective properties of the $FeCO_3$ scale is to purposefully grow the scale in a controlled environment that promotes the formation of a protective scale and then deploy the pipe in the field where it will be exposed to a different environment. For this approach to work it is important to understand how will the scale be affected by the new environment and, in particular, whether the protection provided by the scale remains after exposing it to the new environment.

The model presented in this work is able to simulate these scenarios by changing the simulation environment after a specified amount of time. This section explores how different changes in the environment affect the protective properties of a fully formed scale. The simulation is divided in two stages of 3 hours each. During the first stage the conditions are chosen such that the growth of a reasonably protective scale is encouraged. The initial conditions of this first stage are as follows: 80 °C, pH 6.5, 1 bar, 1% NaCl, $1\,\mathrm{m}^{-1}$ A/V and 1 m/s in a 0.2 m diameter pipe. Figure 5.1 shows the corrosion rate, surface coverage and equivalent porosity for a 5-day simulation using this set of conditions. After approximately 3 days the corrosion rate reaches its lowest value which indicates that the protection of the scale is at its highest. In the second stage one of the initial parameters is changed and the

iron concentration in solution is reset back to zero. This two-step simulation represents the process of artificially growing the protective film off-site and deploying the pipe in a different environment. Three different environment parameters are investigated: the temperature, initial pH, pressure. Figures 5.2 to 5.4 display the formation of the scale from Fig. 5.1 for 3 days followed by a reset of the solution chemistry to their initial values, a change in a single environment parameter and another 3-day simulation under the new environment.

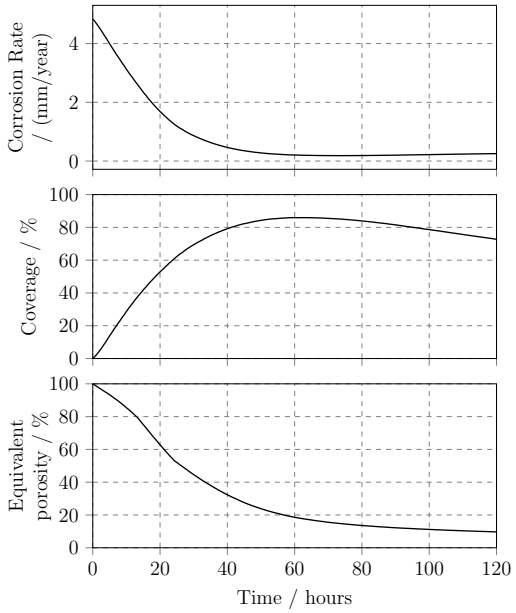


Figure 5.1: Model predictions of the corrosion rate, corrosion scale surface coverage and equivalent porosity. Simulation conditions: 80 °C, pH 6.5, 1 bar, 1% NaCl, 1 m^{-1} A/V and 1 m/s in a 0.2 m diameter pipe.

Effect of temperature

Figure 5.2 shows the effect of the temperature on the corrosion process of a steel surface with a corrosion product layer. After the formation of the scale the corrosion rate, bulk pH, equivalent porosity, precipitation rate and surface coverage were computed for a period of 3 days at 70 °C, 80 °C and 90 °C.

The corrosion rate is predicted to remain low with minimal differences between the different temperatures suggesting that the protection of the scale is not significantly affected after a temperature change. As the Fe^{2+} concentration slowly increases due to the corrosion reaction the pH increases. The increase in pH occurs at different rates for each temperature because of the differences in thermodynamic equilibrium constants involved in the carbonate equilibria. The higher pH results in a higher concentration of CO_3^{2-} which combined with the increase in Fe^{2+} concentration leads to an increase in SS_{FeCO_3}. This increase is higher at low temperatures where the $FeCO_3$ solubility product (K_{sp}) is higher.[73] The precipitation rate remains relatively similar amongst the different temperatures despite the differences in SS_{FeCO_3}. This is attributed to a combination of small differences in the starting corrosion rate and the faster precipitation reaction kinetics at high temperatures. The surface coverage of the corrosion scale is virtually identical in the three temperatures tested due to the similar precipitation rate.

Overall, a change in temperature does not result in significant changes to the corrosion or precipitation rates according to the model's prediction so the effect on the scale is negligible for the duration of the simulation.

Effect of pH

Figure 5.3 examines how a formed scale responds to three different pH environments: pH 5.5, 6 and 6.5. The differences in pH result in different CO_3^{2-} concentrations which determine the SS_{FeCO_3} and, consequently, the precipitation. The difference in precipitation rate is immediately observed after the change of pH at the 3-day mark with a faster precipitation at higher pH (Fig. 5.3). At pH 5.5 and 6 the corrosion rate gradually increases as the precipitation rate can no longer keep up with the corrosion rate leading to a decline in corrosion scale

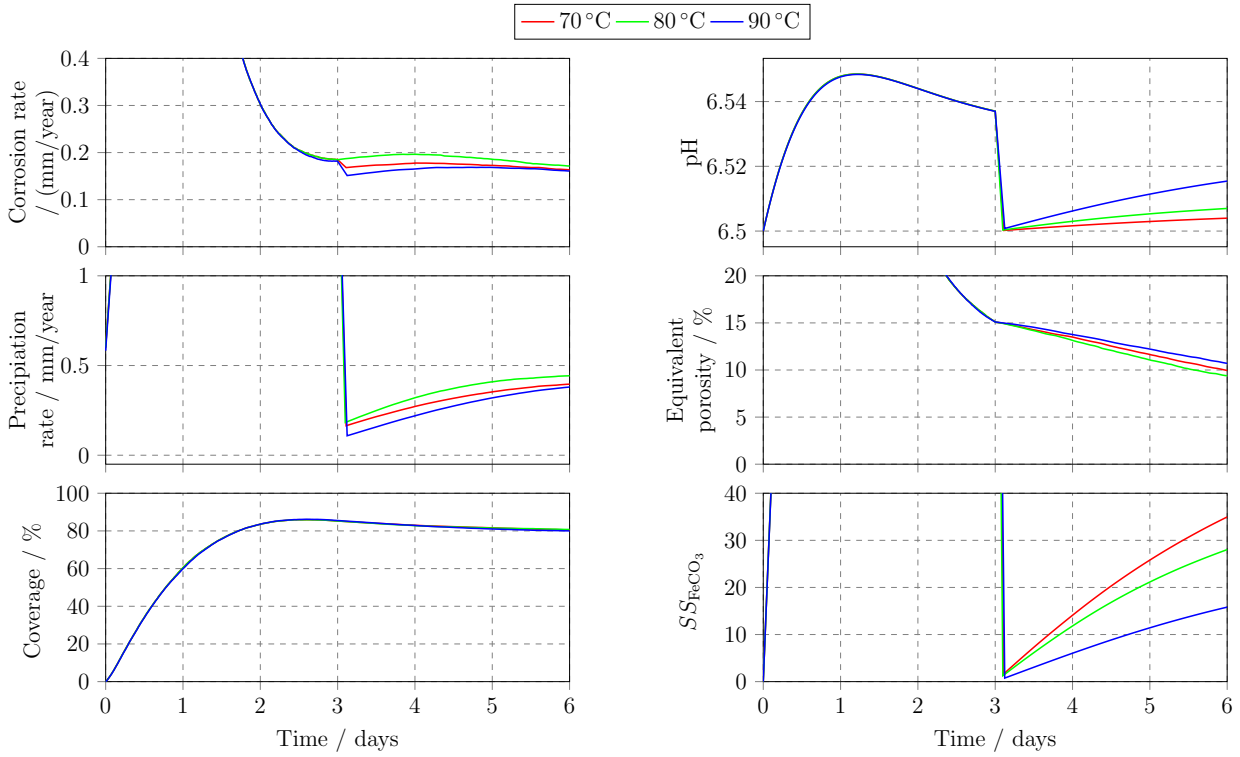


Figure 5.2: Model predictions of the corrosion rate, precipitation rate, surface coverage, bulk pH, equivalent porosity and SS_{FeCO_3} for a 3-day simulation at 80 °C, pH 6.5, 1 bar, 1% NaCl, $1\,m^{-1}$ A/V and 1 m/s in a 0.2 m diameter pipe followed by a water chemistry reset, a change in temperature to 70 °C, 80 °C and 90 °C and another 3-day simulation.

coverage. On the other hand, at pH 6.5 the precipitation rate rises fast enough that the coverage of the corrosion scale barely changes. Indeed, due to the higher CO_3^{2-} concentration at pH 6.5 the supersaturation is able to recover faster from the lack of Fe^{2+} ions in solution and the stability of the scale is maintained. Furthermore, the corrosion rate at pH 6.5 decreases slightly due to the significant increase in scale density compared to pH 5.5 and pH 6.

The effect of pH predicted by the model is significant. At relatively low pH the model predicts that even a considerably dense scale that covers the majority of the steel surface can be susceptible to breakdown due to the corrosion undermining the corrosion scale. This could be partially mitigated if the new environment already contained enough concentration of Fe^{2+} ions to maintain the original precipitation rate.

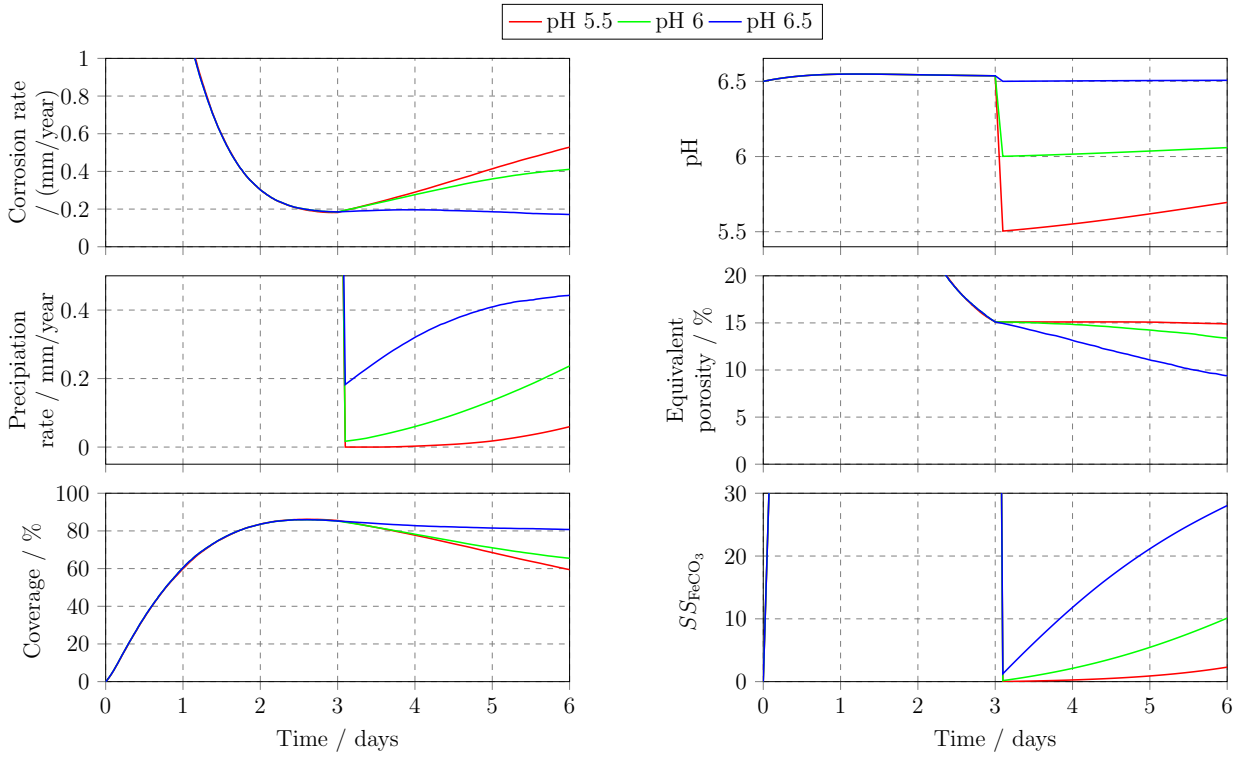


Figure 5.3: Model predictions of the corrosion rate, precipitation rate, surface coverage, bulk pH, equivalent porosity and SS_{FeCO_3} for a 3-day simulation at 80 °C, pH 6.5, 1 bar, 1% NaCl, 1 m^{-1} A/V and 1 m/s in a 0.2 m diameter pipe followed by a water chemistry reset, a change in pH to pH 5.5, pH 6 and pH 6.5 and another 3-day simulation.

Effect of pressure

Figure 5.4 presents the effect of pressure on the corrosion scale for 1, 2 and 3 bar environments. An increase in total pressure results in an increase in the partial pressure of CO_2 and, hence, and increase in the concentration of all carbonate species. An increase in the carbonic acid concentration leads to a stronger *buffering* effect which fuels the HER with H^+, hence, an increase in the total pressure results in a higher corrosion rate. Similarly, an increase in the concentration of CO_3^{2-} results in a higher SS_{FeCO_3} and, therefore, a higher precipitation rate. Since both the corrosion rate and precipitation rate are expected to increase simultaneously it is not trivial to determine whether the scale will keep the same level of protection as the

pressure increases without simulating the specific environment with a corosion model such as the one presented herein.

The precipitation rate at 3 bar continues at roughly the same rate after the first 3-day simulation due to the high CO_3^{2-} concentration. On the other hand, the corrosion rate starts significantly higher than the original due to the increased H_2CO_3 concentration, however it decreases momentarily as the as porosity of the scale decreases due to the high precipitation rate. The precipitation rate also decreases with the corrosion rate due to the lower SS_{FeCO_3} inside the scale, however it increases again once the bulk SS_{FeCO_3} recovers from the lack of Fe^{2+} ions in solution. Similar but less pronounced changes are observed at 2 bar. Both the 2 and 3 bar simulations exhibit a rapid decline in corrosion scale surface coverage due to equally rapid increase in corrosion rate. However, the simulation at 1 bar maintains a low corrosion rate despite the also low precipitation rate due to the stable corrosion scale surface coverage and the constant decline of the scale porosity.

Overall, a change in the total pressure can have a significant effect on the protective properties of the scale. In particular, if the environment changes to higher pressures the corrosion process is predicted to undermine the corrosion scale which can eventually cause the detachment of the scale from the steel surface.

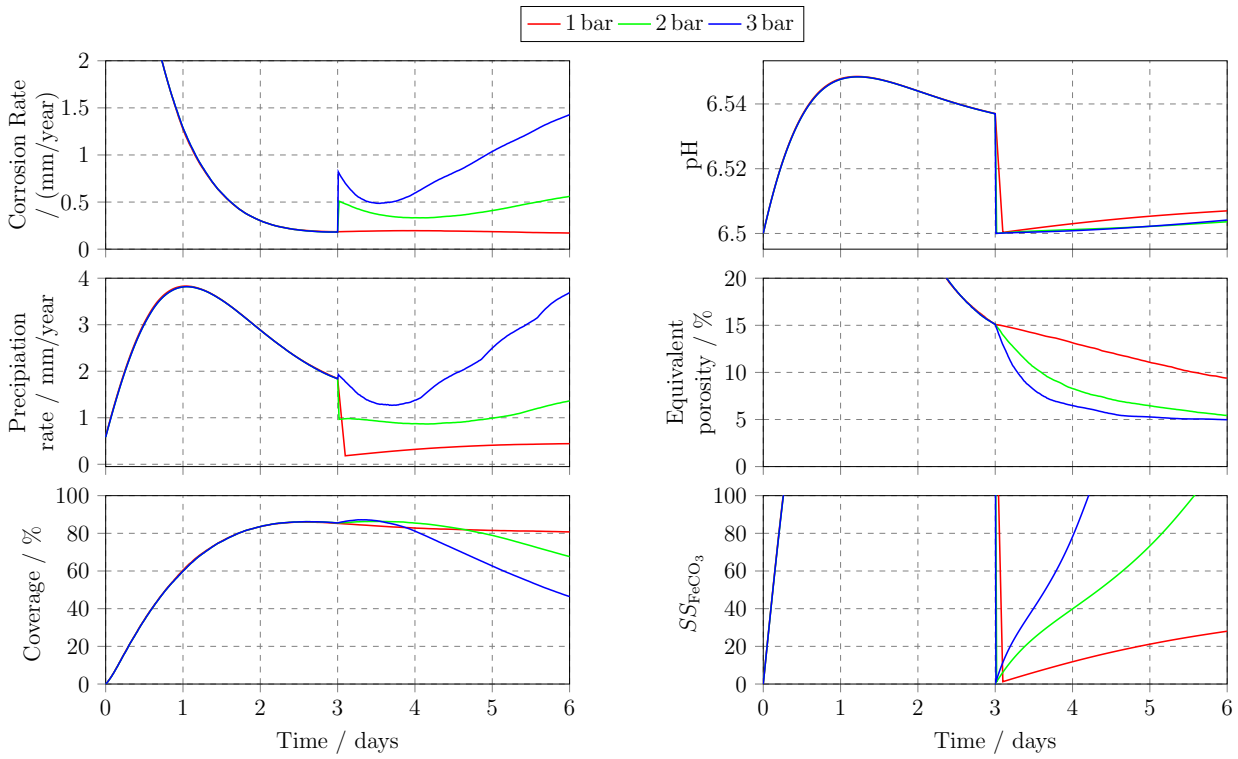


Figure 5.4: Model predictions of the corrosion rate, precipitation rate, surface coverage, pH, bulk $[Fe^{2+}]$ and SS_{FeCO_3} for a 3-day simulation at 80 °C, pH 6.5, 1 bar, 1% NaCl, 1 m^{-1} A/V and 1 m/s in a 0.2 m diameter pipe followed by a water chemistry reset, a change in temperature to 70 °C, 80 °C and 90 °C and another 3-day simulation.

5.3 Corrosion inhibitor protection

The use of corrosion inhibitors has been one the most cost-effective corrosion prevention and mitigation strategies for decades.[108,109] However, the mechanism by which these chemicals inhibit corrosion is still not fully understood.[110] The corrosion inhibitors used in the oil and gas industry are typically surfactant molecules—organic molecules with a hydrophilic head and a hydrophobic tail—that adsorb onto the steel surface and inhibit the corrosion process in various ways such as physically blocking active sites on the surface of the steel or by chemically displacing electroactive species.[110]

In CO_2 corrosion, inhibitors are designed to either inhibit the cathodic reaction or promote the formation of the corrosion product layer.[110] However, the inhibition mechanism of some of the most commonly used inhibitors such as imidazolines is still unknown.[109]

The goal of this section is to investigate the effect of inhibitors on the corrosion process including their interaction with the corrosion scale. Since the inhibition mechanism of most common CO_2 corrosion inhibitors is not known we define a generic inhibition model whereby the inhibitor adsorbs to the surface and physically blocks active corrosion sites. This inhibition model has one single parameter θ_I that determines the fraction of the surface covered by the inhibitor or, equivalently, the fraction of active corrosion sites blocked by the inhibitor. θ_I can be obtained experimentally by fitting the corrosion rate data to the appropriate adsorption isotherm.[108] The model assumes that the inhibitor adsorbed on the steel surface is in equilibrium with the concentration of inhibitor in solution and that the fraction of the surface covered by adsorbed inhibitor (θ_I) is constant throughout the corrosion process. However, this adsorption equilibrium is a dynamic process where inhibitors can desorb and readsorb onto a different part of the surface as long as the same fraction of the surface is

covered by inhibitor. For the sake of simplicity, the model further assumes that the inhibitor is equally as likely to attach to the corrosion scale than to the steel surface, however when the inhibitor attaches to the corrosion scale it does not provide any corrosion protection to the steel surface.

The CO_2 corrosion model developed in this work is a discrete model so the surface of the steel is covered by the inhibitor in discrete area units (Δz^2). However, this does not impact the inhibition mechanism as the steel dissolution process is subject to the same constraints. At every time interval the inhibitor model samples $\theta_I \times N$ area units where N is the total number of surface area units exposed to the electrolyte (both steel and scale surfaces combined) and marks those surface units as protected by the inhibitor.

Using this simple inhibitor model the corrosion process is studied as a function of the parameter θ_I. The system used for this study was simulated for 5 days and was initialised with the following conditions: pH 6, 80 °C, 1 bar, 1% NaCl, 1 m^{-1} A/V and 20 mm RCE at 1000 rpm. Figure 5.5 shows the corrosion and precipitation rate, the bulk pH of the solution and the surface coverage, equivalent porosity and thickness of the scale for a corrosion system with an inhibitor with a θ_I of 0%, 25%, 50% and 75%. The corrosion rate of those environments that contain the inhibitor ($\theta_I > 0$) is noisy as a consequence of the stochastic adsorption of the inhibitor on the surface coupled with the stochastic corrosion process. As expected, the presence of an inhibitor decreases the corrosion rate. The initial corrosion rate is reduced by the same fraction of inhibitor steel surface coverage. A reduction in corrosion rate results in less Fe^{2+} ions in solution which reduces both the pH and the SS_{FeCO_3}. Therefore, there is lower corrosion product precipitation at higher inhibitor surface coverage. Despite the lower precipitation the scale formed is less porous, thinner and covers a larger portion of the steel surface compared to scales formed at lower inhibitor coverage or without inhibitor (Fig. 5.5).

This is also apparent in the cross-section images at the end of the 5 days (Fig. 5.6) where the system with no inhibitor exhibits a thick and irregular scale with a porous steel-scale interface. As the inhibitor coverage increases the scale becomes thinner and less porous and the steel-scale interface becomes flatter which favours the adhesion of the scale to the steel surface.

Overall, the addition of a corrosion inhibitor that blocks active corrosion sites not only reduces the corrosion rate by changing the effective area exposed to the electrolyte but by doing so it creates an environment that encourages the growth of protective scales, i.e. uniform dense scales with good adhesion to the underlying steel surface.

Furthermore, the absolute reduction in the initial corrosion rate is roughly constant throughout the simulation as opposed to being proportional to the corrosion rate without inhibitor. This is an important result as it leads to a significantly faster decrease in corrosion rate and it is attributed to the aforementioned enhancement to the formation of the corrosion product layer.

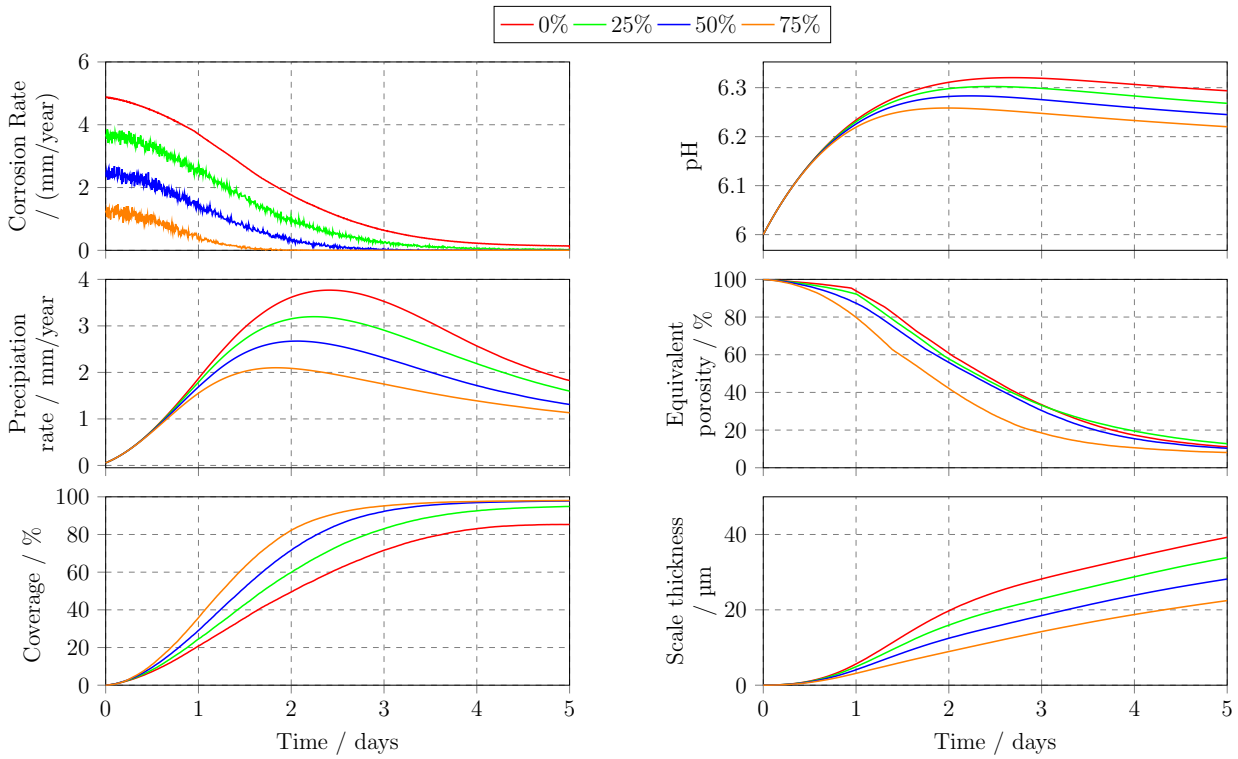


Figure 5.5: Model predictions of corrosion rate, surface coverage and equivalent porosity for 1 bar, 2 bar and 3 bar. Simulation conditions: 80 °C, 1% NaCl, 1 m^{-1} A/V and 1000 rpm.

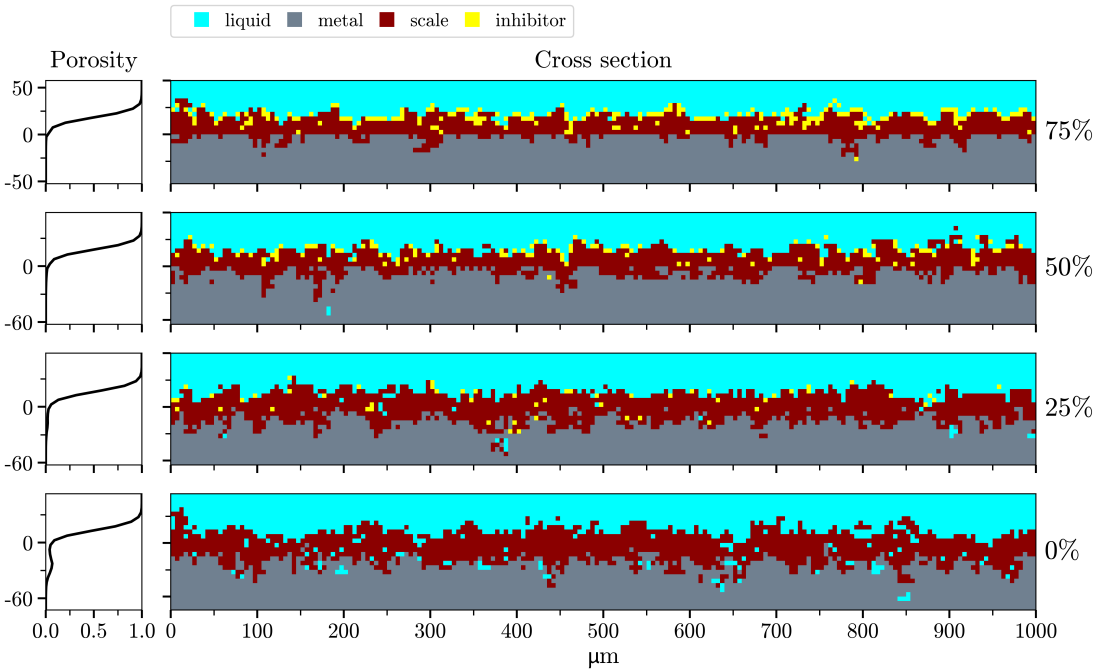


Figure 5.6: Cross-sections and porosity profiles of the 3-dimensional simulation cells after 120 hours of simulation for 60, 70 and 80 °C. Simulation conditions: 80 °C, 1 bar, pH 6, 1% NaCl, 1 m^{-1} A/V and 1000 rpm.

5.4 Conclusions

This chapter presented two modified versions of the SLCA model to tackle two unique use cases where and adapted version of the SLCA model was used to provide valuable insight.

In the first section the stability of a fully formed CO_2 corrosion scale is tested after a change in the environment. In the field, some environment parameters may change gradually over time or the pipeline may be "pre-conditioned" to grow a protective scale before being deployed to the field. This section focused on the latter use case for simplicity. Firstly, a dense corrosion scale covering more than 80% of the steel surface was formed after a 3-day simulation at 80 °C, pH 6.5, 1 bar, 1% NaCl, 1 m^{-1} A/V and 1 m/s in a 0.2 m diameter pipe. Then, Fe^{2+} concentration was reset back to zero and one of the simulation conditions was changed to simulate the transfer of the pipe to a new environment. Finally, the simulation continued for 3 more days in the new environment. Three different environment parameters were tested: the temperature (70, 80 and 90 °C), the initial pH (pH 5.5, 6 and 6) and the total pressure (1, 2 and 3 bar). The temperature changes did not have any significant impact on the scale or the corrosion and precipitation rates. pH changes did have a strong effect at both pH 5.5 and 6 where the scale coverage decreased due to a low precipitation rate which resulted in a gradual increase of the corrosion rate over time. The changes in the total pressure led to a momentary decrease followed by a gradual increase of both the corrosion and precipitation rates at 2 and 3 bar. This was attributed to an initial increase in scale density—corresponding to the temporary decrease in corrosion rate—and a subsequent decline in scale coverage —corresponding to the gradual increase in corrosion rate. The corrosion rate at 1 bar remained low for the duration of the simulation despite the also low precipitation rate. This ensured a stable corrosion scale surface coverage and a constant decline of the scale porosity for the duration of the simulation.

The second section presented a corrosion inhibitor model where corrosion inhibitor is adsorbed onto a fraction of the surface area (both steel and scale) determined by the parameter θ_I. The inhibitor adsorption is modelled as a dynamic equilibrium where the inhibitor desorbs and readsorbs onto the metal or scale surface while maintaining a surface coverage of θ_I. The inhibitor model further assumes that the inhibitor is equally as likely to adsorb on the metal than on the scale and adsorbing on the scale surface provides no corrosion protection and does not affect the scale in any way. This simple inhibitor model was tested for a θ_I of 0%, 25%, 50% and 75%. Unsurprisingly, the initial corrosion rate is reduced by the same θ_I fraction. However, as a side-effect of the lower corrosion rates the corrosion scales become thinner, flatter and less porous for higher values of θ_I which further decreases the corrosion rate. Therefore, corrosion inhibitors with a similar inhibition mechanism to the one described for this inhibitor model are expected to benefit from not only a reduction of the corrosion rate but also the formation of a more protective corrosion scale.

The inhibitor model could be further improved by calculating the relative adsorption energy between steel-inhibitor and scale-inhibitor to obtain the relative tendency of the inhibitor to adsorb on top of steel and scale. Then, this relative adsorption chance can be incorporated into the inhibitor model.

Overall, this chapter showcases the flexible capabilities of the SLCA model. By applying simple modifications to the base model one can reproduce unique scenarios or build additional models taking SLCA as a base.

Chapter 6

Atomistic scale corrosion modelling

6.1 Introduction

The development of new prevention and mitigation strategies for CO_2 corrosion requires a deep understanding of the corrosion process at an atomistic scale. A large body of literature studies the corrosion process using *ab initio* methods and atomistic simulations such as Density Functional Theory (DFT), Molecular Dynamics (MD) and Monte Carlo (MC).[111,112]. These new computational methods open new avenues for the prevention and mitigation of corrosion and enable the design of new types of corrosion inhibitors based on their molecular interaction with the metal surface.[113] In particular, DFT simulations have been used extensively to study the initial stages of the corrosion process at the atomic scale and the interaction of inhibitors molecules with metallic surfaces.[113–117] However, CO_2 corrosion atomistic studies are still lacking due to the complexity of these environments. DFT can also provide new insights on the adsorption of inhibitor molecules on the steel surface and on the corrosion scale which

could. Inhibitor adsorption energies can be interpreted as the relative binding strength of a molecule to a surface which could be incorporated to the inhibitor model described in Section 5.3 as the probability of attaching to either the steel surface or the corrosion scale surface. This chapter aims to revisit our fundamental understanding of corrosion in simplified chemical systems in order to build a solid foundation for future research on the topic.

6.2 Density Functional Theory

DFT is an *ab initio* ("from first principles") quantum mechanical method for calculating the electronic structure of chemical systems. DFT aims to deliver results with an accuracy comparable to other well established ab initio techniques (e.g. Hartree Fock) at a fraction of their computational cost. To achieve this DFT operates on the electron density of the whole system rather than the individual wave functions of every single electron.

6.2.1 Schrödinger equation

In principle, the total energy of a quantum-mechanical system can be calculated using the non-relativistic time-dependent Schrödinger equation:

$$i\hbar\frac{d}{dt}\left|\Psi(t)\right\rangle = \hat{H}\left|\Psi(t)\right\rangle \tag{6.1}$$

where Ψ is the wave function of the system and $\hat{H}$ is the Hamiltonian operator. However, often only the ground state of the chemical system is of interest and the non-relativistic

time-independent Schrödinger equation can be used instead.

$$\hat{H}\,|\Psi\rangle = E\,|\Psi\rangle \tag{6.2}$$

where E is the total energy of the system. The Hamiltonian operator is composed of the kinetic energy of electrons and nuclei, and the potential energy of all the particle interactions.

$$\hat{H} = \hat{T}_e + \hat{T}_n + \hat{V}_{ee} + \hat{V}_{en} + \hat{V}_{nn} \tag{6.3}$$

where $\hat{T}_e$ is the electron kinetic energy, $\hat{T}_n$ is the nucleus kinetic energy, $\hat{V}_{ee}$ is the electron-electron repulsive interaction, $\hat{V}_{nn}$ is the nucleus-nucleus repulsive interaction and $\hat{V}_{en}$ is the electron-nucleus attractive interaction. The expanded Hamiltonian operator for a system of N electrons and M protons can be expressed in atomic units as follows:[118]

$$\begin{aligned}\hat{H} = &\sum_{i=1}^{N} \frac{-\nabla_i^2}{2} + \sum_{A=1}^{M} \frac{-\nabla_A^2}{2M_A} + \sum_{i=1}^{N}\sum_{j>i}^{N} \frac{1}{|r_i - r_j|} \\ &+ \sum_{i=1}^{N}\sum_{A=1}^{M} \frac{-Z_A}{|r_i - R_A|} + \sum_{A=1}^{M}\sum_{B>A}^{M} \frac{Z_A Z_B}{|R_B - R_B|}\end{aligned} \tag{6.4}$$

where M_A is the mass of nucleus A, r and R are the electron and nucleus positions respectively, electron-nucleus and nucleus-nucleus absolute distances respectively; and Z_A and Z_B are the charge of nucleus A and B.

6.2.2 Born-Oppenheimer approximation

The mass of a nucleus is typically several orders of magnitude larger than the mass of an electron. Consequently, the electrons move at such high speeds relative to the movement of

the nuclei that we can consider the nuclei to be static relative to the electron movement. This is known as the Born-Oppenheimer approximation.[119]

This approximation has several implications. First of all, the wave functions of electrons and nuclei are no longer coupled and, therefore, the total wave function of the system can be expressed as the product of the electronic (ψ_e) and the nuclear (ψ_n) wave functions:

$$\Psi_{total} = \psi_e \psi_n \tag{6.5}$$

Consequently, the Schrödinger equation can now be solved independently for the electronic and nuclear wave functions:

$$\hat{H}_e \left|\psi_e\right\rangle = E_e \left|\psi_e\right\rangle \tag{6.6}$$

$$\hat{H}_n \left|\psi_n\right\rangle = E_n \left|\psi_n\right\rangle \tag{6.7}$$

Applying the Born-Oppenheimer approximation to the electronic system we can obtain the electronic Hamiltonian ($\hat{H}_e$) from Eq. (6.3) by only including electronic interactions:

$$\hat{H}_e = \hat{T}_e + \hat{V}_{ee} + \hat{V}_{en} \tag{6.8}$$

where due to the fact that the nuclei are considered fixed in space $\hat{V}_{en}$ now depends only *parametrically* on the nuclear positions (R) and $\hat{T}_n$ is zero. The total energy (E_{total}) can then be obtained by adding the $\hat{V}_{nn}$ contribution which is constant within the Born-Oppenheimer approximation.

$$E_{total} = E_e + \hat{V}_{nn} \tag{6.9}$$

Therefore, the total energy can be obtained through the electronic Hamiltonian up to a constant.

6.2.3 Molecular orbitals

An orbital is a wave function of a single electron. A chemical system composed of a single atom contains atomic orbitals. To fully define an electron these orbitals must include both a spatial and spin components (*spin orbitals*):

$$\chi(x) = \begin{cases} \psi(r)\alpha(\omega) \\ \quad \text{or} \\ \psi(r)\beta(\omega) \end{cases} \tag{6.10}$$

where $\chi(x)$ is a *spin orbital* wave function, $\psi(r)$ is the spatial component of the orbital and α and β are the two possible spin configurations.

There are two commonly used types of atomic orbitals Slater-type orbitals (STOs) and Gaussian-type orbitals (GTOs). STOs have the following radial form:

$$\psi(r)^{\text{STO}} \propto r^l e^{-\zeta r} \tag{6.11}$$

l is the angular momentum, r is the distance of the electron from the nucleus and ζ is the effective nuclear charge. On the other hand, GTOs use Gaussian functions to describe the radial component of the orbital:

$$\psi^{\text{GTO}}(r) \propto r^l e^{-\zeta r^2} \tag{6.12}$$

Chemical systems with more than one atom are composed of molecular orbitals. Molecular

orbitals can be estimated using a Linear Combination of Atomic Orbitals (LCAO).[120]

$$\Psi = \sum_i a_i \chi_i \tag{6.13}$$

Atomic orbitals need to obey Pauli exclusion principle, i.e. the orbitals wave function must be antisymmetric with respect to the interchange of any two electrons. Slater determinants meet the antisymmetry requirement and are widely used as molecular wave functions.[121] They have the following atomic functions meet the antisymmetry requirement.[121] They have the following form:

$$\Psi(x_1, x_2, \dots, x_N) = (N!)^{\frac{1}{2}} \begin{vmatrix} \chi_1(x_1) & \chi_2(x_1) & \cdots & \chi_N(x_1) \\ \chi_1(x_2) & \chi_2(x_2) & \cdots & \chi_N(x_2) \\ \vdots & \vdots & \ddots & \vdots \\ \chi_1(x_N) & \chi_2(x_N) & \cdots & \chi_N(x_N) \end{vmatrix} \tag{6.14}$$

where N is the number of electrons and $(N!)^{\frac{1}{2}}$ is a normalisation constant. The rows of the determinant represent the electrons whereas the columns represent the orbitals. Slater determinants exhibit *exchange correlation*—correlation in the movement between two electrons with parallel spins—which arises naturally from the antisymmetry requirement.

6.2.4 Variational principle

According to the variational principle, for any normalised wave function ψ the ground state energy (E_0) has an upper bound given by:

$$E_0 \leq \langle \psi | \hat{H} | \psi \rangle \tag{6.15}$$

Therefore, we can obtain the best estimate of the ground state energy by finding the spin orbitals that minimize the energy subject to the constraint that spin orbitals remain ortonormal.

6.2.5 Hartree-Fock approximation

Because the electronic Hamiltonian ($\hat{H}_e$) contains an electron-electron repulsion term ($\hat{V}_{ee}$) it is necessary to reformulate the 2-electron operator as a 1-electron operator so that the eigenfunction equation can be split into a set of 1-electron equations. Hartree proposed using the mean field approximation (MFT) to substitute all electron-electron interactions with the 1-electron interaction with an average potential of the other $N-1$ electrons.[122–124] The Fock operator can then be defined as:[118]

$$\hat{F}(1) = \hat{h}(1) + \sum_{j=1}^{N/2}[2\hat{j}_j(1) - \hat{k}_j(1)] \tag{6.16}$$

where the (1) indicates that these are 1-electron operators, $\hat{h}(1)$ are the 1-electron terms of the electronic Hamiltonian, $\hat{j}_j(1)$ is the Coulomb operator and $\hat{k}_j(1)$ is the exchange operator arising from the antisymmetric nature of the wave function.

$$\hat{h}(1) = -\frac{1}{2}\nabla_1^2 - \sum_A \frac{Z_A}{r_1 A} \tag{6.17}$$

$$\hat{j}(1) = -\int dx_2 \chi_b^*(2)\frac{1}{r_{12}}\chi_b(2) \tag{6.18}$$

$$\hat{k}(1) = -\int dx_2 \chi_b^*(2)\frac{1}{r_{12}}\chi_a(2) \tag{6.19}$$

Then, the one-electron wave functions can be obtained by solving the following eigenfunction equation:

$$\hat{F}(1)\chi_i(1) = E_i\chi_i(1) \tag{6.20}$$

where $\chi_i(1)$ refers to the set of 1-electron molecular orbitals. This equation can be solved using the self-consistently field (SCF) method.

While the Hartree-Fock method provides a good approximation of the ground state the computational cost scales as $3N$ where N is the number of electrons in the system as each 1-electron molecular orbital must be determined in a 3-dimensional coordinate system.

6.2.6 Hohenburg-Kohn Theorems

In an electronic system defined by the Hamiltonian described in Eq. (6.8) both the ground-state energy E_0 and the associated wave function Ψ_0 can be obtained by minimising the energy using the variational principle (Eq. (6.15)). The Hamiltonian is completely defined by the external (nuclear) potential $\upsilon_{\text{ext}}(r)$ and the number of electrons of the system. Therefore, the wave function of an system with N electrons is also determined uniquely by $\upsilon_{\text{ext}}(r)$.

$$\upsilon_{\text{ext}} \rightarrow \hat{H} \rightarrow \Psi \tag{6.21}$$

In 1964, Hohenberg and Kohn [125] proposed two theorems that would become the foundation of DFT. The first theorem notes that the external potential $\upsilon_{\text{ext}}(r)$ is uniquely determined by the electron density ($\rho(r)$) and, consequently, the Hamiltonian operator and the total energy

are also uniquely determined by the charge density:

$$\rho \rightarrow \upsilon_{\text{ext}} \rightarrow \hat{H} \rightarrow \Psi \tag{6.22}$$

We can define the *energy functional* as:

$$E[\rho] = T[\rho] + V_{en}[\rho] + V_{ee}[\rho] = \int \rho(r)\upsilon(r)dr + F[\rho] \tag{6.23}$$

where

$$V_{en}[\rho] = \int \rho(r)\upsilon_{\text{ext}}(r) \tag{6.24}$$

$$F[\rho] = T[\rho] + V_{ee}[\rho] \tag{6.25}$$

The second theorem extends the variational principle to the *energy functional* $E[\tilde{\rho}]$.

$$E_0 \leq E[\tilde{\rho}] \tag{6.26}$$

where $\tilde{\rho(r)}$ is a trial electron density. Therefore, just like the ground state wave function can be obtained by minimising the energy (Eq. (6.15)) the electron density of the ground state can be obtained by minimising $E[\tilde{\rho}]$.

The key advantage of using the electron density instead of the wave function is that for an N-electrons system only the 3 spatial coordinates of the density are required to calculate the ground state energy whereas in the Hartree-Fock approximation the wave function contains $3N$ variables accounting for the 3 spatial coordinates of each electron.

6.2.7 Kohn-Sham equations

While the concept of obtaining the ground state energy by minimising the energy functional was a considerable step forward over the Hartree-Fock approximations but it still requires drastic assumptions to compute $F[\rho]$.

In 1965, Kohn and Sham [126] proposed to use a *noninteracting reference system* with no electron-electron interactions described by the following Hamiltonian:

$$\hat{H}_s = \sum_i^N (-\frac{1}{2}\nabla_i^2) + \sum_i^N \upsilon_s(r_i) \tag{6.27}$$

For such Hamiltonian the ground state electron density and the associated wave function can be calculated exactly. Then the kinetic energy functional for this noninteracting system can be defined as:

$$T_s[\rho] = \sum_i^N \langle \Psi_s | -\frac{1}{2}\nabla_i^2 | \Psi_s \rangle \tag{6.28}$$

Equation (6.25) can then be reformulated using T_s:

$$\mathrm{F} = T_s[\rho] + J[\rho] + E_{xc}[\rho] \tag{6.29}$$

where $E_{xc}[\rho]$ is called the *exchange-correlation energy* and it combines the nonclassical part of $V_{ee}[\rho]$ and the difference between $T[\rho]$ and $T_s[\rho]$.

We can define an effective potential v_{eff} that adds the coulomb and exchange-correlation

contribution to the original external potential:

$$\begin{aligned} \upsilon_{\text{eff}} &= \upsilon_{\text{ext}}(r) + \frac{\delta J[\rho]}{\delta \rho(r)} + \frac{\delta E_{xc}[\rho]}{\delta \rho(r)} \\ &= \upsilon_{\text{ext}}(r) + \int \frac{\rho(r')}{|r - r'|} dr' + \upsilon_{xc}(r) \end{aligned} \tag{6.30}$$

where υ_{xc} is the *exchange-correlation potential*.

$$\upsilon_{xc}(r) = \frac{\delta E_{xc}[\rho]}{\delta \rho(r)} \tag{6.31}$$

Then, the electron density $\rho(r)$ can be obtained by solving the N one-electron equations:

$$\left[-\frac{1}{2}\nabla^2 + \upsilon_{\text{eff}}(r) \right] \psi_i = \varepsilon_i \psi_i \tag{6.32}$$

where the electron density is constrained by:

$$\rho(r) = \sum_{i}^{N} \sum_{s} |\psi_i(r, s)|^2 \tag{6.33}$$

The set of eigenvalue equations represented in Equation (6.32) are known as the Kohn-Sham equations and can be solved self-consistently.

6.2.8 Exchange-correlation functional

Kohn-Sham equations lead to the exact electron density provided E_{xc} is known. However, the exact form of E_{xc} is not known, hence it must be estimated. An accurate approximation of the E_{xc} functional is crucial to obtain the true ground state of the system and, therefore, it has been an active area of research since the Kohn-Sham method was proposed.

The simplest approximation for the exchange-correlation functional is known as the *local-density approximation* (LDA) and is derived from the homogeneous electron gas (HEG) model which assumes that the electron density is uniformly distributed across the 3D space. The E_{xc} for this and similar approximations is defined as:

$$E_{xc}^{LDA}[\rho] = \int \rho(r)\varepsilon_{xc}(p(r))dr \tag{6.34}$$

where $\varepsilon_{xc}(p)$ refers to the exchange and correlation energy per electron of a uniform electron gas of density ρ. This approximation works well for slowly varying densities but it tends to underestimate ground-state and ionisation energies while overestimating binding energies.[127] Therefore, more complex E_{xc} functionals have been developed. A popular way of improving the local description of the exchange-correlation energy is to incorporate the second-order density gradient expansion while imposing the necessary constraints to correct for the exchange hole violations arising from the expansion.[128]. This approximation is known as the *generalised gradient approximation* (GGA).[129] Additionally, other functionals include the non-interacting kinetic energy to improve accuracy.[130] These are know as meta-GGA functionals. Another popular family of functionals are those that include a portion of the exact exchange energy computed with the Hartree-Fock exchange functional.[131] These are known as *hybrid* functionals and they were implemented in periodic calculations for the first time using the `CRYSTAL` code.[132]

Selecting the appropriate exchange-correlation functional approximation is not a trivial task and will depend on the system under study, the accuracy requirements and the computational resources available.

6.3 Computational methods

All *ab initio* calculations including the geometry optimisation, the total energy calculations and the DFT-PDOS were performed using `CRYSTAL17`, a quantum-mechanical *ab initio* program based on DFT that uses a linear combination of atom-centered Gaussian-type orbitals (the basis set) for the expansion of the crystalline orbitals to carry out periodic solid-state simulations of atomic systems.[133,134]

The Kohn-Sham equations were solved in the unrestricted open shell formalism. A 8-64111d41G quintuple-zeta basis set was used for iron atoms. The oxygen 8-411d11G and carbon 6-311d11G basis sets developed by Valenzano et al.[135] for $CaCO_3$ are used in the current work as some calculations involve carbonate species. A triple-zeta basis set optimised by Peintinger et al.[136] is used for the hydrogen atoms. The details of this basis sets can be found in Appendix A.1. In order to compute the Fermi energy of the system the reciprocal space is sampled according to the Pack-Monkhorst method with a shrinking factor of 8.[137] A second shrinking factor of 16 defines the sampling of k-points for the calculation of the density matrix—the *Gilat* net.[138,139] The truncation criteria for the Coulomb and exchange infinite sums are set to 10^{-8} for the overlap threshold of Coulomb integrals, 10^{-8} for the penetration threshold of the Coulomb integrals, 10^{-8} for the overlap threshold of HF exchange integral and 10^{-16} for the HF pseudo-overlap. The SCF method is used until a convergence of $\Delta E = 10^{-7}$ is achieved.

6.4 Iron bulk and surface properties: a comparative study

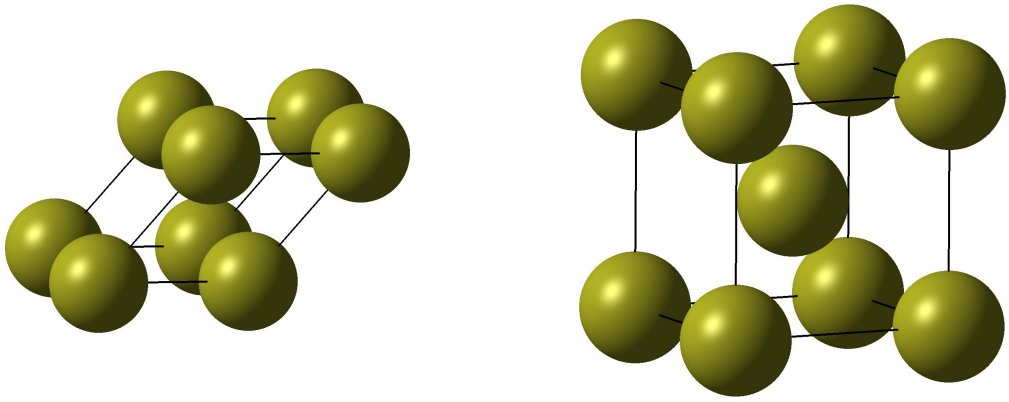
Transition metals have been widely used and studied for many years due to their industrial importance. Metal catalysts play a key role in common chemical reactions such as the Fischer-Tropsch and the Haber process.[140,141] Moreover, iron based alloys are used extensively in the oil and gas industry where the chemical and physical processes occurring on the metal surface, such as corrosion and wear, need to be well understood in order to overcome the major challenges that this industry faces. Due to its relevance in industry, the surface chemistry in metals has been an active field for decades and with the addition of new experimental and computational tools many studies brought unique insights into the surface chemistry at the atomic level.[142–144] In particular, Density Functional Theory (DFT) has been instrumental to understand the adsorption and reaction of different chemical species on the metal surface and has aided the interpretation of complex experimental results.[145,146]

The pipes used to transport oil and gas are typically made from steel, an alloy made up of iron with a small percentage of carbon (up to 2%). To analyse these complex surfaces highly simplified models are adopted. To that end, steel surfaces are typically modelled as a pure iron surfaces in DFT computations.

At the typical temperatures and pressures found in the oil and gas industry the iron is found in the alpha phase, a body-centred cubic (BCC) crystalline structure. The iron surface chemistry has been studied for decades due to its industrial relevance. The most thermodynamically stable surfaces are generally those with a lower miller index as they tend to be closer packed and exhibit a higher adsorption energy. Therefore, the (100), (110) and (111) iron facets have been studied extensively to investigate the adsorption of small

molecules.[147–152]

α-Fe has a conventional cell lattice constant of 2.8606 Å at 0 K and 2.8662 Å at 295 K.[153,154] Figure 6.1 shows the primitive and conventional cell of the BCC crystal structure of α-Fe.



(a) α-Fe primitive cell (b) α-Fe conventional cell

Figure 6.1: α-Fe body-centered cubic crystal structure

DFT methods can be used to investigate both bulk and surface properties of iron. However, DFT should be used with care as the use of different DFT approximations can have a significant impact on the results and could even lead to the wrong conclusions in some cases.[155,156] Generalized gradient approximation (GGA) functionals have found much success at describing metallic systems but adsorption calculations are limited by their semi-local approximation of the exchange-correlation (XC) functional and the associated self-interaction error. On the other hand, hybrid functionals tend to predict the adsorption site preference more reliably partly due to the inclusion of a portion of the Hartree-Fock exchange into the functional.[157,158]. However, hybrid functionals are typically more computationally expensive than GGA functionals and some do not fulfil the homogeneous electron gas limit leading to suboptimal results in metallic systems.[159]

Therefore, the choice of density functional is not straightforward in systems involving

metallic surfaces with adsorbed molecules. In such systems, an initial validation with experimental surface data should be carried out to ensure that the DFT method used is adequate and can reliably model the interaction between the adsorbed molecules and the surface. Such validation can come from a range of experimental techniques such as STM, XPS, LEEDS, IR, etc., which allow to compare, for example, the most stable adsorption site, the density of states (DOS) at the valence band or the vibrational frequencies in an IR or Raman spectra. This kind of validations are often lacking in surface calculations and rarely more than one functional is used for all the calculations to compare the results. This not only diminishes the reliability of the results but it also may lead to the selection of a sub-optimal density functional or basis set.

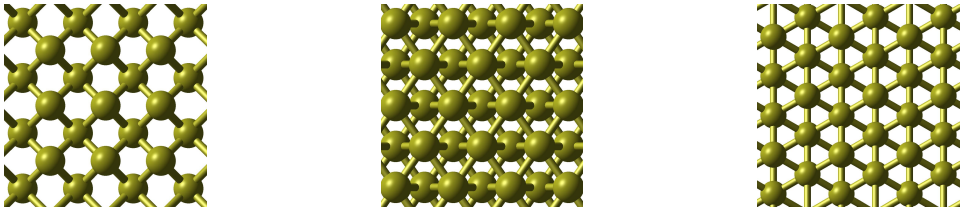
The aim of this work is to study the adsorption of small molecules, thus four different functionals are compared with experimental data in order to select the most adequate for this work. Two Generalised Gradient Approximation (GGA)—PBE and PBEsol—and two hybrid functionals—B3LYP and HSE06.

Firstly, the lattice parameter, magnetic moment and bulk modulus of bulk iron are compared to the corresponding experimental values in Table 6.1. The lattice parameter and bulk modulus of α-Fe obtained using hybrid functionals are closer to the experimental value than those obtained using GGA functionals. On the other hand, the experimental magnetic moment is more accurately represented by the GGA functionals.

Low Miller indices generally correspond to closer packed surfaces. Closely packed surfaces typically exhibit a lower surface energy, and consequently those surfaces are more stable and predominant.[160] Figure 6.2 shows the three lowest Miller index surfaces of α-Fe: (100), (110) and (111).

Table 6.1: Iron bulk properties

Functional	**Lattice parameter (Å)**	**Magnetic moment (μ_B/atom)**	**Bulk modulus (GPa)**
Experimental	2.8639	2.22	168
PBE	2.8136	2.15	236
PBEsol	2.7769	2.09	257
B3LYP	2.8928	2.74	200
HSE06	2.8691	2.81	218



(a) Fe(100) (b) Fe(110) (c) Fe(111)

Figure 6.2: Top view of the Fe(100), Fe(110) and Fe(111) facets.

The surface energy of a facet can be calculated from the total energy of the bulk (E_{bulk}) and the total energy of a slab of the corresponding facet (E_{slab}) as follows:[161]

$$E_{\text{surf}} = \frac{1}{2A}(E_{\text{slab}} - nE_{\text{bulk}}) \tag{6.35}$$

where E_{bulk} and E_{slab} and are the total energy per unit cell at the bulk and of a n-layer slab respectively. However, E_{surf} generally diverges linearly with n when using this method as noted by Boettger[161]. A way to mitigate this is to calculate the E_{bulk} from two slabs with different thicknesses to get the total energy required to create additional bulk-like unit cells at the centre of the slab. Then the surface energy can be calculated as

$$E_{\text{surf}} = \frac{1}{2A}\left(E^B_{\text{slab}} - \frac{N^B_{\text{slab}}}{N^B_{\text{slab}} - N^A_{\text{slab}}}(E^B_{\text{slab}} - E^A_{\text{slab}})\right) \tag{6.36}$$

where A and B denote two different slabs with unit cell thicknesses N^A_{slab} and N^B_{slab} respectively and where $N^A_{\text{slab}} < N^B_{\text{slab}}$.

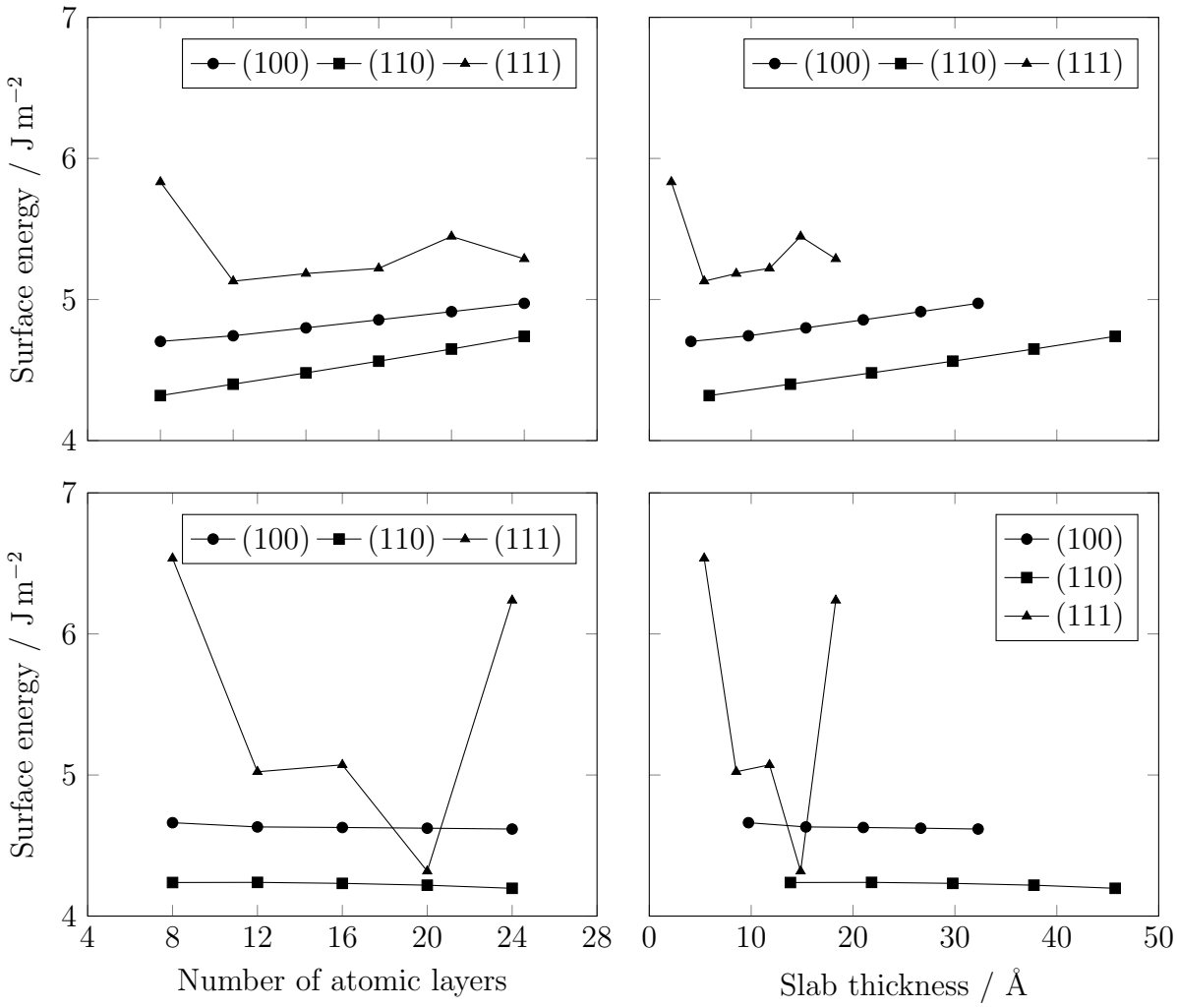


Figure 6.3: α-Fe surface energy of (100), (110) and (111) facets as a function of the atomic layers of the slab

Figure 6.3 shows the surface energy for the (100), (110) and (111) facets calculated using Eqs. (6.35) and (6.36) is shown as a function of the number of atomic layers and slab thickness. The surface energy calculations carried out using Eq. (6.35) exhibit the aforementioned linear divergence and therefore this method is not adequate to calculated the surface energy of these facets. On the other hand, the surface energy calculation method using Eq. (6.36) produces noticeably more stable surface energies even at small slab thicknesses. However, the (111) facet exhibits less stable surface energies which could be related to its smaller surface

density. The large differences in surface energy for the (111) facet could indicate that the geometry optimisation reached a local minimum rather than the global minimum for some of the calculations.

Table 6.2 displays the calculated surface energy for (100), (110) and (111) α-Fe surfaces using the PBE functional. density and energy of these three α-Fe facets. Fe(110) is the most closely packed and low energy surface of the three followed by Fe(100) and Fe(111). The correlation between surface density and surface energy is in line with the aforementioned general trend: the higher the packing efficiency the lower the surface energy. Since Fe(110) is the most stable and predominant facet of α-Fe it has been studied by a large body of literature.

Table 6.2: Surface density and energy of iron facets

Facet	**Surface density** / atom/Å^2	**Surface energy** / atom/Å^2
(100)	0.122	4.617
(110)	0.172	4.197
(111)	0.073	6.238

To assess the suitability of the candidate functionals from Table 6.1 the IR spectrum of a small molecule adsorbed on the iron surface can be calculated and compared to experimental measurements. The CO molecule was chosen as the adsorbate due to its simplicity, availability of experimental literature and its composition similarity to carbonate species.[2,162] Moreover, CO is the by-product of CO_2 activation on an iron surface which is a common process in many applications involving corrosion and catalysis.[163]

Erley[2] measured the infrared spectrum of CO chemisorbed on Fe(110) at different exposures and identified two different CO adlayer structures: p(2x4) (0.25 ML) at low exposures and

distorted p(1x2) (0.5 ML) at high exposures. They propose that the CO molecule adsorbs vertically on the "on top" high symmetry site (see Fig. 6.4 for a top view image of the Fe(110) high symmetry sites) with the carbon atom closest to the iron surface. The measured vibrational spectrum revealed a wide peak around 450 cm^{-1} associated to the Fe-C stretching and a narrower peak around 1900 cm^{-1} corresponding to the stretching of the C-O bond. The frequency of the C-O peak shifts towards higher frequencies with more exposure. Erley [2] proposed the top site as the most likely adsorption site for the CO molecule. The proposed Fe(110)/CO structures were replicated and the geometries were optimized using DFT methods. The optimised geometry was similar amongst all functionals for both adlayers; Fig. 6.5 shows the optimised geometry for the PBE functional.

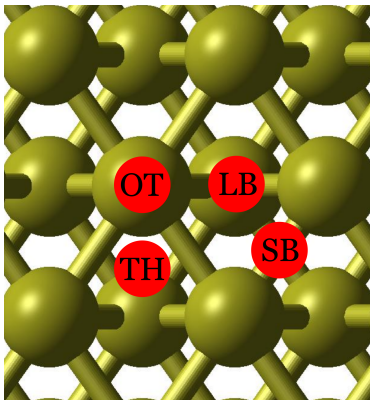
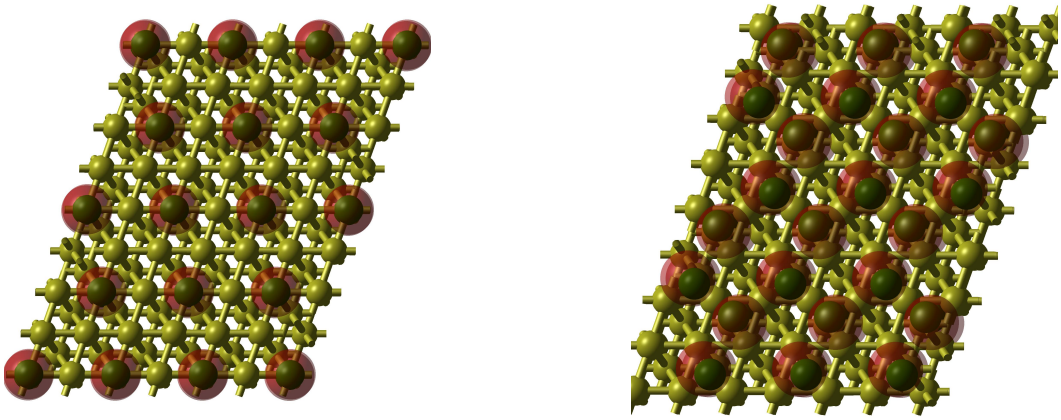


Figure 6.4: Top view of the Fe(111) highlighting the high symmetry sites: on-top (OT), long-bridge (LB), short-bridge (SB) and, 3-fold hollow (TH).

The IR vibrational frequencies associated with the C-O bond are shown in Table 6.3 where they are compared to those obtained by DFT methods using PBE, PBEsol, B3LYP and HSE06 functionals. The theoretical frequencies obtained for the 0.25 ML adlayer structure are lower than the experimental ones regardless of the functional used with the HSE06 functional being the closest to the frequencies obtained experimentally. On the other hand, the 0.5 ML adlayer had frequencies much closer to the experimental measurements.

One aspect that should not be neglected when choosing a functional is its associated



(a) CO/Fe(110) 0.25 ML (b) CO/Fe(110) 0.5 ML

Figure 6.5: Geometry optimised atomistic models of the adlayer structures identified by Erley[2] using the PBE functional.

Table 6.3: CO/Fe(110) high frequency peak

Functional	**0.25 ML** / cm^{-1}	**0.5 ML** / cm^{-1}
Experimental	1952-1985	1890-1948
PBE	1725-1815	1879-1932
PBEsol	1747-1843	1907-1960
B3LYP	1755-1875	1894-1955
HSE06	1779-1893	1927-1987

computational cost. Generally, as the complexity of the functional increases so does the accuracy of the results. However, the increase in accuracy usually comes at the expense of a higher computational cost. Table 6.4 shows the time it took for the CPU to complete the initial self-consistent field (SCF) calculation of the p(2x4) (0.25 ML) adlayer structure. GGA functionals take significantly less time to complete the SCF calculation compared to the hybrid functionals. This is likely due to the additional Hartree-Fock calculation included in the hybrid functionals in order to improve the description of the exchange energy. The computational cost becomes increasingly important as the number of simulations required increases.

Table 6.4: Computation time difference between exchange-correlation functionals

Functional	**CPU time / s**
PBE	2289.37
PBEsol	3602.21
B3LYP	9537.85
HSE06	11 047.63

One can choose a suitable functional for their particular use case by comparing the bulk properties and CO surface adsorption frequencies with the corresponding experimental measurements and accounting for the computational cost of each functional. The PBE functional was considered the most adequate for the following iron surface calculations as the improvements of hybrid functionals over PBE were not considered to be large enough to warrant the additional computational cost.

6.5 Oxygen adsorption on Fe(110)

Iron-oxides are not only important in many corrosion environments but are also used in numerous applications due to their magnetoelectronic and catalytic properties. In CO_2 corrosion Fe_3O_4 and FeO constitute a considerable portion of the corrosion scale composition formed as a by-product of the CO_2 corrosion process.[164,165] The formation of iron-oxides from pure iron is initiated by the adsorption of oxygen on the iron surface.[152] Therefore, this adsorption process has been studied extensively both experimentally and theoretically.[150,151,166–169]

Oxygen adsorption on Fe(110)—the most stable Fe surface—was originally believed to take place in the long-bridge site, a view supported by both experimental and theoretical

studies.[147,168,168,170] The adsorption energy measures the energy released upon the adsorption of a chemical species onto a specific site of a surface and is a key metric used to determine theoretically the most likely adsorption site for a particular adsorbate; higher adsorption energy typically corresponds to a more thermodynamically favoured site for the adsorbate to bind to. Recently, some theoretical studies reported a larger adsorption energy on the three-fold hollow site compared to the long bridge site at high coverages and similar adsorption energies at low coverages.[152,171]

To investigate these discrepancies the adsorption of oxygen was modelled on a symmetric slab using DFT methods. The slab must be thick enough to avoid interactions between both surfaces of the slab. In order to decide what slab thickness is adequate for the purposes of determining the adsorption energy of oxygen it is instructive to analyse how the adsorption energy and the distance between atomic layers change as a function of the thickness of the slab. To this end, the geometry of a series of Fe(110) p(1x1) symmetric slabs of different thicknesses was optimised with one oxygen atom adsorbed at both sides of the slab for all the high symmetry sites. The adsorption energy of adsorbed oxygen atoms can be calculated as:

$$E_{\mathrm{ads}}^{\mathrm{O/Fe}} = -\frac{1}{N_{\mathrm{O}}}\big(E(\mathrm{O/Fe}) - E(\mathrm{Fe}) - \frac{N}{2}E(\mathrm{O_2})\big) \tag{6.37}$$

where N is the number of oxygen atoms in the supercell, $E_{\mathrm{slab}}^{\mathrm{O/Fe}}$ is the total energy of the optimised geometry of the slab with the adsorbed oxygen atoms, $E_{\mathrm{slab}}^{\mathrm{Fe}}$ is the total energy of the optimised geometry of the clean slab and $E^{\mathrm{O_2}}$ is the total energy of the optimised geometry of the O_2 molecule. The adsorption energy calculated in Eq. (6.37) represents the energy difference between an oxygen atom in molecular form and the oxygen atom adsorbed on the iron surface. A positive E_{ads} indicates that the adsorbate is stable on the surface of the slab.

In addition, since Atomic Orbitals (AO) basis sets are being used to describe the electron density we need to account for the basis set superposition error (BSSE). This type of error arises when comparing the total energies of isolated and combined systems. For example, in the combined O/Fe(110) system described in the current work the slab can improve its electron density description thanks to the additional AO provided by the oxygen and vice-versa. Since this additional description of the electron density is not present in the isolated calculations of the Fe(110) slab and the oxygen molecule the shared atomic orbitals in the combined system can lead to BSSE when calculating adsorption energies.[172] Boys and Bernardi[173] proposed a method to correct for BSSE by calculating the error for each component and subtracting it from the energy in the combined system. The error for each component can be calculated as:

$$E_{BSSE}(\mathrm{Fe}) = E^{\mathrm{O/Fe}}_{\mathrm{O/Fe}}(\mathrm{Fe}) - E^{\mathrm{Fe}}_{\mathrm{O/Fe}}(\mathrm{Fe}) \tag{6.38}$$

$$E_{BSSE}(\mathrm{O}) = E^{\mathrm{O/Fe}}_{\mathrm{O/Fe}}(\mathrm{O}) - E^{\mathrm{O}}_{\mathrm{O/Fe}}(\mathrm{O}) \tag{6.39}$$

$$\tag{6.40}$$

where the subscript represents the geometry of the calculation, the superscript represents the basis set used and the symbol in parenthesis is the chemical system for which the total energy is calculated. For example, $E^{\mathrm{O/Fe}}_{\mathrm{O/Fe}}(\mathrm{Fe})$ is the total energy of an iron slab with the optimised geometry of a O/Fe system and with all the basis sets used to optimise the O/Fe system. With the BSSE errors calculated the adsorption energy can now be estimated as:

$$E^{\mathrm{O/Fe}}_{\mathrm{ads}} = -\left(E^{\mathrm{O/Fe}}_{\mathrm{O/Fe}}(\mathrm{O/Fe}) - E^{\mathrm{Fe}}_{\mathrm{Fe}}(\mathrm{Fe}) - E^{\mathrm{O}}_{\mathrm{O}}(\mathrm{O}) - E_{BSSE}(\mathrm{Fe}) - E_{BSSE}(\mathrm{O})\right) \tag{6.41}$$

Table 6.5 shows the adsorption energy of oxygen onto a Fe(110) slab for different thicknesses and adsorption sites. The three central layers where fixed at their bulk positions to mimic the bulk of the material at the centre of the slab. The adsorption energy does not change

significantly as the thickness increases. At 5 atomic layers the threefold hollow, long bridge and short bridge sites have a slightly higher adsorption energy compared to the rest of the thicknesses tested.

Table 6.5: Adsorption energy in $\mathrm{J\,m^{-2}}$ of oxygen adsorbed onto Fe(110) p(1x1) symmetric slabs for different thicknesses (atomic layers) and different adsorption sites

Atomic layers	**Top**	**Threefold hollow**	**Long bridge**	**Short bridge**
5	1.33582	2.86649	2.03383	2.12422
7	1.33552	2.86506	2.03097	2.12244
9	1.33593	2.86555	2.03109	2.12271
11	1.33690	2.86538	2.03105	2.12273
13	1.33558	2.86564	2.02977	2.12276

The distance between atomic layers of the slab can be expressed relative to the distance between atomic layers at the bulk for the same crystallographic direction:

$$\Delta_{i,j} = (d_{i,j} - d_{\mathrm{bulk}})/d_{\mathrm{bulk}} \tag{6.42}$$

where $d_{i,j}$ is the distance between the atomic layer i and j. Atomic layer 1 is taken as the outermost layer of the slab so that $d_{1,2}$ is the distance between the first and second outermost layers of the slab. d_{bulk} is the distance between two consecutive atomic layers on the same crystallographic direction as the slab surface.

Figure 6.6 displays the distances between atomic layers 1, 2, 3 and 4 as a percentage of the distance at the bulk for a clean Fe(110) surface and for oxygen adsorbed on the high symmetry sites of the Fe(110) surface. The distance between the first and second layer exhibits the largest deviations from the bulk distance ranging from 1 to 4%. The sites furthest away from the surface—on-top and short bridge—have smaller deviations from the bulk compared to the sites closest to the surface—threefold hollow and long-bridge—where the deviation of the

long bridge adsorption site is considerably larger than the rest. The clean surface deviation is similar to that of the threefold hollow adsorption site. Interestingly, the deviations with a slab of 5 atomic layers, which has all but the surface layer fixed, are not significantly different than those of thicker slabs indicating that only the outermost layer of the slab experience a meaningful relaxation for both the clean Fe(110) surface and when oxygen is adsorbed. Indeed, the distances between the second and third, and third and forth atomic layers deviate less than 0.5% from the bulk.

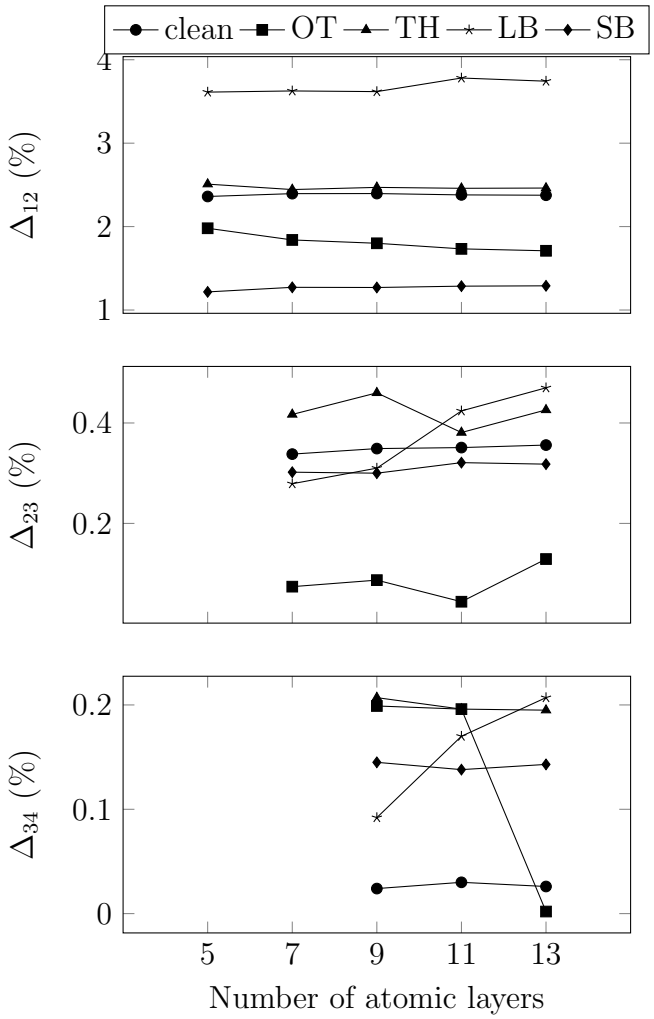


Figure 6.6: Distances between the four outermost atomic layers of a Fe(110) p(1x1) slab for the four high symmetry sites: on-top (T), long-bridge (LB), short-bridge (SB) and, 3-fold hollow (TH). The distances are expressed relative to the distances at the bulk.

These results suggest that (I) fixing all the layers of the slab to their respective bulk positions except for the surface layer accounts for most of the slab relaxation (II) a 5-layer slab is thick enough to obtain adsorption energies with reasonable accuracy. Therefore, a 5-layer slab with the three central layers fixed to their respective bulk positions appears to be the most cost-efficient approach to model adsorption on the Fe(110) surface and it is used in the following oxygen adsorption analysis.

The adsorption energy of oxygen on Fe(110) was calculated for a p(1x1), p(2x2), p(3x3), p(4x4) and p(5x5) slab to understand the role of the interaction between neighbouring adsorbates on the adsorption stability. Figure 6.7 shows the adsorption energy as a function of the distance between two neighbouring oxygens and the oxygen coverage of the iron surface. The surface coverage is defined in terms of the ratio between the number of atoms at the surface and the number of adsorbate atoms (ML). The on-top site least stable site across the range of coverage tested in this work. This is likely due to the large distance of the oxygen to the surface and the single neighbouring iron atom underneath the adsorbate leading to low coordination with the surface. At 1 ML the long bridge and short bridge sites have similar adsorption energies whilst the threefold hollow site is the most stable of the four at this coverage. At 0.25 ML all sites exhibit a higher adsorption energy due to the weaker repulsive interaction between the adatoms. However, the long bridge site is now similar in energy to the threefold hollow site instead of the lower adsorption energy short bridge site. Therefore, at 0.25 ML the long bridge and threefold hollow site are the most thermodynamically stable. These results are in good agreement with the latest theoretical O/Fe(110) adsorption studies and support the hypothesis that the threefold hollow site is more thermodynamically stable at very high coverages.[152,171] Identifying the adsorption site at high coverage is of great importance to facilitate the discovery of new intermediate structures between the adsorption of oxygen and a fully formed iron oxide layer. For coverages lower than 0.25 ML we see no

difference in the adsorption energy for the long bridge and threefold hollow sites indicating that the oxygen atoms no longer experience the repulsive interactions of their neighbouring adatoms. Indeed, it is the repulsive interactions amongst adatoms that decreases the binding of oxygen atoms to the surface on long bridge sites more than on threefold hollow sites.

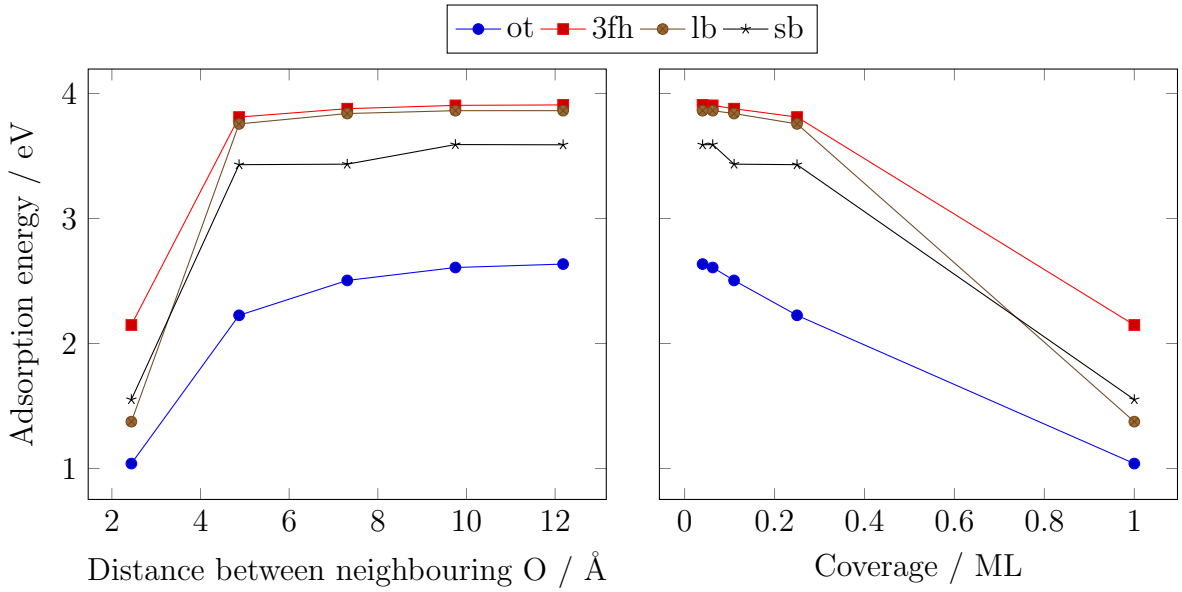


Figure 6.7: Distances between the four outermost atomic layers of a Fe(110) p(1x1) slab. The distances are expressed relative to the distances at the bulk.

6.6 O/Fe(110) XPS analysis

To understand the corrosion process it is crucial to identify not only the composition but also the chemical state of species on the corroding surface. X-ray photoelectron spectroscopy (XPS) is a non-destructive surface analysis technique that can be used to obtain the composition and chemical state of the first few atomic layers of the surface by radiating X-rays of constant frequency over the surface and measuring the kinetic energy of photoelectrons generated by

the photoelectric effect. The kinetic energy of the electrons can be expressed as:

$$E_k = h\nu - E_b - \varphi \tag{6.43}$$

where E_k is the kinetic energy of the photoelectron, $h\nu$ is the energy of the photon, E_b is the binding energy of the electron and φ is the work function of the surface—the energy difference between the vacuum and the Fermi level of the metal surface. The spectrum of binding energies obtained from an XPS measurement consists of peaks representing molecular orbitals of the chemical species present in the surface. Often these peaks are composed of overlapping peaks which complicate the analysis of the data. This is often resolved by fitting the multi-peak to a function with multiple peak components. The choice of fitting function and the number of overlapping peaks can affect the interpretation of the data so a theoretical analysis of the chemical system under study can provide key insights to chose an adequate fitting function.[174]

Asymmetric peaks are not uncommon in XPS spectra and it is not always trivial to determine whether they should be treated as a multi-component peak or a single asymmetric peak.[3] The origin of the shape of XPS peaks is key to interpret the chemical system under study; therefore, theoretical investigations have been carried out to support the interpretation of odd shaped peaks. For example, asymmetric peaks in conducting surfaces are known to appear due to the creation of low energy electron-hole pairs near the Fermi level.[175] Asymmetric peaks can also be observed for adsorbate atoms on conducting surfaces.[151,176–181] Tillborg et al.[182] proposed that the asymmetry of the adsorbate XPS peaks arise from the hybridisation of the adsorbate orbitals with the surface atoms. When the resulting hybrid orbital spans over the Fermi energy, and hence is partially filled, the low energy electron-hole pairs can still form on these hybrid orbitals. However, if the resulting hybrid orbital is completely full, i.e. its energy is lower than the Fermi energy, then no additional electron-hole

pairs can be created resulting in a symmetric peak.[182] This explanation for asymmetric peaks of adsorbates on conducting surfaces implies that one can validate the choice of fitting function by analysing the electronic structure of the surface using either theoretical or experimental techniques. This type of validation is still rare in XPS experiments which can lead to independent studies fitting a different line shape for similar chemical systems.[177,183]

Oxygen adsorption on iron is the first step in the formation of iron oxides. The atomic oxygen can originate from different sources so it is instructive to analyse the dissociative adsorption of oxygen from common small molecules using XPS. The XPS spectra of Fe(110) exposed to O_2, H_2O and CO_2 is shown in Fig. 6.8 for Fe 2p and O 1s orbitals.[3] As expected, the Fe 2p orbitals present an asymmetric shape in the XPS spectra with a very similar spectra across all molecules tested. Furthermore, the O 1s orbital also produces an asymmetric peak regardless of the molecule exposed to the Fe(110) surface. The asymmetric O 1s peak has also been reported by other studies exposing the Fe(110) surface to O_2.[151,184]

The O 1s asymmetric peak can have two different interpretations: (I) multiple overlapping symmetric peaks corresponding to different adsorbate states or (II) a single asymmetric peak as a result of hybrid states near the Fermi level as reported by Tillborg et al.[182]. To determine the origin of the asymmetric peak DFT Projected Density of States (PDOS) calculations were carried out for a (2 x 2) 5-layer Fe(110) symmetric slab with an oxygen atom adsorbed on the threefold hollow site—the most stable site according to the present work (Fig. 6.9). The PDOS reveals hybridised states of the O 1s and the surface layer Fe 2d orbitals around the Fermi level. According to Tillborg et al.[182] this results in an asymmetric O 1s peak in the XPS spectrum. Therefore, asymmetric peak the observed in Fig. 6.8 can be attributed to the hybrid states around the Fermi energy and an asymmetric line shape function (e.g. Lorentzian-based asymmetric functions) must be used to fit the peak.

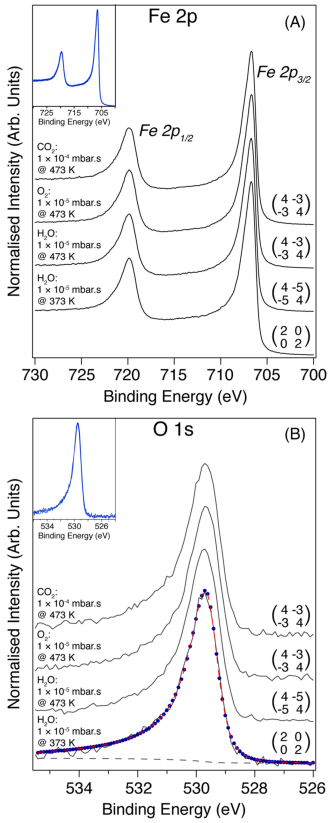


Figure 6.8: (A) Fe 2p and (B) O 1s X-ray photoelectron spectroscopy (XPS) spectra ($h\nu$ = 1486.6 eV, θ E = 0) acquired from four ordered phases formed on Fe(110) following exposure to either O2, CO2, or H2O. Details of exposure (in mbar/s), substrate temperature (in K), and the resulting surface unit cells (matrix notation) are indicated. Each spectrum has been normalised to have a maximum (minimum) intensity of 1 (0). Insets (top left of each panel) show superimposition of spectra displayed in panel. Also shown is the best fit (blue markers) to the bottommost O 1s spectrum, using an LF line shape function (broken red lines) and a Shirley-type background. Source: Acres et al.[3]. Figure reproduced with permission of the rights holder, John Wiley & Sons.

DFT-PDOS calculations provide a simple method to verify the type of line shape that is appropriate for a given surface.

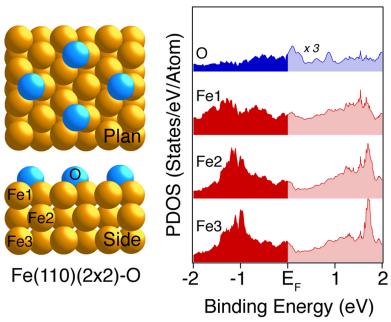


Figure 6.9: To the left, schematic plan and side views of Fe(110) (2 x 2)-O structure used to generate DFT-PDOS.The O atoms are located in their most energetically favourable adsorption sites, as determined from DFT modelling. Atom labels are employed to identify the source of plotted DFT-PDOS. To the right O, Fe1, Fe2 and Fe3 DFT-PDOS ($-2eV \geq E_F \geq 2eV$) from an optimised five-layer Fe(110) (2 x 2)-O slab. DFT, density functional; PDOS, projected electronic density of states. Source: Acres et al.[3]. Figure reproduced with permission of the rights holder, John Wiley & Sons.

6.7 H_2CO_3/Fe(110) adsorption geometry

Direct H_2CO_3 reduction has been studied extensively in CO_2 corrosion as it was thought to be the origin of the additional corrosion current density obtained under CO_2 environments compared to CO_2-free environments.[31,185,186] The carbonic acid still plays a major role in CO_2 corrosion so it is important to understand its interaction with the reactive surface. To that end, a H_2CO_3 molecule is adsorbed at each side of a symmetric (2 x 2) Fe(110) 5-layer slab. The H_2CO_3 molecule and the outermost layer of the slab was allowed to relax and geometry optimisation was performed using different starting geometries for the H_2CO_3 molecule. Three different configurations were obtained (Fig. 6.10). In all three configurations the carbonic acid molecule dissociates into two H^+, a O^{2-} and a CO_2 molecule. The H^+ and the O^{2-} ions adsorb at the threefold hollow site—the most stable site for oxygen to adsorb as shown in Fig. 6.7. In the first two configurations the oxygens of the CO_2 molecule are located at the on-top site of the Fe(110) surface and the C-O bond exhibits a length of 125.4 pm, higher than the 116.3 pm bond length measured in the gas phase.[187] On the other hand, the third

optimised geometry displays a more asymmetric configuration where one of the oxygens is at the on-top site while the other is at the short bridge site. This asymmetric configuration results in asymmetric C-O bond lengths of 124.9 pm for the on-top oxygen and 129.0 pm for the short-bridge oxygen.

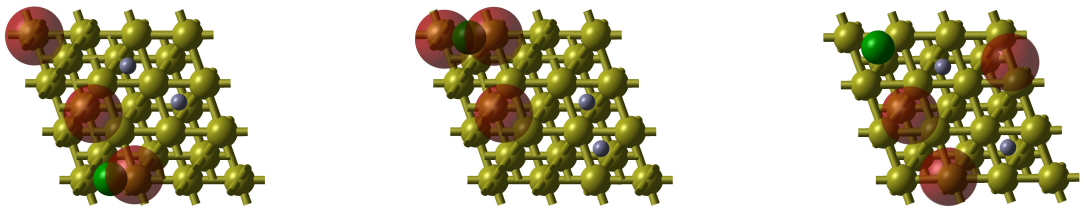


Figure 6.10: Top view of the Fe(100), Fe(110) and Fe(111) facets.

Since no stable geometry with the full H_2CO_3 molecule could be found it is likely that the dissociation of H_2CO_3 is a thermodynamically favourable process. This dissociation could constitute an additional pathway for the transport of H^+ to the reactive steel surface and is compatible with the established consensus that the reduction of H_2CO_3 is not responsible for the increase in corrosion rate under CO_2 environments. Nevertheless, a more in-depth study is necessary to understand the conditions under which this dissociation reaction takes place.

6.8 Conclusions

The application of DFT methods to model CO_2 corrosion is still lacking. In order to obtain reliable results from DFT calculations it is important to select a density functional that is adequate for the chemical system under study. In this chapter, four different density functionals were investigated in Sections 6.4 and 6.5 comparing both bulk and surface properties with experimental data to determine the most adequate functional to be used in the iron surface

chemistry calculations. The PBE functional was considered to be accurate enough for the following surface chemistry calculations.

DFT calculations can also help with the interpretation of XPS spectra by computing the electronic structure of the surface under study. In Section 6.6 the asymmetric peak observed in the O-Fe110 spectra was found to originate from the partially filled hybridised orbital around the Fermi energy by calculating the PDOS using DFT methods.

Lastly, the adsorption of carbonic acid onto Fe(110) was investigated by optimising the geometry of a Fe(110) surface with a H_2CO_3 molecule on the surface. The geometry optimisation performed using DFT resulted in the dissociation of H_2CO_3 into H^+, O^{2-} and CO_2 on the iron surface. This dissociation on the iron surface could further contribute to the *buffering* effect driving the HER reaction although further research is necessary.

Chapter 7

Conclusions

Corrosion is an ubiquitous problem in many industries costing $2.5 trillion yearly. A large portion of the cost is spent on methods and strategies to prevent or mitigate the corrosion process. Therefore, there is a considerable financial incentive to develop new cost-effective prevention and mitigation strategies.

In the oil and gas industry corrosion is not only a financial risk but also and environmental one. The pipes used to extract the oil and gas are susceptible to both external (outer surface) and internal (inner surface) corrosion so they require regular inspections and adequate maintenance to safely extend their lifespan. Internal corrosion is generally more aggressive and dangerous than external corrosion due to the highly corrosive environment inside the pipeline. A key component from such environments is the CO_2 gas extracted alongside the oil and water. The CO_2 gas dissolves into solution and hydrates to form carbonic acid. The corrosion reaction is limited by the supply of protons to the reactive surface where the cathodic HER takes place. The carbonic acid boosts the HER by acting as an additional source of

protons, the so-called buffering effect. This type of corrosion is known as CO_2 corrosion.

A key feature of CO_2 corrosion is that under certain conditions corrosion product may precipitate on the metal surface forming a film that can protect the steel from further corrosion. This phenomenon has been studied for decades due to its potential to become a cost-effective corrosion mitigation strategy. However, the formation process of these films is still not fully understood and their long term stability is still uncertain due to the difficulty of running reproducible experiments under field conditions. However, CO_2 corrosion models can in principle simulate long term experiments in complex environments as long as they are appropriately calibrated. Generally, CO_2 corrosion models are 1-dimensional electrochemical models of general (or uniform) corrosion where only a few of them incorporate some description of the corrosion product film. In this work a novel hybrid model combining an electrochemical CO_2 general corrosion model with a stochastic 3-dimensional model was presented, the Semi-local Corrosion Approximation (SLCA). The goal of this model is to capture the stochastic nature of the corrosion process which is generally missing in CO_2 general corrosion models. The model was then validated against experimental data and a series of model predictions at different conditions were analysed and compared against our current understanding of the CO_2 corrosion process. The model results revealed that the formation process of the corrosion scale plays an important role on the stability and protection capabilities of the scale once fully formed. If the film forms too slowly it will become thick and porous whereas a rapidly formed film can result in an incomplete formation of the film which can lead to localised corrosion. This level of insight was only possible due to the explicit 3-dimensional description of the corrosion scale.

CO_2 corrosion trends are generally based on experiments that only change a single environment variable. The applicability of these trends is then limited to the conditions of

the experiment, hence they are not guaranteed to hold true under a different set of conditions. To better understand the relationships between the different environment parameters and to be able to provide general trends with a wide range of applicability a multivariate analysis of the temperature, total pressure and bulk pH was carried out using the SLCA model. One of the key findings of this analysis is that there exist a band in the parameter space that covers the conditions at which a protective film will form and separates the sets of conditions where a porous thick scale forms from those where the scale forms too fast to fully cover the steel surface. More generally, this analysis suggests that one can optimise the environment parameters to form a scale with excellent protective properties.

The SLCA model was adapted to two additional use cases. Firstly, the change of environment after the formation of a protective scale was investigated. It was found that while temperature and pressure changes have a significant effect on the scale stability the scale is not significantly affected by changes in temperature. Secondly, an inhibitor model was incorporated into the SLCA model to describe the protection mechanism of an inhibitor that physically blocks active corrosion sites. The inhibitor was found to not only lower the corrosion rate but also significantly improve the formation of the corrosion scale.

Density Functional Theory has been instrumental to improve our understanding of corrosion at the fundamental level and to support the interpretation of experimental data. This work sets the foundations for future CO_2 corrosion DFT studies by calculating the bulk and surface properties of iron for four popular functionals and compares the results with their respective experimental measurements. The adsorption of oxygen was investigated using the iron Fe(110) surface as a simplified model for the carbon steel surface. The most stable adsorption site was found to be dependent on the surface coverage. At low coverage the three-fold hollow and long bridge sites were the most stable exhibiting similar adsorption energies whereas at 1

ML coverage the three-fold hollow site was found to be the most stable. The XPS spectrum of oxygen adsorbed on iron displays an asymmetric peak for the O 1s orbital. The PDOS of the adsorbed oxygen atoms was calculated to elucidate the origin of the asymmetric peak. It was found that the asymmetry originated from the hybridisation of the O 1s orbitals with the Fe 2p orbitals of the outer atomic layer. The hybrid orbital is positioned around the Fermi level, hence the orbital is expected to be half empty which causes the asymmetry in the peak. Lastly, the adsorption of a carbonic acid molecule on a Fe(110) surface was investigated to understand its interaction with the reactive surface in CO_2 corrosion. The molecule was found to be unstable on the surface with a tendency to dissociate into H^+, O^{2-} and CO_2.

Recommendation for further work

The Semi-local Corrosion Approximation model presented in this thesis represents one of the first steps towards a new class of corrosion models that combine a deterministic model with a stochastic component. The current implementation of the model utilises a relatively simple electrochemical model to ensure that simulations run in a reasonable amount of time. However, more complex general corrosion continuous models have been developed which could in principle be adapted to replace the current electrochemical model. Additionally, this model can be applied to a variety of corrosion systems unrelated to CO_2 corrosion where some type of passivating film forms on the metallic surface.

DFT has the potential to further improve the model by incorporating results from atomistic simulations into the model. However, the present work has focused on the early stages of the corrosion process and no results have been directly implemented into the model yet. Therefore, further DFT studies targeted to improve the model could be carried out in the future. This

could include surface energy studies to understand what crystals form under what conditions and adsorption studies of different inhibitors on a steel surface. Additionally, some of the most inaccurate reaction kinetics models could be studied using Molecular Dynamics.

So far the pipeline system that the model simulates is a closed-loop system where the solution is recirculated through the system. While this is adequate to compare with experimental measurements it doesn't replicate the set up one would find in the field, i.e. non recirculating water flow. Therefore, one could extend the model to cover the case where the solution does not circulate back through the same part of the pipe.

Lastly, in the field the environment inside the pipeline is dynamic. In the current state the model can account for sudden changes in the environment. However, it cannot handle constant change in the environment, e.g. changes in temperature, pressure, salt content, etc; a common problem encountered in the industry.

Appendix A

Atomistic scale corrosion modelling

A.1 basis sets

A.1.1 Iron 8-64111d41G

```
26 8
0 0 8 2.0 1.0
315379.0    0.000227
45690.0     0.0019
9677.3      0.0111
2520.88     0.0501
759.746     0.1705
262.964     0.36924
102.801     0.4033
```

```
42.9733    0.1434
0 1 6 8.0 1.0
798.262   -0.0052   0.00850
191.162   -0.068    0.0608
63.6885   -0.1314   0.2114
25.3625    0.2517   0.3944
10.7338    0.6433   0.398
3.764      0.2825   0.2251
0 1 4 8.0 1.0
48.1434    0.0122  -0.0215
17.4579   -0.2278  -0.085
6.9972    -0.8801   0.201
3.0791     0.9755   1.3024
0 1 1 2.0 1.0
1.3137     1.0      1.0
0 1 1 0.0 1.0
0.5625     1.0      1.0
0 1 1 0.0 1.0
0.225      1.0      1.0
0 3 4 6.0 1.0
30.4821   0.0583
8.692     0.2591
3.1008    0.5162
1.1709    0.5656
0 3 1 0.0 1.0
0.353683  1.0
```

A.1.2 Oxygen 8-411d11G

```
8 6
0 0 8 2.0 1.0
 8020. 0.001080
 1338. 0.008040
 255.4 0.053240
 69.22 0.168100
 23.90 0.358100
 9.264 0.385500
 3.851 0.146800
 1.212 0.072800
0 1 4 6. 1.0
 49.43 -0.008830 0.009580
 10.47 -0.091500 0.069600
 3.235 -0.040200 0.206500
 1.217  0.379000 0.347000
0 1 1 0. 1.0
 0.486 1. 1.
0 1 1 0. 1.0
 0.1925 1. 1.
0 3 1 0. 1.
 2.0 1.
0 3 1 0. 1.
0.500 1.
```

A.1.3 Carbon 6-311d11G

```
6 6
0 0 6 2.0 1.00
 0.4563240000D+04 0.1966650000D-02
 0.6820240000D+03 0.1523060000D-01
 0.1549730000D+03 0.7612690000D-01
 0.4445530000D+02 0.2608010000D+00
 0.1302900000D+02 0.6164620000D+00
 0.1827730000D+01 0.2210060000D+00
0 1 3 4.0 1.00
 0.2096420000D+02  0.1146600000D+00 0.4024870000D-01
 0.4803310000D+01  0.9199990000D+00 0.2375940000D+00
 0.1459330000D+01 -0.3030680000D-02 0.8158540000D+00
0 1 1 0.0 1.00
 0.4834560000D+00 0.1000000000D+01 0.1000000000D+01
0 1 1 0.0 1.00
 0.1455850000D+00 0.1000000000D+01 0.1000000000D+01
0 3 1 0.0 1.0
 2.0 .1000000000D+01
0 3 1 0.0 1.0
 0.6 .1000000000D+01
```

A.1.4 Hydrogen TZVP

```
1 4
0 0 3 1.0 1.0
34.061341000 0.00602519780
5.1235746000 0.04502109400
1.1646626000 0.20189726000
0 0 1 0.0 1.0
0.4157455100 1.00000000000
0 0 1 0.0 1.0
0.1795111000 1.00000000000
0 2 1 0.0 1.0
0.8000000000 1.00000000000
```

A.2 Vibrational frequencies

Table A.1: Vibrational frequencies in cm^{-1} of C-O adsorbed on Fe(110) at 0.25 ML

Functional	**1st peak**	**2nd peak**	**3rd peak**	**4th peak**
PBE	1725	1756	1762	1815
PBEsol	1747	1776	1783	1843
B3LYP	1755	1794	1798	1875
HSE	1779	1808	1825	1893

Table A.2: Vibrational frequencies in cm^{-1} of C-O adsorbed on Fe(110) at 0.5 ML

Functional	**1st peak**	**2nd peak**
PBE	1879	1932
PBEsol	1907	1960
B3LYP	1894	1955
HSE	1927	1987

Appendix B

Semi-local Corrosion Approximation

B.1 Water chemistry

Constant	Reference
p_{H_2O}	Wagner and Kretzschmar [188]
ρ_{H_2O}	Nordsveen et al. [42]
μ_{H_2O}	Korson et al. [189]
φ_{CO_2}	Duan et al. [190]
$\tilde{V}_{m,CO_2}$	Garcia [191]

Table B.1: References of temperature dependent physicochemical properties

The partial pressure of CO_2 (p_{CO_2}) can be calculated using the water saturation pressure (p_{H_2O}):[188]

$$p_{CO_2} = P_{\text{total}} - p_{H_2O} \tag{B.1}$$

The homogeneous chemical reactions included in the model are shown in Table B.2 where

a_i stands for the activity of species i and f_i is the fugacity of gas i defined as $f_i = p_i\varphi_i$ where φ_i is the fugacity coefficient of gas i

Reaction	**Equilibrium constant**
$H_2O \rightleftharpoons 2\,H^+ + OH^-$	$K_w = \frac{a_{H^+}a_{OH^-}}{a_{H_2O}}$
$CO_{2(g)} \rightleftharpoons CO_{2(aq)}$	$K_H = \frac{a_{CO_2}}{f_{CO_2}a_{H_2O}}$
$CO_2 + H_2O \rightleftharpoons H_2CO_3$	$K_{hy} = \frac{a_{H_2CO_3}}{a_{CO_2}}$
$H_2CO_3 \rightleftharpoons H^+ + HCO_3^-$	$K_{ca} = \frac{a_{H^+}a_{HCO_3^-}}{a_{H_2CO_3}}$
$HCO_3^- \rightleftharpoons H^+ + CO_3^{2-}$	$K_{bi} = \frac{a_{H^+}a_{CO_3^{2-}}}{a_{HCO_3^-}}$

Table B.2: Thermodynamic equilibrium constants of the homogeneous reactions involved in CO_2 corrosion.

Thermodynamic equilibrium constants can also be expressed as a function of the reaction rate constants for the forward and backwards reaction:

$$K = \frac{k_f}{k_b} \tag{B.2}$$

As described by Kahyarian et al.[36] it is necessary to add a correction factor to the definitions of K_H and K_{ca}. The equations defined in their corresponding references assume that CO_2 and H_2CO_3 are the same species (commonly refered to as CO_2^*) due to the difficulty of measuring H_2CO_3 individually:

$$[CO_2^*] = [CO_2] + [H_2CO_3] \tag{B.3}$$

Constant	Reference
K_{w}	Marshall and Franck [192]
K_{H}	Li and Duan [193]
K_{hy}	Kahyarian and Nesic [44]
K_{ca}	Li and Duan [193]
K_{bi}	Li and Duan [193]

Table B.3: Thermodynamic equilibrium constants of the homogeneous rections involved in CO_2 corrosion.

hence

$$K_H = \frac{1}{1 + K_{hyd}} K_H^* \tag{B.4}$$

$$K_{ca} = \left(1 + \frac{1}{K_{hyd}}\right) K_{ca}^* \tag{B.5}$$

B.2 Pitzer model

$$
\begin{aligned}
ln(\gamma_M) = &\sum_{a=1}^{N_a} m_a(2B_{Ma} + ZC_{Ma}) + \sum_{c=1}^{N_c} m_c(2\Phi_{Mc} + \sum_{a=1}^{N_a} m_a\psi_{Mca}) \\
&+ \sum_{a=1}^{N_a-1}\sum_{a'=a+1}^{N_a} m_a m_{a'}\psi_{aa'M} + |z_M|\sum_{c=1}^{N_c}\sum_{a=1}^{N_a} m_c m_a C_{ca} + \sum_{n=1}^{N_n} 2m_n\lambda_{nM} + z_M^2 F
\end{aligned}
\tag{B.6}
$$

$$
\begin{aligned}
ln(\gamma_X) = &\sum_{c=1}^{N_c} m_c(2B_{cX} + ZC_{cX}) + \sum_{a=1}^{N_a} m_a(2\Phi_{Xa} + \sum_{c=1}^{N_c} m_c\psi_{Xac}) \\
&+ \sum_{c=1}^{N_c-1}\sum_{c'=c+1}^{N_c} m_c m_{c'}\psi_{cc'M} + |z_X|\sum_{c=1}^{N_c}\sum_{a=1}^{N_a} m_c m_a C_{ca} + \sum_{n=1}^{N_n} 2m_n\lambda_{nX} + z_X^2 F
\end{aligned}
\tag{B.7}
$$

$$
ln(\gamma_N) = \sum_{n=1}^{N_n} 2m_n\lambda_{Nn} + \sum_{c=1}^{N_c} 2m_c\lambda_{Nc} + \sum_{a=1}^{N_a} 2m_a\lambda_{Na} + \sum_{c=1}^{N_c}\sum_{a=1}^{N_a} m_c m_a\xi_{Nca} \tag{B.8}
$$

$$
ln(a_{\mathrm{H_2O}}) = -\frac{\phi M_{\mathrm{H_2O}}}{1000}\sum m_i \tag{B.9}
$$

The molecular weight of water ($M_{\mathrm{H_2O}}$) is 18.015 and the osmotic pressure (ϕ) is defined as:

$$
\begin{aligned}
(\phi - 1) = &\frac{2}{\sum m_i}\left(-\frac{A^\phi I^{3/2}}{1 + bI^{1/2}}\right)\Bigg[\sum_{c=1}^{N_c}\sum_{a=1}^{N_a} m_c m_a(B_{ca}^\phi + ZC_{ca}) \\
&+ \sum_{c=1}^{N_c-1}\sum_{c'=c+1}^{N_c} m_c m_{c'}\left(\Phi_{cc'}^\phi + \sum_{a=1}^{N_a} m_a\psi_{cc'a}\right) \\
&+ \sum_{a=1}^{N_a-1}\sum_{a'=a+1}^{N_a} m_a m_{a'}\left(\Phi_{aa'}^\phi + \sum_{a=1}^{N_a} m_a\psi_{aa'c}\right) \\
&+ \sum_{n=1}^{N_n}\sum_{a=1}^{N_a} m_n m_a\lambda_{na} + \sum_{n=1}^{N_n}\sum_{c=1}^{N_c} m_n m_c\lambda_{nc} \\
&+ \sum_{n=1}^{N_n}\sum_{c=1}^{N_c}\sum_{a=1}^{N_a} m_n m_c m_a\xi_{nca}\Bigg]
\end{aligned}
\tag{B.10}
$$

F and Z are defined as:

$$Z = \sum_i |z_i| m_i \tag{B.11}$$

$$\begin{aligned} F = &- A^\phi \left(\frac{I^{1/2}}{1 + bI^{1/2}} + \sum_{c=1}^{N_c} \sum_{a=1}^{N_a} m_c m_a B'_{ca} \right. \\ &\left. + \sum_{c=1}^{N_c - 1} \sum_{c'=c+1}^{N_c} m_c m_{c'} \Phi'_{cc} + \sum_{a=1}^{N_a - 1} \sum_{a'=a+1}^{N_a} m_a m_{a'} \Phi'_{aa} \right) \end{aligned} \tag{B.12}$$

where A^ϕ is the Dubye-Huckel limiting slope whose temperature dependence was studied by Pitzer [194] who proposed the following expression:

$$A^\phi = \frac{1}{3} (2\pi \rho N_A)^{1/2} \left(\frac{e^2}{4\pi \varepsilon \varepsilon_0 kT} \right)^{3/2} \tag{B.13}$$

The second virial coefficients of opposite-charge ions (B^ϕ_{MX}, B_{MX} and B'_{MX}) can be obtained using the following expressions:

$$B^\phi_{MX} = \beta^{(0)}_{MX} + \beta^{(1)}_{MX} \exp\left(-a_{MX}\sqrt{I}\right) + \beta^{(2)}_{MX} \exp\left(-12\sqrt{I}\right) \tag{B.14}$$

$$B_{MX} = \beta^{(0)}_{MX} + \beta^{(1)}_{MX} g(a_{MX}\sqrt{I}) + \beta^{(2)}_{MX} g(12\sqrt{I}) \tag{B.15}$$

$$B'_{MX} = \beta^{(1)}_{MX} g'(a_{MX}\sqrt{I})/I + \beta^{(2)}_{MX} g'(12\sqrt{I})/I \tag{B.16}$$

with

$$g(x) = 2\Big(1 - (1+x)e^{-x}\Big)/x^2 \tag{B.17}$$

$$g'(x) = -2\Big(1 - (1 + x + \frac{x^2}{2})e^{-x}\Big)/x^2 \tag{B.18}$$

The second virial coefficients of same-charge ions (Φ^ϕ_{ij}, Φ_{ij} and Φ'_{ij}) can be obtained using the

following expressions:

$$\Phi_{ij}^{\phi} = \theta_{ij} + E_{\theta_{ij}}(I) + IE'_{\theta ij}(I) \tag{B.19}$$

$$\Phi_{ij} = \theta_{ij} + E_{\theta_{ij}}(I) \tag{B.20}$$

$$\Phi'_{ij} = E'_{\theta_{ij}}(I) \tag{B.21}$$

with

$$E_{\theta_{ij}} = \left(\frac{z_i z_j}{4I}\right)\left[J(x_{ij}) - \frac{1}{2}J(x_{ii}) - \frac{1}{2}J(x_{jj})\right] \tag{B.22}$$

$$E'_{\theta_{ij}} = -\left(\frac{E_{\theta_{ij}}}{I}\right) + \left(\frac{z_i z_j}{8I^2}\right)\left[x_{ij}J'(x_{ij}) - \frac{1}{2}x_{ii}J'(x_{ii}) - \frac{1}{2}x_{jj}J'(x_{jj})\right] \tag{B.23}$$

where J and J' can be approximated by the following empirical equations proposed by Pitzer [194]:

$$J = \frac{x}{4 + C_1 x^{-C_2}\exp(-C_3 x^{C_4})} \tag{B.24}$$

$$J' = \frac{x^{C_2}\exp(C_3 x_4^C)(C_1(C_2 + C_3 C_4 x^{C_4} + 1) + 4x^{C_2}\exp(C_3 x^{C_4}))}{\left(C_1 + 4x_2^C \exp(C_3 x^{C_4})\right)^2} \tag{B.25}$$

and $C_M X$ is defined as:

$$C_{MX} = \frac{C_{MX}^{\phi}}{2|z_M z_X|^{1/2}} \tag{B.26}$$

Table B.4 contains the references for the parameters C_{MX}^{ϕ}, Ψ and ξ.

$\beta^{(0)}$, $\beta^{(1)}$, $\beta^{(2)}$ and C^{ϕ}	**Reference**
Na−Cl	Møller [195]
H−Cl	Holmes et al. [196]
Na−OH	Pabalan and Pitzer [197]
Na−OH	Pabalan and Pitzer [197]
$Na-HCO_3^-$	Polya et al. [198]
$Na-CO_3^{2-}$	Polya et al. [198]
Fe−Cl	Pitzer [58]

Table B.4: References for $\beta^{(0)}$, $\beta^{(1)}$ and $\beta^{(2)}$

θ	**Reference**
OH−Cl	Christov and Moller [199]
H−Na	Christov and Moller [199]
$OH-CO_3^{2-}$	Harvie et al. [200]
$Cl-HCO_3^-$	Harvie et al. [200]
$Cl-CO_3^{2-}$	Millero and Pierrot [201]
$CO_3^{2-}-HCO_3^-$	Harvie et al. [200]
Fe−Na	Marion et al. [202]

Table B.5: References for $\beta^{(0)}$, $\beta^{(1)}$ and $\beta^{(2)}$

ψ	**Reference**
Na^+-Cl^--H	Christov and Moller [199]
Na^+-Cl^--OH	Christov and Moller [199]
Na^+-Cl^--Fe	Marion et al. [202]
$Na^+-Cl^--HCO_3^-$	Millero and Pierrot [201]
$Na^+-Cl^--CO_3^{2-}$	Millero and Pierrot [201]
$Na^+-HCO_3^--CO_3^{2-}$	Millero and Pierrot [201]
$Na^+-H^+-HCO_3^-$	Harvie et al. [200]
$Na^+-H^+-CO_3^{2-}$	Harvie et al. [200]
$Na^+-OH^--HCO_3^-$	Harvie et al. [200]
$Na^+-OH^--CO_3^{2-}$	Harvie et al. [200]
$H^+-Cl^--HCO_3^-$	Harvie et al. [200]
$OH^--Cl^--H^+$	Harvie et al. [200]
$Fe^{2+}-Cl^--HCO_3^-$	Marion et al. [202]
$Fe^{2+}-H^+-Cl^-$	Marion et al. [202]

Table B.6: References for the ternary intercation term ψ

B.3 Electrochemistry

Nesic proposed the following empirical equation to describe the rate of iron dissolution:[66]

$$i_a = k[\mathrm{OH}^-]_{surf}^{a_1}(p_{\mathrm{CO}_2})^{a_2} \exp\left(-\frac{\alpha_a F}{RT}\eta\right). \tag{B.27}$$

where k is the rate of reaction constant, $[\mathrm{OH}^-]_{surf}$ is the concentration of OH^- at the reactive surface, p_{CO_2} is the partial pressure of CO_2 and $\eta = E_{\mathrm{app}} - E_{rev}$ is the overpotential.

a_1, a_2 and α_a depend on the pH and partial pressure as follows:

$$a_1 = \begin{cases} 2 & \text{if pH} \leq 4 \\ -\text{pH} + 5 & \text{if } 4 < \text{pH} < 5 \\ 0 & \text{if pH} \geq 5 \end{cases} \tag{B.28}$$

$$a_2 = \begin{cases} 0 & \text{if } p_{\mathrm{CO}_2} \leq 10^{-2} \text{ bar} \\ 1 & \text{if } 10^{-2} \text{ bar} < p_{\mathrm{CO}_2} < 1 \text{ bar} \\ 0 & \text{if } p_{\mathrm{CO}_2} \geq 1 \text{ bar} \end{cases} \tag{B.29}$$

$$\alpha_a = \begin{cases} 2 & \text{if pH} \leq 4 \\ -1.5\text{pH} + 8 & \text{if } 4 < \text{pH} < 5 \\ 0.5 & \text{if pH} \geq 5 \end{cases} \tag{B.30}$$

The reaction rate of the HER reaction can be described by[39,42]

$$i_{\mathrm{ct}} = i_0[\mathrm{H}^+]^a_{\mathrm{surf}} \exp\left(- \frac{\alpha_c F}{RT}\eta \right), \tag{B.31}$$

where the reversible potential of the HER is a function of the pH:

$$E_{\mathrm{rev}} = -\frac{\ln(10)RT}{F}\mathrm{pH}. \tag{B.32}$$

According to Bockris, $\alpha_c = 0.5$ is the most likely value for the HER which is in good agreement with independent experimental data.[39,203]

The temperature dependence of i_0 the reaction can be modelled using an Arrhenius-type equation:

$$i_o = i_{o,\mathrm{ref}} \exp\left(- \frac{\Delta H}{R}\left(\frac{1}{T} - \frac{1}{T_{\mathrm{ref}}}\right)\right), \tag{B.33}$$

where ΔH has been reported to be approximately 30 kJ.[39]

Bockris observed the following relationship between the cathodic current and the pH:[203]

$$\frac{\partial \log i_0}{\partial \mathrm{pH}} = -0.5. \tag{B.34}$$

Nesic calculated $i_{o,\mathrm{ref}}$ to be approximately 0.05 A m^{-2} at 20 °C and pH 4.[39] Hence the HER cathodic current can be expressed as

$$i_c = i_{o,\mathrm{ref}}\left(\frac{[\mathrm{H}^+]_{\mathrm{surf}}}{10^{-4}}\right)^{0.5} \exp\left(- \frac{\alpha_c F}{RT}\eta \right). \tag{B.35}$$

B.4 Mass transport model

The thickness of the mass transfer layer can be obtained using the following relation:[65]

$$\delta_m = \frac{D}{k_{\mathrm{mt}}}. \tag{B.36}$$

Vetter developed the following equation to calculate the thickness of the chemical reaction layer:[63]

$$\delta_r = \frac{D c_{product}}{k_f c_{reactant}} \tag{B.37}$$

Appendix C

Publishing permissions

CCC Marketplace™

This is a License Agreement between Carles Rafols i Belles ("User") and Copyright Clearance Center, Inc. ("CCC") on behalf of the Rightsholder identified in the order details below. The license consists of the order details, the CCC Terms and Conditions below, and any Rightsholder Terms and Conditions which are included below.

All payments must be made in full to CCC in accordance with the CCC Terms and Conditions below.

Order Date	30-Jan-2022	**Type of Use**	Republish in a thesis/dissertation
Order License ID	1183786-1		
ISSN	0142-2421	**Publisher**	JOHN/WILEY & SONS LTD.
		Portion	Image/photo/illustration

LICENSED CONTENT

Publication Title	Surface and interface analysis : SIA	**Publication Type**	Journal
		Start Page	507
Article Title	Core level photoemission line shape selection: Atomic adsorbates on iron	**End Page**	512
		Issue	8
		Volume	52
Date	01/01/1979		
Language	English		
Country	United Kingdom of Great Britain and Northern Ireland		
Rightsholder	John Wiley & Sons - Books		

REQUEST DETAILS

Portion Type	Image/photo/illustration	**Distribution**	U.K. and Commonwealth (excluding Canada)
Number of images / photos / illustrations	2		
Format (select all that apply)	Electronic	**Translation**	Original language of publication
Who will republish the content?	Academic institution	**Copies for the disabled?**	No
Duration of Use	Life of current and all future editions	**Minor editing privileges?**	Yes
Lifetime Unit Quantity	Up to 499	**Incidental promotional use?**	No
Rights Requested	Main product	**Currency**	GBP

NEW WORK DETAILS

Title	Towards Mutiscale modelling of CO2 corrosion	**Institution name**	Imperial College London
Instructor name	Nicholas Harrison	**Expected presentation date**	2022-04-04

ADDITIONAL DETAILS

The requesting person / organization to appear on the license	Carles Rafols i Belles

REUSE CONTENT DETAILS

Title, description or numeric reference of the portion(s)	Figure 2 and 3	**Title of the article/chapter the portion is from**	Core level photoemission line shape selection: Atomic adsorbates on iron
Editor of portion(s)	Acres, Matthew J.; Hussain, Hadeel; Walczak, Monika S.; Nikiel, Marek; Sewell, Christopher; Rafols i Belles, Carles; Ahmad, Ehsan A.; Walton, Alexander S.; Muryn, Christopher A.; Harrison, Nicholas M.; Lindsay, Robert	**Author of portion(s)**	Acres, Matthew J.; Hussain, Hadeel; Walczak, Monika S.; Nikiel, Marek; Sewell, Christopher; Rafols i Belles, Carles; Ahmad, Ehsan A.; Walton, Alexander S.; Muryn, Christopher A.; Harrison, Nicholas M.; Lindsay, Robert
Volume of serial or monograph	52		
Page or page range of portion	507-512	**Publication date of portion**	2020-08-01

RIGHTSHOLDER TERMS AND CONDITIONS

No right, license or interest to any trademark, trade name, service mark or other branding ("Marks") of WILEY or its licensors is granted hereunder, and you agree that you shall not assert any such right, license or interest with respect thereto. You may not alter, remove or suppress in any manner any copyright, trademark or other notices displayed by the Wiley material. This Agreement will be void if the Type of Use, Format, Circulation, or Requestor Type was misrepresented during the licensing process. In no instance may the total amount of Wiley Materials used in any Main Product, Compilation or Collective work comprise more than 5% (if figures/tables) or 15% (if full articles/chapters) of the (entirety of the) Main Product, Compilation or Collective Work. Some titles may be available under an Open Access license. It is the Licensors' responsibility to identify the type of Open Access license on which the requested material was published, and comply fully with the terms of that license for the type of use specified Further details can be found on Wiley Online Library http://olabout.wiley.com/WileyCDA/Section/id-410895.html.

CCC Terms and Conditions

1. Description of Service; Defined Terms. This Republication License enables the User to obtain licenses for republication of one or more copyrighted works as described in detail on the relevant Order Confirmation (the "Work(s)"). Copyright Clearance Center, Inc. ("CCC") grants

licenses through the Service on behalf of the rightsholder identified on the Order Confirmation (the "Rightsholder"). "Republication", as used herein, generally means the inclusion of a Work, in whole or in part, in a new work or works, also as described on the Order Confirmation. "User", as used herein, means the person or entity making such republication.

2. The terms set forth in the relevant Order Confirmation, and any terms set by the Rightsholder with respect to a particular Work, govern the terms of use of Works in connection with the Service. By using the Service, the person transacting for a republication license on behalf of the User represents and warrants that he/she/it (a) has been duly authorized by the User to accept, and hereby does accept, all such terms and conditions on behalf of User, and (b) shall inform User of all such terms and conditions. In the event such person is a "freelancer" or other third party independent of User and CCC, such party shall be deemed jointly a "User" for purposes of these terms and conditions. In any event, User shall be deemed to have accepted and agreed to all such terms and conditions if User republishes the Work in any fashion.

3. Scope of License; Limitations and Obligations.

    3.1. All Works and all rights therein, including copyright rights, remain the sole and exclusive property of the Rightsholder. The license created by the exchange of an Order Confirmation (and/or any invoice) and payment by User of the full amount set forth on that document includes only those rights expressly set forth in the Order Confirmation and in these terms and conditions, and conveys no other rights in the Work(s) to User. All rights not expressly granted are hereby reserved.

    3.2. General Payment Terms: You may pay by credit card or through an account with us payable at the end of the month. If you and we agree that you may establish a standing account with CCC, then the following terms apply: Remit Payment to: Copyright Clearance Center, 29118 Network Place, Chicago, IL 60673-1291. Payments Due: Invoices are payable upon their delivery to you (or upon our notice to you that they are available to you for downloading). After 30 days, outstanding amounts will be subject to a service charge of 1-1/2% per month or, if less, the maximum rate allowed by applicable law. Unless otherwise specifically set forth in the Order Confirmation or in a separate written agreement signed by CCC, invoices are due and payable on "net 30" terms. While User may exercise the rights licensed immediately upon issuance of the Order Confirmation, the license is automatically revoked and is null and void, as if it had never been issued, if complete payment for the license is not received on a timely basis either from User directly or through a payment agent, such as a credit card company.

    3.3. Unless otherwise provided in the Order Confirmation, any grant of rights to User (i) is "one-time" (including the editions and product family specified in the license), (ii) is non-exclusive and non-transferable and (iii) is subject to any and all limitations and restrictions (such as, but not limited to, limitations on duration of use or circulation) included in the Order Confirmation or invoice and/or in these terms and conditions. Upon completion of the licensed use, User shall either secure a new permission for further use of the Work(s) or immediately cease any new use of the Work(s) and shall render inaccessible (such as by deleting or by removing or severing links or other locators) any further copies of the Work (except for copies printed on paper in accordance with this license and still in User's stock at the end of such period).

    3.4. In the event that the material for which a republication license is sought includes third party materials (such as photographs, illustrations, graphs, inserts and similar materials) which are identified in such material as having been used by permission, User is responsible for identifying, and seeking separate licenses (under this Service

or otherwise) for, any of such third party materials; without a separate license, such third party materials may not be used.

3.5. Use of proper copyright notice for a Work is required as a condition of any license granted under the Service. Unless otherwise provided in the Order Confirmation, a proper copyright notice will read substantially as follows: "Republished with permission of [Rightsholder's name], from [Work's title, author, volume, edition number and year of copyright]; permission conveyed through Copyright Clearance Center, Inc. " Such notice must be provided in a reasonably legible font size and must be placed either immediately adjacent to the Work as used (for example, as part of a by-line or footnote but not as a separate electronic link) or in the place where substantially all other credits or notices for the new work containing the republished Work are located. Failure to include the required notice results in loss to the Rightsholder and CCC, and the User shall be liable to pay liquidated damages for each such failure equal to twice the use fee specified in the Order Confirmation, in addition to the use fee itself and any other fees and charges specified.

3.6. User may only make alterations to the Work if and as expressly set forth in the Order Confirmation. No Work may be used in any way that is defamatory, violates the rights of third parties (including such third parties' rights of copyright, privacy, publicity, or other tangible or intangible property), or is otherwise illegal, sexually explicit or obscene. In addition, User may not conjoin a Work with any other material that may result in damage to the reputation of the Rightsholder. User agrees to inform CCC if it becomes aware of any infringement of any rights in a Work and to cooperate with any reasonable request of CCC or the Rightsholder in connection therewith.

4. Indemnity. User hereby indemnifies and agrees to defend the Rightsholder and CCC, and their respective employees and directors, against all claims, liability, damages, costs and expenses, including legal fees and expenses, arising out of any use of a Work beyond the scope of the rights granted herein, or any use of a Work which has been altered in any unauthorized way by User, including claims of defamation or infringement of rights of copyright, publicity, privacy or other tangible or intangible property.

5. Limitation of Liability. UNDER NO CIRCUMSTANCES WILL CCC OR THE RIGHTSHOLDER BE LIABLE FOR ANY DIRECT, INDIRECT, CONSEQUENTIAL OR INCIDENTAL DAMAGES (INCLUDING WITHOUT LIMITATION DAMAGES FOR LOSS OF BUSINESS PROFITS OR INFORMATION, OR FOR BUSINESS INTERRUPTION) ARISING OUT OF THE USE OR INABILITY TO USE A WORK, EVEN IF ONE OF THEM HAS BEEN ADVISED OF THE POSSIBILITY OF SUCH DAMAGES. In any event, the total liability of the Rightsholder and CCC (including their respective employees and directors) shall not exceed the total amount actually paid by User for this license. User assumes full liability for the actions and omissions of its principals, employees, agents, affiliates, successors and assigns.

6. Limited Warranties. THE WORK(S) AND RIGHT(S) ARE PROVIDED "AS IS". CCC HAS THE RIGHT TO GRANT TO USER THE RIGHTS GRANTED IN THE ORDER CONFIRMATION DOCUMENT. CCC AND THE RIGHTSHOLDER DISCLAIM ALL OTHER WARRANTIES RELATING TO THE WORK(S) AND RIGHT(S), EITHER EXPRESS OR IMPLIED, INCLUDING WITHOUT LIMITATION IMPLIED WARRANTIES OF MERCHANTABILITY OR FITNESS FOR A PARTICULAR PURPOSE. ADDITIONAL RIGHTS MAY BE REQUIRED TO USE ILLUSTRATIONS, GRAPHS, PHOTOGRAPHS, ABSTRACTS, INSERTS OR OTHER PORTIONS OF THE WORK (AS OPPOSED TO THE ENTIRE WORK) IN A MANNER CONTEMPLATED BY USER; USER UNDERSTANDS AND AGREES THAT NEITHER CCC NOR THE RIGHTSHOLDER MAY HAVE SUCH ADDITIONAL RIGHTS TO GRANT.

7. Effect of Breach. Any failure by User to pay any amount when due, or any use by User of a Work beyond the scope of the license set forth in the Order Confirmation and/or these terms and conditions, shall be a material breach of the license created by the Order Confirmation

and these terms and conditions. Any breach not cured within 30 days of written notice thereof shall result in immediate termination of such license without further notice. Any unauthorized (but licensable) use of a Work that is terminated immediately upon notice thereof may be liquidated by payment of the Rightsholder's ordinary license price therefor; any unauthorized (and unlicensable) use that is not terminated immediately for any reason (including, for example, because materials containing the Work cannot reasonably be recalled) will be subject to all remedies available at law or in equity, but in no event to a payment of less than three times the Rightsholder's ordinary license price for the most closely analogous licensable use plus Rightsholder's and/or CCC's costs and expenses incurred in collecting such payment.

8. Miscellaneous.

8.1. User acknowledges that CCC may, from time to time, make changes or additions to the Service or to these terms and conditions, and CCC reserves the right to send notice to the User by electronic mail or otherwise for the purposes of notifying User of such changes or additions; provided that any such changes or additions shall not apply to permissions already secured and paid for.

8.2. Use of User-related information collected through the Service is governed by CCC's privacy policy, available online here:https://marketplace.copyright.com/rs-ui-web/mp/privacy-policy

8.3. The licensing transaction described in the Order Confirmation is personal to User. Therefore, User may not assign or transfer to any other person (whether a natural person or an organization of any kind) the license created by the Order Confirmation and these terms and conditions or any rights granted hereunder; provided, however, that User may assign such license in its entirety on written notice to CCC in the event of a transfer of all or substantially all of User's rights in the new material which includes the Work(s) licensed under this Service.

8.4. No amendment or waiver of any terms is binding unless set forth in writing and signed by the parties. The Rightsholder and CCC hereby object to any terms contained in any writing prepared by the User or its principals, employees, agents or affiliates and purporting to govern or otherwise relate to the licensing transaction described in the Order Confirmation, which terms are in any way inconsistent with any terms set forth in the Order Confirmation and/or in these terms and conditions or CCC's standard operating procedures, whether such writing is prepared prior to, simultaneously with or subsequent to the Order Confirmation, and whether such writing appears on a copy of the Order Confirmation or in a separate instrument.

8.5. The licensing transaction described in the Order Confirmation document shall be governed by and construed under the law of the State of New York, USA, without regard to the principles thereof of conflicts of law. Any case, controversy, suit, action, or proceeding arising out of, in connection with, or related to such licensing transaction shall be brought, at CCC's sole discretion, in any federal or state court located in the County of New York, State of New York, USA, or in any federal or state court whose geographical jurisdiction covers the location of the Rightsholder set forth in the Order Confirmation. The parties expressly submit to the personal jurisdiction and venue of each such federal or state court.If you have any comments or questions about the Service or Copyright Clearance Center, please contact us at 978-750-8400 or send an e-mail to support@copyright.com.

v 1.1

Bibliography

[1] Tanaporn Tanupabrungsun. *Thermodynamics and Kinetics of Carbon Dioxide Corrosion of Mild Steel at Elevated Temperatures*. PhD thesis, Russ College of Engineering and Technology of Ohio University, 2013.

[2] W Erley. Vibrational spectra of co chemisorbed on fe (110). *Journal of Vacuum Science and Technology*, 18(2):472–475, 1981.

[3] Matthew J Acres, Hadeel Hussain, Monika S Walczak, Marek Nikiel, Christopher Sewell, Carles Rafols i Belles, Ehsan A Ahmad, Alexander S Walton, Christopher A Muryn, Nicholas M Harrison, et al. Core level photoemission line shape selection: Atomic adsorbates on iron. *Surface and Interface Analysis*, 52(8):507–512, 2020.

[4] Pierre R Roberge. *Handbook of corrosion engineering*. McGraw-Hill Education, 2019.

[5] Gerhardus Koch, Jeff Varney, Neil Thompson, Oliver Moghissi, Melissa Gould, and Joe Payer. International measures of prevention, application, and economics of corrosion technologies study. *NACE International*, page 216, 2016.

[6] Gerhardus Koch. Trends in oil and gas corrosion research and technologies. *Trends in Oil and Gas Corrosion Research and Technologies*, 2017.

[7] U.S. DOT Pipeline and Hazardous Materials Safety Administration. Crude oil/refined

petroleum/biofuel accidents impacting people or the environment: Apparent causes for 2010 - 2020. Technical report, U.S. Department of Transportation, 2021.

[8] M B Kermani and L M Smith. *A working party report on COsub 2 corrosion control in oil and gas production. Design considerations*. Maney Pub, 1997.

[9] S Sh Abedi, A Abdolmaleki, and N Adibi. Failure analysis of scc and srb induced cracking of a transmission oil products pipeline. *Engineering Failure Analysis*, 14(1): 250–261, 2007.

[10] Cheng-hong Peng, Zheng-yi Liu, and Xing-zhao Wei. Failure analysis of a steel tube joint perforated by corrosion in a well-drilling pipe. *Engineering Failure Analysis*, 25: 13–28, 2012.

[11] Lekan Taofeek Popoola, Alhaji Shehu Grema, Ganiyu Kayode Latinwo, Babagana Gutti, and Adebori Saheed Balogun. Corrosion problems during oil and gas production and its mitigation. *International Journal of Industrial Chemistry*, 4(1):1–15, 2013.

[12] M Askari, M Aliofkhazraei, and S Afroukhteh. A comprehensive review on internal corrosion and cracking of oil and gas pipelines. *Journal of Natural Gas Science and Engineering*, 71:102971, 2019.

[13] AM El-Sherik. *Trends in oil and gas corrosion research and technologies: Production and transmission*. Woodhead Publishing, 2017.

[14] MB Kermani and A Morshed. Carbon dioxide corrosion in oil and gas productiona compendium. *Corrosion*, 59(08), 2003.

[15] MB Kermani and Don Harrop. The impact of corrosion on oil and gas industry. *SPE Production & Facilities*, 11(03):186–190, 1996.

[16] Aria Kahyarian, Marc Singer, and Srdjan Nesic. Modeling of uniform CO2 corrosion of mild steel in gas transportation systems: A review, feb 2016. ISSN 18755100. URL https://www.sciencedirect.com/science/article/abs/pii/S1875510015303437.

[17] BR Linter and GT Burstein. Reactions of pipeline steels in carbon dioxide solutions. *Corrosion science*, 41(1):117–139, 1999.

[18] Elias Remita, Bernard Tribollet, E Sutter, Vincent Vivier, Francois Ropital, and Jean Kittel. Hydrogen evolution in aqueous solutions containing dissolved co2: Quantitative contribution of the buffering effect. *Corrosion science*, 50(5):1433–1440, 2008.

[19] Thu Tran, Bruce Brown, Srdjan Nesic, et al. Corrosion of mild steel in an aqueous co2 environment—basic electrochemical mechanisms revisited. *CORROSION/2015*, 2015.

[20] Aria Kahyarian, Bruce Brown, and Srdjan Nešić. Electrochemistry of co2 corrosion of mild steel: effect of co2 on cathodic currents. *Corrosion*, 74(8):851–859, 2018.

[21] Aria Kahyarian, Bruce Brown, and Srdjan Nesic. Mechanism of co2 corrosion of mild steel: a new narrative. *CORROSION*, page Paper No. 11232, jul 2018. ISSN 03614409. URL https://www.onepetro.org/conference-paper/NACE-2018-11232.

[22] G Schmitt and B Rothmann. Studies on the corrosion mechanism of unalloyed steel in oxygen-free carbon dioxide solutions, part i. kinetics of the liberation of hydrogen. *Werkstoffe und korrosion*, 28(12):816–822, 1977.

[23] Aria Kahyarian and Srdjan Nesic. A new narrative for co2 corrosion of mild steel. *Journal of The Electrochemical Society*, 166(11):C3048–C3063, 2019.

[24] S. Menezes, R. Haak, G. Hagen, and M. Kendig. Photoelectrochemical characterization of corrosion inhibiting oxide films on aluminum and its alloys. *Journal of The*

Electrochemical Society, 136(7):1884–1886, jul 1989. doi: 10.1149/1.2097069. URL https://doi.org/10.1149%2F1.2097069.

[25] Eric Van Hunnik, ELJA Hendriksen, Bernardus FM Pots, et al. The formation of protective fe3co2 corrosion product layers in co corrosion. In *CORROSION 96*. Nace International, 1996.

[26] S Nešic and K-LJ Lee. A mechanistic model for carbon dioxide corrosion of mild steel in the presence of protective iron carbonate films—part 3: film growth model. *Corrosion*, 59(7):616–628, 2003.

[27] Arne Dugstad et al. Mechanism of protective film formation during co2 corrosion of carbon steel. In *CORROSION 98*. Nace International, 1998.

[28] Srdjan Nešić. Key issues related to modelling of internal corrosion of oil and gas pipelines–a review. *Corrosion science*, 49(12):4308–4338, 2007.

[29] V Ruzic, M Veidt, and S Nešic. Protective iron carbonate films—part 3: simultaneous chemo-mechanical removal in single-phase aqueous flow. *Corrosion*, 63(8):758–769, 2007.

[30] Richard Barker, Daniel Burkle, Thibaut Charpentier, Harvey Thompson, and Anne Neville. A review of iron carbonate (feco3) formation in the oil and gas industry. *Corrosion Science*, 142:312–341, 2018.

[31] C De Waard and DE Milliams. Carbonic acid corrosion of steel. *Corrosion*, 31(5): 177–181, 1975.

[32] C De Waard, U Lotz, and DE Milliams. Predictive model for co2 corrosion engineering in wet natural gas pipelines. *Corrosion*, 47(12):976–985, 1991.

[33] C de Waard and U Lotz. Prediction of co2 corrosion of carbon steel‖, paper no. 69. *CORROSION/93,(Houston, TX: NACE International, 1993)*, 1993.

[34] C De Waard, U Lotz, and Ame Dugstad. Influence of liquid flow velocity on co {sub 2} corrosion: A semi-empirical model. Technical report, NACE International, Houston, TX (United States), 1995.

[35] Liane Smith, Kees de Waard, and Bruce D Craig. The influence of crude oils on well tubing corrosion rates. In *CORROSION 2003*. OnePetro, 2003.

[36] Aria Kahyarian, Mohsen Achour, and Srdjan Nesic. Mathematical modeling of uniform CO 2 corrosion. In *Trends in Oil and Gas Corrosion Research and Technologies: Production and Transmission*, pages 805–849. Woodhead Publishing, jan 2017. ISBN 9780081012192. doi: 10.1016/B978-0-08-101105-8.00034-6. URL https://www.sciencedirect.com/science/article/pii/B9780081011058000346.

[37] Linda GS Gray, Bruce G Anderson, Michael J Danysh, and Peter R Tremaine. Effect of ph and temperature on the mechanism of carbon steel corrosion by aqueous carbon dioxide. *Corrosion/90, paper*, 40, 1990.

[38] E Dayalan, G Vani, JR Shadley, and S Shirazi. Modeling co 2 corrosion of carbon steels in pipe flow. *E. Dayalan, G. Vani, J. R. Shadley, S. A. Shirazi, and E. F. Rybicki, Paper*, (118), 1995.

[39] S. Nesic, J. Postlethwaite, and S. Olsen. An electrochemical model for prediction of corrosion of mild steel in aqueous carbon dioxide solutions. *CORROSION*, 52(4): 280–294, 1996. doi: 10.5006/1.3293640.

[40] S Turgoose, RA Cottis, and K Lawson. Modeling of electrode processes and surface chemistry in carbon dioxide containing solutions. In *Computer Modeling in Corrosion*. ASTM International, 1992.

[41] B FM Pots. Mechanistic models for the prediction of co {sub 2} corrosion rates under

multi-phase flow conditions. Technical report, NACE International, Houston, TX (United States), 1995.

[42] M Nordsveen, S Nešic, R Nyborg, and A Stangeland. A mechanistic model for carbon dioxide corrosion of mild steel in the presence of protective iron carbonate films—part 1: theory and verification. *Corrosion*, 59(5):443–456, 2003.

[43] S Nešic, M Nordsveen, R Nyborg, and A Stangeland. A mechanistic model for carbon dioxide corrosion of mild steel in the presence of protective iron carbonate films—part 2: a numerical experiment. *Corrosion*, 59(6):489–497, 2003.

[44] Aria Kahyarian and Srdjan Nesic. On the mechanism of carbon dioxide corrosion of mild steel: Experimental investigation and mathematical modeling at elevated pressures and non-ideal solutions. *Corrosion Science*, page 108719, 2020.

[45] R Reigada, F Sagues, and JM Costa. A monte carlo simulation of localized corrosion. *The Journal of chemical physics*, 101(3):2329–2337, 1994.

[46] F Caleyo, JC Velázquez, A Valor, and JM Hallen. Probability distribution of pitting corrosion depth and rate in underground pipelines: A monte carlo study. *Corrosion Science*, 51(9):1925–1934, 2009.

[47] Cristian Felipe Pérez-Brokate, Dung Di Caprio, Damien Féron, Jacques De Lamare, and Annie Chaussé. Overview of cellular automaton models for corrosion. In *International Conference on Cellular Automata*, pages 187–196. Springer, 2014.

[48] Łukasz Bartosik, Dung Di Caprio, and Janusz Stafiej. Cellular automata approach to corrosion and passivity phenomena. *Pure and Applied Chemistry*, 85(1):247–256, 2012.

[49] E. Remita, B. Tribollet, E. Sutter, F. Ropital, X. Longaygue, J. Kittel, C. Taravel-Condat, and N. Desamais. A Kinetic Model for CO[sub 2] Corrosion of Steel in Confined

Aqueous Environments. *Journal of The Electrochemical Society*, 155(1):C41, jan 2007. ISSN 00134651. doi: 10.1149/1.2801349. URL http://jes.ecsdl.org/cgi/doi/10.1149/1.2801349.

[50] Jiabin Han, J William Carey, and Jinsuo Zhang. A coupled electrochemical–geochemical model of corrosion for mild steel in high-pressure co2–saline environments. *International Journal of Greenhouse Gas Control*, 5(4):777–787, 2011.

[51] Madan Gopal, Ruolan Zhang, and S Rajappa. Modeling the diffusion effects through the iron carbonate layer in the carbon dioxide corrosion of carbon steel. *CORROSION 98*, 1998.

[52] Andrzej Anderko et al. Simulation of feco˜ 3/fes scale formation using thermodynamic and electrochemical models. In *CORROSION-NATIONAL ASSOCIATION OF CORROSION ENGINEERS ANNUAL CONFERENCE-*. NACE, 2000.

[53] Srdjan Nesic, Ying Xiao, and Bernardus FM Pots. A quasi 2-D localised corrosion model. *Corrosion 2004*, (04628):16, 2004. URL http://www.icmt.ohio.edu/Nesic/papers/fulltext/conference-58.pdf.

[54] RA De Motte, R Barker, D Burkle, SM Vargas, and A Neville. The early stages of feco3 scale formation kinetics in co2 corrosion. *Materials Chemistry and Physics*, 216: 102–111, 2018.

[55] MP Tautschnig, NM Harrison, and MW Finnis. A model for time-dependent grain boundary diffusion of ions and electrons through a film or scale, with an application to alumina. *Acta Materialia*, 132:503–516, 2017.

[56] SV Lishchuk, R Akid, and K Worden. A cellular automaton based model for predicting intergranular corrosion in aerospace alloys. *Proc. EUROCORR–2008, Edinburgh, UK*, 2008.

[57] Pieter Van der Weeën, Alexsandro M Zimer, Ernesto C Pereira, Lucia H Mascaro, Odemir M Bruno, and Bernard De Baets. Modeling pitting corrosion by means of a 3d discrete stochastic model. *Corrosion Science*, 82:133–144, 2014.

[58] Kenneth S Pitzer. Ion interaction approach: theory and data correlation. *Activity coefficients in electrolyte solutions*, 2:75–153, 1991.

[59] Vladimir S Bagotsky. *Fundamentals of electrochemistry*, volume 44. John Wiley & Sons, 2005.

[60] Allen J Bard, Larry R Faulkner, et al. *Fundamentals and applications: electrochemical methods*. Wiley, New York, 2001.

[61] WZ Nernst. Oscillometric investigation of sparingly soluble sulfates. *Physik. Chem*, 47: 52, 1904.

[62] EZ Brunner. physik. chem. *Physical Chemistry*, 47:56, 1904.

[63] Klaus J Vetter and Stanley Bruckenstein. *Electrochemical Kinetics: Theoretical and Experimental Aspects: Revisions, Additions, and a Foreword to the English Language Ed. Prepared by the Author*. Academic Press, 1967.

[64] Allen J Bard and Larry R Faulkner. Electrochemical methods: Fundamentals and applications. *Surface Technology*, 20(1):91–92, 1983.

[65] Srdjan Nesic, BFM Pots, John Postlethwaite, and Nicolas Thevenot. Superposition of diffusion and chemical reaction controlled limiting currents-application to co2 corrosion. *Journal of Corrosion Science and engineering*, 1(3), 1995.

[66] S Nesic, N Thevenot, JL Crolet, and M Drazic. Electrochemical properties of iron dissolution in the presence of co2–basics revisited; paper no. 3. *CORROSION/96 (NACE)*, 1996.

[67] ML Johnson and MB Tomson. Ferrous carbonate precipitation kinetics and its impact co 2 corrosion. *M. L. Johnson, M. B. Tomson, CORROSION 91/268, NACE, Houston, TX.*, 1991.

[68] Eric Van Hunnik, ELJA Hendriksen, Bernardus FM Pots, et al. The formation of protective fe3co2 corrosion product layers in co corrosion. In *CORROSION 96*. Nace International, 1996.

[69] Wei Sun, Srdjan Nesic, et al. Basics revisited: kinetics of iron carbonate scale precipitation in co2 corrosion. *Corrosion/2006, paper*, (06365), 2006.

[70] Kunal Chokshi, Wei Sun, and Srdjan Nesic. Iron carbonate scale growth and the effect of inhibition in co2 corrosion of mild steel. *Corrosion/2005, paper*, (05285), 2005.

[71] W Sun and S Nešic. Kinetics of corrosion layer formation: part 1—iron carbonate layers in carbon dioxide corrosion. *Corrosion*, 64(4):334–346, 2008.

[72] Zheng Ma, Yang Yang, Bruce Brown, Srdjan Nesic, and Marc Singer. Investigation of precipitation kinetics of feco3 by eqcm. *Corrosion Science*, 141:195–202, 2018.

[73] Wei Sun, Srdjan Nešić, and Richard C Woollam. The effect of temperature and ionic strength on iron carbonate (feco3) solubility limit. *Corrosion Science*, 51(6):1273–1276, 2009.

[74] Xin Gao, Fazlollah Madani Sani, Zheng Ma, Bruce Brown, Marc Singer, and Srdjan Nesic. A quantitative study of feco3 solubility in non-ideal solutions. In *CORROSION 2021*. OnePetro, 2021.

[75] Janet Greenberg and Mason Tomson. Precipitation and dissolution kinetics and equilibria of aqueous ferrous carbonate vs temperature. *Applied Geochemistry*, 7(2):185–190, 1992.

[76] SV Golubev, P Bénézeth, J Schott, JL Dandurand, and A Castillo. Siderite dissolution kinetics in acidic aqueous solutions from 25 to 100 c and 0 to 50 atm pco2. *Chemical Geology*, 265(1-2):13–19, 2009.

[77] Owen W Duckworth and Scot T Martin. Dissolution rates and pit morphologies of rhombohedral carbonate minerals. *American Mineralogist*, 89(4):554–563, 2004.

[78] S Nešic, G Th Solvi, and J Enerhaug. Comparison of the rotating cylinder and pipe flow tests for flow-sensitive carbon dioxide corrosion. *Corrosion*, 51(10):773–787, 1995.

[79] Joshua Owen, Jack Godfrey, Wenlong Ma, Greg de Boer, Mohammed Al-Khateeb, Harvey Thompson, Anne Neville, Callum Ramsey, and Richard Barker. An experimental and numerical investigation of co2 corrosion in a rapid expansion pipe geometry. *Corrosion Science*, 165:108362, 2020.

[80] M Al-Khateeb, R Barker, A Neville, and HM Thompson. The effect of surface roughness on diffusion and chemical reaction controlled limiting currents on a rotating cylinder electrode in deaerated solutions with and without co2. *Corrosion*, 74(9):971–983, 2018.

[81] DC Silverman. The rotating cylinder electrode for examining velocity-sensitive corrosion—a review. *Corrosion*, 60(11):1003–1023, 2004.

[82] M Eisenberg, CW Tobias, and CR Wilke. Ionic mass transfer and concentration polarization at rotating electrodes. *Journal of the Electrochemical Society*, 101(6):306, 1954.

[83] FP Berger and K-FF-L Hau. Mass transfer in turbulent pipe flow measured by the electrochemical method. *International Journal of Heat and Mass Transfer*, 20(11): 1185–1194, 1977.

[84] Peter Grathwohl. *Diffusion in natural porous media: contaminant transport, sorption/desorption and dissolution kinetics*, volume 1. Springer Science & Business Media, 2012.

[85] FAL Dullien. Characterization of porous media—pore level. In *Mathematical Modeling for Flow and Transport Through Porous Media*, pages 581–606. Springer, 1991.

[86] Klaus Probst and Klaus Wohlfahrt. Empirische abschätzung effektiver diffusionskoeffizienten in porösen systemen. *Chemie Ingenieur Technik*, 51(7):737–739, 1979.

[87] Ya-Chiao Chang, Richard Woollam, and Mark E Orazem. Mathematical models for under-deposit corrosion i. aerated media. *Journal of The Electrochemical Society*, 161 (6):C321–C329, 2014.

[88] John Newman and Karen E Thomas-Alyea. *Electrochemical systems*. John Wiley & Sons, 2012.

[89] JF Sánchez, Francisco Alhama, and JA Moreno. An efficient and reliable model based on network method to simulate co2 corrosion with protective iron carbonate films. *Computers & Chemical Engineering*, 39:57–64, 2012.

[90] Ehsan A Ahmad, Hao-Yeh Chang, Mohammed Al-Kindi, Gaurav R Joshi, Karyn Cooper, Robert Lindsay, and Nicholas M Harrison. Corrosion protection through naturally occurring films: New insights from iron carbonate. *ACS applied materials & interfaces*, 11(36):33435–33441, 2019.

[91] B Chopard and M Droz. Cellular automata. *Modelling of Physical*, 1998.

[92] S. Nesic and W. Sun. 2.25 - corrosion in acid gas solutions. In Bob Cottis, Michael Graham, Robert Lindsay, Stuart Lyon, Tony Richardson, David Scantlebury, and Howard Stott, editors, *Shreir's Corrosion*, pages 1270–1298. Elsevier, Oxford, 2010.

ISBN 978-0-444-52787-5. doi: https://doi.org/10.1016/B978-044452787-5.00055-X. URL https://www.sciencedirect.com/science/article/pii/B978044452787500055X.

[93] Yuhua Sun, Keith George, and Srdjan Nesic. The effect of cl-and acetic acid on localized co2 corrosion in wet gas flow. In *CORROSION 2003*. OnePetro, 2003.

[94] DE Williams, C Westcott, and M Fleischmann. Studies of the initiation of pitting corrosion on stainless steels. *Journal of electroanalytical chemistry and interfacial electrochemistry*, 180(1-2):549–564, 1984.

[95] DE Williams, C Westcott, and M Fleischmann. Stochastic models of pitting corrosion of stainless steels: I. modeling of the initiation and growth of pits at constant potential. *Journal of the Electrochemical Society*, 132(8):1796, 1985.

[96] DE Williams, C Westcott, and M Fleischmann. Stochastic models of pitting corrosion of stainless steels: Ii. measurement and interpretation of data at constant potential. *Journal of the Electrochemical Society*, 132(8):1804, 1985.

[97] C Gabrielli, F Huet, M Keddam, and R Oltra. A review of the probabilistic aspects of localized corrosion. *Corrosion*, 46(4):266–278, 1990.

[98] B Wu, JR Scully, JL Hudson, and Alexander S Mikhailov. Cooperative stochastic behavior in localized corrosion: I. model. *Journal of the electrochemical society*, 144(5): 1614, 1997.

[99] Misao Hashimoto, Shumpei Miyajima, and Tomomi Murata. A stochastic analysis of potential fluctuation during passive film breakdown and repair on iron. *Corrosion Science*, 33(6):885–904, 1992.

[100] GS Frankel. Pitting corrosion of metals: a review of the critical factors. *Journal of the Electrochemical society*, 145(6):2186, 1998.

[101] Srdjan SNesic, Shihuai Wang, and Keith George. High pressure co2 corrosion electrochemistry and the effect of acetic acid. In *CORROSION 2004*. OnePetro, 2004.

[102] Rolf Nyborg. Pipeline corrosion prevention by ph stabilization or corrosion inhibitors. In *Rio Pipeline Conference and Exposition 2009*, 2009.

[103] M Honarvar Nazari, SR Allahkaram, and MB Kermani. The effects of temperature and ph on the characteristics of corrosion product in co2 corrosion of grade x70 steel. *Materials & Design*, 31(7):3559–3563, 2010.

[104] Wei Li, Bruce Brown, David Young, and Srdjan Nešić. Investigation of pseudo-passivation of mild steel in co2 corrosion. *Corrosion*, 70(3):294–302, 2014.

[105] Frederick Pessu, Richard Barker, and Anne Neville. The influence of ph on localized corrosion behavior of x65 carbon steel in co2-saturated brines. *Corrosion*, 71(12): 1452–1466, 2015.

[106] Z Fa Yin, YR Feng, WZ Zhao, ZQ Bai, and GF Lin. Effect of temperature on co2 corrosion of carbon steel. *Surface and Interface Analysis: An International Journal devoted to the development and application of techniques for the analysis of surfaces, interfaces and thin films*, 41(6):517–523, 2009.

[107] P Bénézeth, JL Dandurand, and JC Harrichoury. Solubility product of siderite (feco3) as a function of temperature (25–250 c). *Chemical Geology*, 265(1-2):3–12, 2009.

[108] William Durnie, Roland De Marco, Alan Jefferson, and Brian Kinsella. Development of a structure-activity relationship for oil field corrosion inhibitors. *Journal of the Electrochemical Society*, 146(5):1751, 1999.

[109] S Ramachandran and V Jovancicevic. Molecular modeling of the inhibition of mild steel carbon dioxide corrosion by imidazolines. *Corrosion*, 55(03), 1999.

[110] Hany Mohamed Abd El-Lateef, Vagif Maharram Abbasov, Leylufer Imran Aliyeva, and Teyyub Allahverdi Ismayilov. Corrosion protection of steel pipelines against co2 corrosion-a review. *Chemistry Journal*, 2(2):52–63, 2012.

[111] IB Obot, K Haruna, and TA Saleh. Atomistic simulation: a unique and powerful computational tool for corrosion inhibition research. *Arabian Journal for Science and Engineering*, 44(1):1–32, 2019.

[112] Hossein DorMohammadi, Qin Pang, Líney Árnadóttir, and O Burkan Isgor. Atomistic simulation of initial stages of iron corrosion in pure water using reactive molecular dynamics. *Computational Materials Science*, 145:126–133, 2018.

[113] IB Obot, DD Macdonald, and ZM Gasem. Density functional theory (dft) as a powerful tool for designing new organic corrosion inhibitors. part 1: an overview. *Corrosion Science*, 99:1–30, 2015.

[114] Zheng Chen, Yumei Nong, Jianhua Chen, Ye Chen, and Bo Yu. A dft study on corrosion mechanism of steel bar under water-oxygen interaction. *Computational Materials Science*, 171:109265, 2020.

[115] Weimin Cao. Using and validation of the dft method for oxygen adsorbed on the iron (100) surface. *Mineral Processing and Extractive Metallurgy*, 119(2):67–70, 2010.

[116] S-H Dang, C-X Li, and P-D Han. Synergetic effects of impurities and alloying element cr on oxidation and dissolution corrosion of ni (111) surfaces: A dft study. *Chinese Journal of Physics*, 61:1–7, 2019.

[117] Dharmendr Kumar, Nimesh Jain, Vinay Jain, and Beena Rai. Amino acids as copper corrosion inhibitors: A density functional theory approach. *Applied Surface Science*, 514:145905, 2020.

[118] Attila Szabo and Neil S Ostlund. *Modern quantum chemistry: introduction to advanced electronic structure theory*. Courier Corporation, 2012.

[119] Max Born and Robert Oppenheimer. Zur quantentheorie der molekeln. *Annalen der physik*, 389(20):457–484, 1927.

[120] John E Lennard-Jones. The electronic structure of some diatomic molecules. *Transactions of the Faraday Society*, 25:668–686, 1929.

[121] John C Slater. The theory of complex spectra. *Physical Review*, 34(10):1293, 1929.

[122] Douglas Rayne Hartree. The wave mechanics of an atom with a non-coulomb central field. part ii. some results and discussion. In *Mathematical Proceedings of the Cambridge Philosophical Society*, volume 24, pages 111–132. Cambridge University Press, 1928.

[123] Vladimir Fock. Näherungsmethode zur lösung des quantenmechanischen mehrkorperproblems. *Zeitschrift für Physik*, 61(1):126–148, 1930.

[124] Clemens Carel Johannes Roothaan. New developments in molecular orbital theory. *Reviews of modern physics*, 23(2):69, 1951.

[125] P Hohenberg and WJPR Kohn. Density functional theory (dft). *Phys. Rev*, 136:B864, 1964.

[126] Walter Kohn and Lu Jeu Sham. Self-consistent equations including exchange and correlation effects. *Physical review*, 140(4A):A1133, 1965.

[127] Sérgio Filipe Sousa, Pedro Alexandrino Fernandes, and Maria Joao Ramos. General performance of density functionals. *The Journal of Physical Chemistry A*, 111(42): 10439–10452, 2007.

[128] John P Perdew. Accurate density functional for the energy: Real-space cutoff of the gradient expansion for the exchange hole. *Physical Review Letters*, 55(16):1665, 1985.

[129] John P Perdew and Wang Yue. Accurate and simple density functional for the electronic exchange energy: Generalized gradient approximation. *Physical review B*, 33(12):8800, 1986.

[130] Swapan K Ghosh and Robert G Parr. Phase-space approach to the exchange-energy functional of density-functional theory. *Physical Review A*, 34(2):785, 1986.

[131] Axel D Becke. A new mixing of hartree–fock and local density-functional theories. *The Journal of chemical physics*, 98(2):1372–1377, 1993.

[132] A Wander and NM Harrison. An ab-initio study of zno (1120). *Surface science*, 468 (1-3):L851–L855, 2000.

[133] R Dovesi, VR Saunders, C Roetti, R Orlando, CM Zicovich-Wilson, F Pascale, B Civalleri, K Doll, NM Harrison, IJ Bush, et al. Crystal17. *University of Torino*, 2017.

[134] Roberto Dovesi, Alessandro Erba, Roberto Orlando, Claudio M Zicovich-Wilson, Bartolomeo Civalleri, Lorenzo Maschio, Michel Rérat, Silvia Casassa, Jacopo Baima, Simone Salustro, et al. Quantum-mechanical condensed matter simulations with crystal. *Wiley Interdisciplinary Reviews: Computational Molecular Science*, 8(4):e1360, 2018.

[135] Loredana Valenzano, Fernando J Torres, Klaus Doll, Fabien Pascale, Claudio M Zicovich-Wilson, and Roberto Dovesi. Ab initio study of the vibrational spectrum and related properties of crystalline compounds; the case of caco3 calcite. *Zeitschrift Für Physikalische Chemie*, 2006.

[136] Michael F Peintinger, Daniel Vilela Oliveira, and Thomas Bredow. Consistent gaussian basis sets of triple-zeta valence with polarization quality for solid-state calculations. *Journal of Computational Chemistry*, 34(6):451–459, 2013.

[137] Hendrik J Monkhorst and James D Pack. Special points for brillouin-zone integrations. *Physical review B*, 13(12):5188, 1976.

[138] G Gilat and LJ Raubenheimer. Accurate numerical method for calculating frequency-distribution functions in solids. *Physical Review*, 144(2):390, 1966.

[139] G Gilat. Analysis of methods for calculating spectral properties in solids. *Journal of Computational Physics*, 10(3):432–465, 1972.

[140] F Fischer and H Tropsch. The direct synthesis of petroleum hydrocarbons with standard pressure.(first report.). *Berichte Der Deutschen Chemischen Gesellschaft*, 59:830–831, 1926.

[141] Dietrich Stoltzenberg. *Fritz Haber: Chemist, Nobel Laureate, German, Jew*. Chemical Heritage Foundation, 2004.

[142] Mengting Yu, Lili Liu, Qiang Wang, Litao Jia, Bo Hou, Yubing Si, Debao Li, and Yi Zhao. High coverage h2 adsorption and dissociation on fcc co surfaces from dft and thermodynamics. *International Journal of Hydrogen Energy*, 43(11):5576 – 5590, 2018. ISSN 0360-3199. doi: https://doi.org/10.1016/j.ijhydene.2018.01.165. URL http://www.sciencedirect.com/science/article/pii/S0360319918303082.

[143] M.E. Belghiti, S. Echihi, A. Mahsoune, Y. Karzazi, A. Aboulmouhajir, A. Dafali, and I. Bahadur. Piperine derivatives as green corrosion inhibitors on iron surface; dft, monte carlo dynamics study and complexation modes. *Journal of Molecular Liquids*, 261:62 – 75, 2018. ISSN 0167-7322. doi: https://doi.org/10.1016/j.molliq.2018.03.127. URL http://www.sciencedirect.com/science/article/pii/S0167732217352145.

[144] Yijia Li, Zheshen Li, Ali Ahsen, Lutz Lammich, Gilbère J. A. Mannie, J. W. Hans Niemantsverdriet, and Jeppe V. Lauritsen. Atomically defined iron carbide surface

for fischer–tropsch synthesis catalysis. *ACS Catalysis*, 9(2):1264–1273, 2019. doi: 10.1021/acscatal.8b03684. URL https://doi.org/10.1021/acscatal.8b03684.

[145] Lorenzo Mino, Anna Maria Ferrari, Valentina Lacivita, Giuseppe Spoto, Silvia Bordiga, and Adriano Zecchina. Co adsorption on anatase nanocrystals: A combined experimental and periodic dft study. *The Journal of Physical Chemistry C*, 115(15):7694–7700, 2011. doi: 10.1021/jp2017049. URL https://doi.org/10.1021/jp2017049.

[146] Joachim Schnadt, Jan Knudsen, Xiao Liang Hu, Angelos Michaelides, Ronnie T. Vang, Karsten Reuter, Zheshen Li, Erik Lægsgaard, Matthias Scheffler, and Flemming Besenbacher. Experimental and theoretical study of oxygen adsorption structures on ag(111). *Phys. Rev. B*, 80:075424, Aug 2009. doi: 10.1103/PhysRevB.80.075424. URL https://link.aps.org/doi/10.1103/PhysRevB.80.075424.

[147] T Miyano, Y Sakisaka, T Komeda, and M Onchi. Electron energy-loss spectroscopy study of oxygen chemisorption and initial oxidation of fe (110). *Surface science*, 169(1): 197–215, 1986.

[148] C Leygraf and S Ekelund. A leed-aes study of the oxidation of fe (110) and fe (100). *Surface Science*, 40(3):609–635, 1973.

[149] E Vescovo, C Carbone, W Eberhardt, O Rader, T Kachel, and W Gudat. Spin-resolved photoemission study of the clean and oxygen-covered fe (110) surface. *Physical Review B*, 48(1):285, 1993.

[150] A Hodgson, A Wight, and G Worthy. The kinetics of o2 dissociative chemisorption on fe (110). *Surface science*, 319(1-2):119–130, 1994.

[151] Jonas Weissenrieder, Mats Göthelid, Martin Månsson, Henrik von Schenck, Oscar Tjernberg, and Ulf O Karlsson. Oxygen structures on fe (1 1 0). *Surface Science*, 527 (1-3):163–172, 2003.

[152] Tomasz Ossowski and Adam Kiejna. Oxygen adsorption on fe (110) surface revisited. *Surface Science*, 637:35–41, 2015.

[153] WB Pearson. *A Handbook of Lattice Spacings of Metals and Alloys*. Pergamon, New York, 1958.

[154] D Bagayoko and J Callaway. Lattice-parameter dependence of ferromagnetism in bcc and fcc iron. *Physical Review B*, 28(10):5419, 1983.

[155] A. Bil, B. Kolb, R. Atkinson, D. G. Pettifor, T. Thonhauser, and A. N. Kolmogorov. van der waals interactions in the ground state of $mg(bh_4)_2$ from density functional theory. *Phys. Rev. B*, 83:224103, Jun 2011. doi: 10.1103/PhysRevB.83.224103. URL https://link.aps.org/doi/10.1103/PhysRevB.83.224103.

[156] L Schimka, J Harl, A Stroppa, A Grüneis, M Marsman, F Mittendorfer, and G Kresse. Accurate surface and adsorption energies from many-body perturbation theory. *Nature materials*, 9(9):741, 2010.

[157] Yun Wang, Stefano de Gironcoli, Noel S. Hush, and Jeffrey R. Reimers. Successful a priori modeling of co adsorption on pt(111) using periodic hybrid density functional theory. *Journal of the American Chemical Society*, 129(34):10402–10407, 2007. doi: 10.1021/ja0712367. URL https://doi.org/10.1021/ja0712367. PMID: 17672452.

[158] Yu-Wei Huang and Shyi-Long Lee. Hybrid dft and hyper-gga dft studies of the co adsorption on pt nanoclusters: Effects of the cluster size and better co lumo description. *Chemical Physics Letters*, 492(1):98 – 102, 2010. ISSN 0009-2614. doi: https://doi.org/10.1016/j.cplett.2010.04.026. URL http://www.sciencedirect.com/science/article/pii/S000926141000549X.

[159] Joachim Paier, Martijn Marsman, and Georg Kresse. Why does the b3lyp hybrid functional fail for metals? *The Journal of chemical physics*, 127(2):024103, 2007.

[160] G-L Song. Corrosion electrochemistry of magnesium (mg) and its alloys. In *Corrosion of Magnesium alloys*, pages 3–65. Elsevier, 2011.

[161] JC Boettger. Nonconvergence of surface energies obtained from thin-film calculations. *Physical Review B*, 49(23):16798, 1994.

[162] George Blyholder. Infrared spectrum of co chemisorbed on iron. *The Journal of Chemical Physics*, 36(8):2036–2039, 1962.

[163] Vassiliki-Alexandra Glezakou, Liem X Dang, and B Peter McGrail. Spontaneous activation of co2 and possible corrosion pathways on the low-index iron surface fe (100). *The Journal of Physical Chemistry C*, 113(9):3691–3696, 2009.

[164] Weimin Zhao, Timing Zhang, Yonglin Wang, Jianhua Qiao, and Zerui Wang. Corrosion failure mechanism of associated gas transmission pipeline. *Materials*, 11(10):1935, 2018.

[165] Adriana Matamoros-Veloza, Richard Barker, Silvia Vargas, and Anne Neville. Mechanistic insights of dissolution and mechanical breakdown of feco3 corrosion films. *ACS Applied Materials & Interfaces*, 13(4):5741–5751, 2021.

[166] Kinga Freindl, Tomasz Ossowski, Marcin Zajac, Nika Spiridis, Dorota Wilgocka-Slezak, Ewa Madej, Tomasz Giela, Adam Kiejna, and Jozef Korecki. Oxygen adsorption on the fe (110) surface: The old system–new structures. *The Journal Of Physical Chemistry C*, 120(7):3807–3813, 2016.

[167] M Busch, M Gruyters, and H Winter. Feo (1 1 1) formation by exposure of fe (1 1 0) to atomic and molecular oxygen. *Surface science*, 600(13):2778–2784, 2006.

[168] P Błoński, A Kiejna, and J Hafner. Theoretical study of oxygen adsorption at the fe (1 1 0) and (1 0 0) surfaces. *Surface science*, 590(1):88–100, 2005.

[169] H-J Kim and E Vescovo. Spin-resolved photoemission investigation of the c (2× 2) and c (3× 1) oxygen overlayers on the fe (110) surface. *Physical Review B*, 58(20):14047, 1998.

[170] A Wight, NG Condon, FM Leibsle, G Worthy, and A Hodgson. Initial stages of fe (110) oxidation at 300 k: kinetics and structure. *Surface science*, 331:133–137, 1995.

[171] Si Chen, M-L Giorgi, J-B Guillot, and Grégory Geneste. Oxidation and diffusion processes at the mn-doped fe (0 0 1) and fe (1 1 0) surfaces from first-principles. *Applied surface science*, 258(22):8613–8618, 2012.

[172] C David Sherrill. Counterpoise correction and basis set superposition error. *School of Chemistry and Biochemistry, Georgia Institute of Technology*, 2010.

[173] Samuel F Boys and FJMP Bernardi. The calculation of small molecular interactions by the differences of separate total energies. some procedures with reduced errors. *Molecular Physics*, 19(4):553–566, 1970.

[174] Peter MA Sherwood. The use and misuse of curve fitting in the analysis of core x-ray photoelectron spectroscopic data. *Surface and Interface Analysis*, 51(6):589–610, 2019.

[175] Sunjic Doniach and M Sunjic. Many-electron singularity in x-ray photoemission and x-ray line spectra from metals. *Journal of Physics C: Solid State Physics*, 3(2):285, 1970.

[176] Helmut Öfner and Francisco Zaera. Surface defect characterization in oxygen-dosed nickel surfaces and in nio thin films by co adsorption- desorption experiments. *The Journal of Physical Chemistry B*, 101(44):9069–9076, 1997.

[177] M Rocca, L Savio, L Vattuone, U Burghaus, V Palomba, N Novelli, F Buatier de Mon-

geot, U Valbusa, R Gunnella, Giovanni Comelli, et al. Phase transition of dissociatively adsorbed oxygen on ag (001). *Physical Review B*, 61(1):213, 2000.

[178] Alessandro Baraldi, Silvano Lizzit, Giovanni Comelli, and Giorgio Paolucci. Oxygen adsorption and ordering on ru (101^{-} 0). *Physical Review B*, 63(11):115410, 2001.

[179] M Kinne, T Fuhrmann, JF Zhu, CM Whelan, R Denecke, and H-P Steinrück. Kinetics of the co oxidation reaction on pt (111) studied by in situ high-resolution x-ray photoelectron spectroscopy. *The Journal of chemical physics*, 120(15):7113–7122, 2004.

[180] CHEN Bohao, MA Yunsheng, DING Liangbing, XU Lingshun, WU Zongfang, YUAN Qing, and Weixin HUANG. Xps and tpd study of no interaction with cu (111): Role of different oxygen species. *Chinese Journal of Catalysis*, 34(5):964–972, 2013.

[181] Travis E Jones, Tulio CR Rocha, Axel Knop-Gericke, Catherine Stampfl, Robert Schlögl, and Simone Piccinin. Thermodynamic and spectroscopic properties of oxygen on silver under an oxygen atmosphere. *Physical Chemistry Chemical Physics*, 17(14):9288–9312, 2015.

[182] Helena Tillborg, Anders Nilsson, Tomas Wiell, Nial Wassdahl, Nils Mårtensson, and Joseph Nordgren. Electronic structure of atomic oxygen adsorbed on ni (100) and cu (100) studied by soft-x-ray emission and photoelectron spectroscopies. *Physical Review B*, 47(24):16464, 1993.

[183] Christian Heine, Baran Eren, Barbara AJ Lechner, and Miquel Salmeron. A study of the o/ag (111) system with scanning tunneling microscopy and x-ray photoelectron spectroscopy at ambient pressures. *Surface Science*, 652:51–57, 2016.

[184] VS Smentkowski and JT Yates Jr. The adsorption of oxygen on fe (110) in the temperature range of 90 to 920 k. *Surface Science*, 232(1-2):113–128, 1990.

[185] Linda GS Gray, Bruce G Anderson, Michael J Danysh, and Peter R Tremaine. Mechanisms of carbon steel corrosion in brines containing dissolved carbon dioxide at ph 4. *CORROSION/89, paper*, (464), 1989.

[186] Elisabeth Eriksrud and Terje Sontvedt. Effect of flow on co sub 2 corrosion rates in real and synthetic formation waters.(retroactive coverage). *Advances in CO sub 2 Corrosion.*, 1:20–38, 1984.

[187] Norman Neill Greenwood and Alan Earnshaw. *Chemistry of the Elements*. Elsevier, 2012.

[188] Wolfgang Wagner and Hans-Joachim Kretzschmar. Iapws industrial formulation 1997 for the thermodynamic properties of water and steam. *International steam tables: properties of water and steam based on the industrial formulation IAPWS-IF97*, pages 7–150, 2008.

[189] Lawrence Korson, Walter Drost-Hansen, and Frank J Millero. Viscosity of water at various temperatures. *The Journal of Physical Chemistry*, 73(1):34–39, 1969.

[190] Zhenhao Duan, Rui Sun, Chen Zhu, and I-Ming Chou. An improved model for the calculation of co2 solubility in aqueous solutions containing na+, k+, ca2+, mg2+, cl-, and so42-. *Marine Chemistry*, 98(2-4):131–139, 2006.

[191] Julio E Garcia. Density of aqueous solutions of co2. Technical report, Lawrence Berkeley National Lab.(LBNL), Berkeley, CA (United States), 2001.

[192] William L Marshall and EU Franck. Ion product of water substance, 0–1000 c, 1–10,000 bars new international formulation and its background. *Journal of physical and chemical reference data*, 10(2):295–304, 1981.

[193] Dedong Li and Zhenhao Duan. The speciation equilibrium coupling with phase equilibrium in the h2o–co2–nacl system from 0 to 250 c, from 0 to 1000 bar, and from 0 to 5 molality of nacl. *Chemical Geology*, 244(3-4):730–751, 2007.

[194] Kenneth S Pitzer. Thermodynamics of electrolytes. v. effects of higher-order electrostatic terms. *Journal of Solution Chemistry*, 4(3):249–265, 1975.

[195] Nancy Møller. The prediction of mineral solubilities in natural waters: A chemical equilibrium model for the na-ca-cl-so4-h2o system, to high temperature and concentration. *Geochimica et Cosmochimica Acta*, 52(4):821–837, 1988.

[196] HF Holmes, RH Busey, John M Simonson, Robert E Mesmer, DG Archer, and RH Wood. The enthalpy of dilution of hcl (aq) to 648 k and 40 mpa thermodynamic properties. *The Journal of Chemical Thermodynamics*, 19(8):863–890, 1987.

[197] Roberto T Pabalan and Kenneth S Pitzer. Thermodynamics of naoh (aq) in hydrothermal solutions. *Geochimica et Cosmochimica Acta*, 51(4):829–837, 1987.

[198] DA Polya, EM Woolley, JM Simonson, and RE Mesmer. The enthalpy of dilution and thermodynamics of na2co3 (aq) and nahco3 (aq) fromt= 298 k tot= 523.15 k and pressure of 40 mpa. *The Journal of Chemical Thermodynamics*, 33(2):205–243, 2001.

[199] Christomir Christov and Nancy Moller. Chemical equilibrium model of solution behavior and solubility in the h-na-k-oh-cl-hso4-so4-h2o system to high concentration and temperature. *Geochimica et Cosmochimica Acta*, 68(6):1309–1331, 2004.

[200] Charles E Harvie, Nancy Møller, and John H Weare. The prediction of mineral solubilities in natural waters: The na-k-mg-ca-h-cl-so4-oh-hco3-co3-co2-h2o system to high ionic strengths at 25 c. *Geochimica et Cosmochimica Acta*, 48(4):723–751, 1984.

[201] Frank J Millero and Denis Pierrot. A chemical equilibrium model for natural waters. *Aquatic Geochemistry*, 4(1):153–199, 1998.

[202] Giles M Marion, David C Catling, and Jeffrey S Kargel. Modeling aqueous ferrous iron chemistry at low temperatures with application to mars. *Geochimica et cosmochimica Acta*, 67(22):4251–4266, 2003.

[203] Bockris JO'M, D Drazic, and AR Despic. The electrode kinetics of the deposition and dissolution of iron. *Electrochimica Acta*, 4(2-4):325–361, 1961.